Sensitivity analysis of
low-density jets and flames

by

Gary James Chandler
Emmanuel College

A dissertation submitted for the degree of Doctor of Philosophy

May 2010

Department of Engineering
University of Cambridge

Declaration

This dissertation is the result of my own work and includes nothing which is the outcome of work done in collaboration except where specifically indicated in the text and Acknowledgements. No part of this dissertation has already been, or is concurrently being, submitted for any degree, diploma or qualification.

This dissertation contains no more than 65000 words or 150 figures.

....

Gary James Chandler

5th May 2010

Sensitivity analysis of low-density jets and flames

Gary J. Chandler

Abstract

This work represents the initial steps in a wider project that aims to map out the sensitive areas in fuel injectors and combustion chambers. Direct numerical simulation (DNS) using a Low-Mach-number formulation of the Navier–Stokes equations is used to calculate direct-linear and adjoint global modes for axisymmetric low-density jets and lifted jet diffusion flames. The adjoint global modes provide a map of the most sensitive locations to open-loop external forcing and heating. For the jet flows considered here, the most sensitive region is at the inlet of the domain.

The sensitivity of the global-mode eigenvalues to force feedback and to heat and drag from a hot-wire is found using a general structural sensitivity framework. Force feedback can occur from a sensor-actuator in the flow or as a mechanism that drives global instability. For the lifted flames, the most sensitive areas lie between the inlet and flame base. In this region the jet is absolutely unstable, but the close proximity of the flame suppresses the global instability seen in the non-reacting case. The lifted flame is therefore particularly sensitive to outside disturbances in the non-reacting zone.

The DNS results are compared to a local analysis. The most absolutely unstable region for all the flows considered is at the inlet, with the wavemaker slightly downstream of the inlet. For lifted flames, the region of largest sensitivity to force feedback is near to the location of the wavemaker, but for the non-reacting jet this region is downstream of the wavemaker and outside of the pocket of absolute instability near the inlet.

Analysing the sensitivity of reacting and non-reacting variable-density shear flows using the low-Mach-number approximation has up until now not been done. By including reaction, a large forward step has been taken in applying these techniques to real fuel injectors.

Key words: hydrodynamic instability, low-density jet, low-Mach-number Navier–Stokes, diffusion flame, structural sensitivity, force feedback, hot wire, adjoint operator, non-normality, global modes, absolute instability.

Dedicated to my father, who was the early source of my interest in science and engineering and taught me the value of hard work and determination.

Contents

List of Figures

List of Tables

Preface

The work described in this thesis was undertaken between March 2008 and May 2010 at the Department of Engineering, University of Cambridge, with occasional brief visits to LadHyX, École Polytechnique. Preliminary work in this field was undertaken between October 2006 and March 2008 and was presented at the 2007 APS/DFD annual meeting in Salt Lake City, Utah.

The numerical computations were initially carried out on the LadHyX cluster, with subsequent work performed using the Darwin Supercomputer of the University of Cambridge High Performance Computing Service (http://www.hpc.cam.ac.uk/).

The work represents the first steps of a much wider project and as such has been written with continuation and future work in mind. In particular chapter 6 gives some quite detailed descriptions of what could be done next and contains preliminary work I've started, but not had a chance to follow up. Included throughout the text are many suggestions and references, particularly in the boundary conditions section, that I hope will give anyone who wishes to continue this work a bit of a head start.

I've tried to make the sections and chapters as self-contained as possible, so that it is hopefully possible to go straight to the section of interest without the prerequisite of reading all the previous chapters. In particular I hope the sections in chapter 4 on sensitivity analysis can be read by anyone with an idea of linear systems. The derivations assume no knowledge of the exact form of the governing equations, boundary conditions or solution procedure. All that is needed are the direct and adjoint global modes of any time-evolving linear system. The structural sensitivity section is a short opening section giving a general framework with the following two sections going into specific examples for hydrodynamic instability.

Finally it's worth mentioning the 'Instaflow' application that was used to produce the results of the local analysis in chapter 5. This is a Matlab graphical user interface

developed by my supervisor Dr. Juniper and a number of of his students. While I have not used it thoroughly myself, it seems to make light work of slicing up and analysing my vast amounts of numerical data.

Acknowledgements

I would firstly like to thank my supervisor, Dr. Matthew Juniper, for guiding me through this work, for the great people he has put me in contact with, for providing the results for section 4.5 of this thesis and for all the small odds and ends - some I know about and some I probably wasn't aware of - which he could have asked me to do, but instead just did them himself. Although, it has occurred to me that there are two possibilities when supervisors do tasks (especially important tasks) for you - either they are being nice or are they think you are incompetent. Hopefully this thesis will show the former to be true. I would finally like to thank Matt for being a great person to work with and (on the odd occasion) socialize with over the last three and a half years.

A special thank you is extended to Dr. Joseph Nichols and Prof. Peter Schmid for providing me with the nonlinear versions of the Low-Mach-number code, from which the linear and adjoint codes were developed, and for the vast amounts of knowledge and advice they have passed on. I would further like to thank Prof. Schmid for initially inviting me to the workshop in Tuscany, where he never tired of my endless questions about adjoints, for making me feel welcome at LadHyX and for letting me have time on the LadHyX cluster.

I would also like to thank Dr. Colm Caulfield, for providing the necessary introduction to this field and for giving some key insights along the way, and Dr. Flavio Giannetti for some enlightening tips on the discrete-adjoint approach.

I would like to thank the guys in the lab (past and present) - Kane, Tash, Kamal, Regitz, Payney, Chris, Johannes, Hao, Patrick, Larry, Iain and Ubaid - who sparked off a variety of interesting conversations and projects and made the lab a friendly and enjoyable working environment. A further thank you is extended to Iain, Ubaid and

Sam for reading and commenting on this work prior to submission. Sam especially has asked (and helped answer) some very helpful questions along the way.

Finally I would like to thank Alexie for putting up with (especially in the last few months) my somewhat dubious multi-tasking skills and apparent ability, while I focused on my work, to blank out everything that goes on around me.

Emmanuel College   Gary Chandler
Cambridge
May 2010

Chapter 1

Introduction

Fuel injectors

Fuel injectors exploit natural hydrodynamic instabilities to mix reactants well in combustion chambers. Good mixing is essential to ensure complete combustion over a short distance. In gas turbines, for instance, this minimizes overall length and weight, which is important for increasing the fuel efficiency of the aircraft. Fuel injectors have elaborate shapes and complex flow dynamics, often involving large amounts of swirl and turbulence. To a first approximation, however, fuel injectors can be considered to be one of two types of shear flow: a jet flow, where the injected fuel velocity is greater than the surrounding oxidizer velocity, or a wake flow, where the injected fuel velocity is less than the surrounding oxidizer velocity. Jet type fuel injectors are commonly used in automotive engines, whereas wake type injectors are commonly used in gas turbines. The physical properties and analysis of each type of flow are closely related.

Turbulent shear flows are far better at mixing than laminar shear flows. According to Schmid & Henningson (2001), transition to turbulence usually starts with the projection of random initial disturbances into exponentially-growing eigenmodes and/or transiently-growing optimal perturbation structures. The linear growth of these primary instabilities usually leads to nonlinear saturation and the new quasi-steady flow becomes the base flow for shorter-wavelength secondary instabilities. Nonlinearities and/or higher instabilities proceed to excite an increasing number of scales and frequencies in the flow, eventually leading to the breakdown to turbulence. Linear growth mechanisms are therefore an influential part in the transition process and are looked at specifically by Henningson & Reddy (1994).

In aircraft engines, the fuel and air are both turbulent before they enter the combustion chamber. Broadwell & Breidenthal (1982) show that large scale structures in the turbulent shear flows are responsible for mixing. In particular they describe a mixing model where the interfacial area between the two fluids grows as it is distorted by the motion of the large scale structures and by secondary structures and small eddies, which exist within the large scale structures. This starts slowly and becomes more and more rapid as successively finer scales develop, until the Kolmogorov scales are reached, where rapid molecular diffusion occurs. This initial model assumes that the diffusion-layer thickness is small compared to the turbulent-layer thickness, which is appropriate for high Schmidt and Reynolds numbers. Broadwell (1988) extended this model to interfaces with diffusion layers, where the thickness is dependent on the molecular transport coefficients. In both cases, the fluid entrainment rate, caused by the motion of the large scale structures, is influential to the mixing rate, a finding that is supported by Catrakis *et al.* (2005). These large-scale coherent structures have been observed in turbulent jet flow at high Reynolds numbers by Broadwell & Mungal (1991) and Catrakis *et al.* (2002). The large scale structures occur due to global instabilities of the turbulent shear flow. Global instability therefore plays an important role in both the transition to turbulence and turbulent mixing itself.

Within the mixing zone there is a region where the fuel to oxidizer ratio is sufficiently close to the stoichiometric ratio for combustion to occur. The local flow conditions, however, affect combustion by convecting heat away from the combustion zone. If the rate of convection is too large, the flame cannot stabilize at that point. An example of this occurs in lifted jet diffusion flames, where the liftoff height is sensitive to the jet velocity (Brown *et al.*, 1999). Combustion has a significant effect on flow dynamics and mixing within the combustion chamber. The combustion process for most common fuels is complex and involves many different intermediate reactions to convert fuel and oxidizer into the final combustion product. The reacting gas is a non-isothermal mixture of multiple species, each having a different set of transport coefficients. Each species must be tracked individually and the rates at which these species react require careful modelling (Poinsot & Veynante, 2005). This is complicated further with incomplete combustion and secondary reactions due to the high temperatures, such as the generation of nitrogen oxides from the nitrogen and oxygen contained in air.

Initial work into combustion chambers for rockets and aircraft involved much experimentation and guesswork (Heppenheimer, 1997). Today our ability to measure and

simulate the internal processes of combustion chambers has improved our knowledge of what is happening, but it has not always improved our understanding of why it is happening. To answer the question 'why' rather than 'what' requires a greater toolbox than accurate modelling alone. Although applied mathematicians have developed many useful tools, it is only relatively recently that some of these tools have been applied to real fuel injectors. A recent example is the 'Instaflow' application (Correia Da Costa, 2009), which uses local analysis techniques (Huerre & Monkewitz, 1990) to provide extra information about the nature and origin of existing global modes inside real combustion chambers. Nonlinear adjoint looping has also recently been used to find optimal perturbations in a canonical combustion-instability problem, to improve understanding of triggering of sustained oscillations in a linearly stable system (Juniper, 2011).

The behaviour of a combustion system is extremely sensitive to the injector geometry, the heat release due to combustion and acoustics in the combustion chamber (see Culick *et al.*, 1995, and Ananthkrishnan *et al.*, 2005, for a review of combustion instability). The design of an injector also influences the overall cost of manufacture and running of the engine and involves many simulations and experiments to improve existing designs incrementally. An understanding of the sensitive areas of an injector can not only allow a more guided design approach, but can also provide useful information for the design team. For example, if the desired flow dynamics have been established by computational fluid dynamics, sensitivity information could significantly aid the realization of that design by providing the materials scientists and structural engineers with information about the most influential parts of the desired injector geometry, i.e. the regions of the injector that must not be altered between the prototype and the manufacturing stage.

The overall aim of the wider project is to develop the capability of producing sensitivity maps of real fuel injectors in combustion chambers. The maps would give information about where various design changes have the largest and smallest effects on the rate of mixing and the sensitivity to acoustics. This thesis represents part of the initial work into adapting existing sensitivity analysis techniques within the fluid dynamics community to eventually be applied to real fuel injectors.

The starting point is the work by Giannetti & Luchini (2007), who produced sensitivity maps for the primary instability of a cylinder wake. Cylinder wakes and fuel injectors are both natural oscillators (as opposed to amplifiers, see Huerre & Monkewitz, 1990; Chomaz, 2005) and have therefore a natural frequency of oscillation and global

mode shape that dominate the flow dynamics. The natural oscillation is believed to arise from a hydrodynamic feedback loop that is inherent in the underlying system of equations (Chomaz *et al.*, 1991; Monkewitz *et al.*, 1993; Giannetti & Luchini, 2007).

The spatial sensitivity maps calculated by Giannetti & Luchini (2007) give the sensitivity of the frequency and amplitude of the natural oscillation to perturbations of an assumed force-momentum feedback coupling. Giannetti & Luchini (2007) define the region of maximum sensitivity as the 'instability core'. The 'instability core' of the primary instability of a fuel injector is of key interest because it is the region that has the largest influence on the global flow dynamics and combustion process. It has therefore the largest influence on the overall efficiency of the fuel injector and combustion chamber design.

It is worth pointing out that the use of sensitivity maps is not a new concept in engineering design optimization. The principles on which they are established were first used for steady fluid dynamic design by Pironneau (1974) and later for aerodynamic design optimization of a wing by Jameson (1988), which gave rise to a large expansion of aeronautical optimization research (see Jameson, 1999; Newman *et al.*, 1999). While similarities exist between the sensitivity maps for current aeronautical design optimization and for cylinder wakes, the fundamental difference is the stability properties of the flows concerned. For aeronautical applications the flows considered are steady and lend themselves in a more straightforward way to design optimization using sensitivity information. For cylinder wakes and fuel injectors the flows are unsteady and require therefore a more complex approach for design optimization using sensitivity information.

Flow instability methods

Early work in flow instability produced the well-known Rayleigh's inflection point criterion for inviscid parallel flows (Rayleigh, 1880). In more modern times the use of linear eigenmodes to study the instability of parallel shear flows (see Drazin & Reid, 1981) has become increasingly popular. The concepts of absolute and convective instabilities, originally introduced in plasma physics (Briggs, 1964), distinguish between parallel flows that oscillate of their own accord and parallel flows that act as amplifiers of external disturbances. Under the parallel flow assumption, Ashpis & Reshotko (1990) applied the absolute/convective approach to the vibrating ribbon problem, in

which a boundary layer amplifies the disturbance produced by the ribbon. Huerre & Monkewitz (1985) carried out a similar analysis for a parallel spatial mixing layer and dicuss the implications for hot jets and wakes.

Juniper (2006) used a linear spatio-temporal analysis to provide a thorough theoretical account of the effect of confinement on the transition from convective to absolute instability for parallel planar jets and wakes. This work is particularly relevant in the study of fuel injectors given the observation by Barrère *et al.* (1960) that confining the outer flow of fuel injectors is beneficial for mixing. This observation is supported by results from numerical (Delbende & Chomaz, 1998; Garcia-Villalba *et al.*, 2006) and theoretical (Juniper & Candel, 2003) studies, which suggest that confinement can enhance the instability of the flow.

The extension of the absolute/convective approach to weakly non-parallel flows can be made using a WKBJ approximation (Bender & Orszag, 1978) and introduces the concepts of global modes and the wavemaker (Huerre & Monkewitz, 1990; Huerre & Rossi, 1998; Huerre, 2000). This approach is known as a local analysis, because at each streamwise location the flow is considered independently. At each streamwise location the flow is assumed to be parallel and to extend infinitely far up- and downstream. It is then assessed to be either absolutely unstable, where disturbances spread up- and downstream, or convectively unstable, where disturbances are swept away from the source. For weakly non-parallel flows to act as oscillators, they require a region of absolute instability that is large enough and strong enough to act as a wavemaker. The wavemaker provides a natural oscillation that can be amplified finite distances up- and downstream by surrounding convectively-unstable regions in the flow, which gives rise to a global mode. A particularly relevant application of linear absolute/convective instability methods to analyze fully nonlinear global modes in hot and helium jets has been made by Kyle & Sreenivasan (1993).

Weakly nonlinear theory, involving Landau amplitude equations, provides a more accurate extension of the linear theory to the fully nonlinear regime in the vicinity of the first bifurcation point (Huerre & Rossi, 1998; Chomaz, 2005). Fully-nonlinear extensions and the front concept are reviewed by Huerre (2000) and Chomaz (2005), with the latter reviewing in depth the role non-normality plays in non-parallel flows and how non-normality limits the use of linear theory to describe nonlinear dynamics. Pier (2002) successfully applied a local analysis to a highly non-parallel cylinder wake using both linear and nonlinear theory.

The non-parallel approaches typically make use of a steady, but unstable, solution of the fully-nonlinear governing equations. Traditionally this has been done with root finding algorithms, such as the Newton methods, applied to the steady nonlinear problem (Fletcher, 1991). Methods that damp down the high-frequency unstable components in the unsteady problem (Åkervik *et al.*, 2006) have recently been gaining in popularity due to the relative ease with which they can be applied to existing time-stepping codes.

Linear eigenmodes have been calculated and used in numerical stability studies of highly-non-parallel flows. For example Zebib (1987) and Hill (1992), with spectral techniques, and Jackson (1987), with finite elements, used linear eigenvalue theory to predict the critical Reynolds number for the onset of oscillations in the flow behind a cylinder. To analyze the secondary instability behind a cylinder, Barkley & Henderson (1996), using a spectral-element method, conducted a linear Floquet stability analysis with the time-evolving nonlinear global mode as the base flow. The Floquet stability analysis is an extension of the eigenfunction analysis for periodic time-evolving base flows.

Numerical analysis has also opened the door to different modal decomposition techniques. In flow control and model reduction, Proper Orthogonal Decomposition (POD) is often used (Berkooz *et al.*, 1993). The use of Krylov methods for linear eigenmode decomposition in unstable flows (Edwards *et al.*, 1994) has led to a new decomposition technique for fully nonlinear problems. Applying Krylov techniques to a nonlinear time evolution, Rowley *et al.* (2009) and Schmid (2010) calculate dynamic modes that characterize nonlinear behaviour in a similar way to the way in which eigenmodes characterize linear behaviour. Schmid *et al.* (2010) carried out a reconstruction and dynamic mode decomposition of experimental data of a helium jet.

Non-normality

While modal analysis techniques give good insight into the long time hydrodynamic instability behaviour, they usually do not give a quantitative description of short-term disturbance behaviour. Transient effects arise from modal interactions due to the non-normality of the governing operator. An operator is referred to as normal if its set of eigenfunctions are orthogonal and is referred to as non-normal if the set of eigenfunctions are not orthogonal. For open flows, the main source of non-normality in the linear evolution operator is the difference in sign of the regular and adjoint basic flow advection

term compared to the diffusive term, which causes spatial separation of the direct and adjoint modes (Chomaz, 2005).

The analysis of transient effects falls into the category of non-modal stability theory (Schmid & Henningson, 2001; Schmid, 2007). For highly non-normal flows the spectrum of eigenvalues is often a poor indicator of disturbance behaviour in the short term and a disturbance that grows most over a short time scale often differs significantly from the least stable eigenmode. Trefethen *et al.* (1993) introduced the concept of pseudospectra to quantify non-normal amplification and point out that transient growth can occur even when a corresponding modal analysis would predict that all eigenmodes are stable. Cossu & Chomaz (1997) demonstrated that stream-wise non-normality can lead to large transient growth of the initial perturbation energy.

As well as transient effects, non-normality can lead to extreme sensitivity to forcing (Chomaz, 2005) and extreme sensitivity of eigenvalues to operator perturbations (Reddy *et al.*, 1993). Non-normality can also lead to to a wide gap between the critical Reynolds numbers calculated by linear eigenfunction theory and energy stability theory (Reddy *et al.*, 1993) and to pseudoresonance (Trefethen *et al.*, 1993), where a large resonance occurs in an amplifier type flow even though the forcing frequency is not near any eigenvalue frequency.

Adjoint operators

The concept of non-normality is closely linked to that of adjoint operators. If an operator is normal it commutes with its corresponding adjoint operator; if an operator is non-normal it does not commute with its adjoint operator. In terms of eigenfunctions for a linear operator, the set of direct linear eigenfunctions and the corresponding set of adjoint eigenfunctions are biorthogonal (Salwen & Grosch, 1981; Hill, 1995). This means that for each direct eigenfunction there is only one non-orthogonal adjoint eigenfunction, which has an adjoint eigenvalue that is the complex conjugate of the corresponding direct eigenvalue.

The adjoint operator essentially provides gradient information about the direct operator and has been used directly in receptivity analyses (Hill, 1995); in optimal flow control (Bewley, 2001; Guegan *et al.*, 2006); and in optimization routines to find 'optimal perturbations' for maximum transient growth using linear theory (Andersson *et al.*, 1999; Luchini, 2000; Corbett & Bottaro, 2001; Guegan *et al.*, 2006).

A number of extensions to the linear optimal perturbation framework have been successfully implemented, for example, optimal perturbations for flows with moving domains (Protas & Liao, 2008) and optimal perturbations for fully nonlinear systems (Zuccher *et al.*, 2006; Juniper, 2011), where the adjoint of the nonlinear operator is actually linear and is calculated using a time-evolving operator derived from the time-evolving direct calculation.

It is worth pointing out that, although adjoint operators are versatile, they are not the only means to carry out analyses like those above. Butler & Farrell (1992) used a superposition of the leading eigenmodes to create a variational problem, which was solved for optimal perturbations. Another alternative for the optimal perturbation problem is to carry out a singular value decomposition of the non-self-adjoint perturbation matrix (Schmid & Henningson, 2001). Schmid & Henningson also use a similar approach in the related problem of optimal forcing. The use of adjoint techniques forms an efficient optimization routine for systems with many degrees of freedom. For systems with few degrees of freedom, however, estimating the local gradient function with a numerical scheme is relatively simple.

The form of the adjoint depends on the inner product used to determine it, with a natural choice being one related to the disturbance energy (Schmid & Henningson, 2001). Other choices of inner product to define the adjoint exist and are discussed in depth by Protas *et al.* (2004).

Sensitivity analyses

The experiments of Strykowski & Sreenivasan (1990) determined the most sensitive regions of the primary instability of a cylinder wake to the placement of smaller cylinders. They found that when the smaller cylinders were placed in certain regions, the natural oscillation of the wake could be suppressed. This prompted the numerical sensitivity analyses of Hill (1992) and Giannetti & Luchini (2007). Similar experimental studies, perhaps more relevant to the present work, are those of Sreenivasan *et al.* (1989) and Toong *et al.* (1965). Sreenivasan *et al.* observed the suppression of natural oscillations in helium-air jets by the placement of a control wire in the near field of the jet, while Toong *et al.* studied the flame behind a burning cylinder and found that the placement of small non-burning cylinders slightly downstream of the main burning cylinder suppressed the natural oscillation of the flame.

Hill (1992) modelled the drag force exerted by a small cylinder on the flow near the first bifurcation point of a cylinder wake and used linear theory and adjoint eigenfunctions to predict the most sensitive regions, which coincided well with the experimental findings of Strykowski & Sreenivasan (1990). Giannetti & Luchini (2007) extended the work of Hill (1992) by lengthening the computational domain and provided a more general framework in terms of the force-momentum feedback coupling and instability core. Using a linear Floquet analysis, Luchini *et al.* (2008) performed a sensitivity analysis similar to that of Giannetti & Luchini (2007) for the cylinder wake away from the bifurcation point and well into the fully nonlinear regime. Using a similar Floquet technique Giannetti *et al.* (2010) calculate the location of the core of the secondary instability of a cylinder wake that develops on the saturated nonlinear global mode.

With the exception of Hill (1992), the sensitivity analyses described above have focused on structural perturbations of the linear operator resulting from a change in the perturbative forcing in the linear equations. This perturbative forcing only affects the linear global modes and not the underlying base flow. Hill (1992) recognised that the steady component of the drag force would affect the instability through altering the base flow, but treated it as negligible compared to the direct effect of the perturbative force on the linear operator. Bottaro *et al.* (2003) found, however, that relatively small changes in the base flow of plane Couette flow have a destabilizing effect on the eigenvalues. The concept of the sensitivity to a steady force was developed in a more general linear Lagrange-multiplier framework by Marquet (2008) for the incompressible flow behind a cylinder near the bifurcation point and this approach has been extended by Meliga (2008) for near-bifurcation compressible after-body flows, which allow for the introduction of the sensitivity to steady heating and the sensitivity to localized wall blowing and cooling. Meliga & Chomaz (2010) applied the same technique to investigate the global modes of a jet impinging on a flat plate.

Giannetti *et al.* (2010) state that the sensitivity to the perturbative source terms alone is the appropriate tool to study the position of the wavemaker and investigate the physical nature of the instability, whereas the investigation into the sensitivity to steady source terms is more appropriate to develop effective control strategies to suppress the instability or for direct comparison to experiments. This statement is plausible and suggests that steady source terms influence eigenvalue growth rates and frequencies to a greater extent than perturbative source terms. If this is the case then the sensitivity to steady source terms would also be more appropriate for design optimization, while

perturbative source terms would provide a greater insight into the actual instability mechanisms present in the flow.

Overview

As the initial part of a wider project, this work first calculates in chapter 2 the direct and adjoint global modes for the primary instability of a low-density jet mixing with an ambient fluid. This is representative of a light gaseous fuel being injected into a combustion chamber containing air. To analyze the effect of heat release due to combustion and the resulting fluid expansion on the sensitivity of the primary instability, the model is extended in chapter 3 to that of a lifted jet diffusion flame by including a simple combustion model. In chapter 4, a physical meaning of the adjoint global modes is derived and the direct and adjoint modes are used to carry out a similar sensitivity study to that of Giannetti & Luchini (2007) for the low density jet and lifted jet diffusion flame. The sensitivity of the eigenvalues to the placement of a hot wire in the flow is then considered. The last section of chapter 4 compares the results to a local analysis. Chapter 5 outlines the next steps to move further towards the goal of sensitivity maps of real fuel injectors. Finally, in chapter 6, some overall concluding remarks are drawn for this work.

Chapter 2

Hot jets

2.1   Introduction

An axisymmetric non-swirling low-density jet has been chosen as the first problem to
investigate, because it contains some of the key elements that drive instabilities in real
fuel injectors, while still being of fundamental interest to the fluid dynamics community.
The local analysis of Lesshafft & Huerre (2007) highlights the importance of the density
ratio of the jet to the surroundings in determining whether the flow behaves as an
oscillator or an amplifier. When the ratio is unity the jet behaves as an amplifier. As
the density ratio decreases, i.e. the jet becomes lighter than the surroundings, the flow
becomes more unstable until a natural oscillation occurs.

The particular type of low-density jet studied in this chapter is that of a hot jet,
which is dynamically similar to a jet containing a low-density species surrounded by a
high-density species, herein referred to as a light jet. A number of experimental studies
have observed oscillatory behaviour for both hot and light jets. Sreenivasan *et al.* (1989)
looked at the nature of absolute instability of helium-air jets exiting into ambient air;
Monkewitz *et al.* (1989) studied the entrainment of fluid into self-excited hot jets at
transitional Reynolds numbers; Monkewitz *et al.* (1990) studied self-excited oscillations
and mixing in a heated round jet; Yildirim & Agrawal (2005) studied self-excited os-
cillations in momentum-dominated helium jets and Schmid *et al.* (2010) carried out a
dynamic-mode decomposition of experimental data from an unforced and harmonically
forced helium jet.

Early theoretical studies on variable density shear flows were performed by Taylor
(1931), Goldstein (1931) and Drazin (1958). For the specific case of low-density jets,

Monkewitz & Sohn (1988) performed a local analysis of hot jets exiting into ambient conditions, which was extended by Jendoubi & Strykowski (1994) to jets with coflow and counterflow. The spatio-temporal analysis of the full impulse response was then completed by Lesshafft & Huerre (2007). Lesshafft *et al.* (2006) carried out a theoretical study of nonlinear global modes in hot jets and Nichols *et al.* (2007) carried out a direct numerical simulation (DNS) and local analysis to look at the effect buoyancy plays on the nature of self-sustained oscillations in variable-density jets.

In this study the direct and adjoint global modes are found with DNS using a low-Mach-number formulation of the Navier–Stokes equations as used by Nichols *et al.* (2007).

2.2 Governing equations

The Low-Mach-number approximation

The low-Mach-number approximation (McMurtry *et al.*, 1986; McMurtry, 1987) produces a set of equations that allow for density variation due to temperature or species variation, but not due to compressibility. The low-Mach-number equations allow therefore the study of low density jets and flames without the need to resolve acoustic time and length scales. They are based on the fully compressible Navier–Stokes equations and lie in between the fully compressible and incompressible Navier–Stokes equations, bearing resemblances to both. The Low-Mach-number equations are different to those formed with the Boussinesq approximation. Using the Boussinesq approximation, density variations are neglected everywhere except in the buoyancy related terms, whereas using the low-Mach-number approximation density variations are included everywhere. The Boussinesq approximation is commonly used in geophysical flows where the density varies with height due to atmospheric effects. This variation is not considered in the low-Mach-number equations, where density variation is only caused by different species or temperature variation.

The nonlinear low-Mach-number equations have been used successfully to simulate self-sustained oscillations in variable-density round jets (Nichols, 2005; Nichols *et al.*, 2007); unsteady combustion in pre-mixed flames (Najm *et al.*, 1998); turbulent reactive plumes (Cook & Riley, 1996); and self-sustained oscillations in variable-density lifted diffusion flames (Nichols, 2005; Nichols & Schmid, 2008; Nichols *et al.*, 2009).

While a set of adjoint equations has been formed for many different equation sets in fluid dynamics, this does not seem to have been done for the low-Mach-number equations. The adjoint equations corresponding to the incompressible Navier–Stokes equations are well known (see Giannetti & Luchini, 2007, for an example), while the adjoint equations corresponding to the fully-compressible Navier–Stokes equations have been derived by Cerviño *et al.* (2002) and Meliga (2008).

Equation derivations

Starting from a set of non-dimensionalized fully-compressible Navier–Stokes equations, each variable is expressed in a form similar to $p = p^{(0)} + \gamma Ma^2 p^{(1)} + \cdots$, where p is the non-dimensional pressure, and the Mach number, Ma, and γ are defined in table 2.1. In the limit of low Mach number, all terms of order Ma^2 disappear except for the pressure term in the momentum equation, which contains the factor $1/\gamma Ma^2$. This term implies that the low-Mach-number momentum equation is balanced by $\boldsymbol{\nabla} p^{(1)}$ and that $\boldsymbol{\nabla} p^{(0)} = \boldsymbol{0}$.

The domain is cylindrical and uses a collocated grid with cylindrical polar coordinates (r, θ, x). The inlet (jet exit plane) is located at the axial location $x = 0$ and the outlet at $x = X_{max}$, with uninormly spaced grid points in the axial direction. The lateral boundaries are located at a radial distance $r = R_{max}$ from the centreline, with skewed grid spacing in the radial direction. For the results in this thesis, only axisymmetric flows are considered, but the analysis can be extended to fully 3D regimes. The full derivation of the nonlinear equations along with a full description of the computational domain and non-dimensionalizations are given in Nichols *et al.* (2007). The definitions of all non-dimensionalized variables and parameters are given in table 2.1. The superscript (0) has been dropped on all non-dimensional variables except for p. Dimensional variables are denoted by $(\sim)$, ambient conditions are denoted by subscript (0) and conditions for the jet at entry are denoted by subscript (j). The non-dimensional

nonlinear low-Mach-number equations are

$$\frac{\mathrm{D}\rho}{\mathrm{D}t} + \rho(\boldsymbol{\nabla} \cdot \boldsymbol{u}) = 0, \tag{2.1a}$$

$$\frac{\partial\,(\rho\boldsymbol{u})}{\partial t} + \boldsymbol{\nabla}p^{(1)} - \boldsymbol{\nabla} \cdot \left(\frac{1}{S_1 Re}\boldsymbol{\tau} - \rho\boldsymbol{u}\boldsymbol{u} \right) + Ri\,(1 - \rho)\,\hat{\boldsymbol{g}} = \boldsymbol{0}, \tag{2.1b}$$

$$\rho\frac{\mathrm{D}T}{\mathrm{D}t} - \frac{1}{S_1 Re Pr}\nabla^2 T = 0, \tag{2.1c}$$

$$\rho\,((S_1 - 1)\,T + 1) = p^{(0)}, \tag{2.1d}$$

$$\boldsymbol{\nabla}p^{(0)} = \boldsymbol{0}, \tag{2.1e}$$

$$\boldsymbol{\tau} \equiv \left[\boldsymbol{\nabla}\boldsymbol{u} + (\boldsymbol{\nabla}\boldsymbol{u})^T \right] - \frac{2}{3}\,(\boldsymbol{\nabla} \cdot \boldsymbol{u})\,\boldsymbol{I},$$

where the identity matrix $\boldsymbol{I}$ has the same matrix dimensions as $\boldsymbol{\nabla}\boldsymbol{u}$ and $\boldsymbol{\tau}$ is the viscous stress tensor. The vector $\hat{\boldsymbol{g}}$ is a unit vector in the direction of $\boldsymbol{g}$, the acceleration due to gravity. The pressures $p^{(0)}$ and $p^{(1)}$ are known as the thermodynamic pressure and hydrodynamic pressure respectively because $p^{(0)}$ is determined by the temperature in the state equation (2.1d) and $p^{(1)}$ is determined by the hydrodynamic forces in the momentum equation (2.1b).

The physical properties μ, λ, R, c_p and γ, described in table 2.1, are assumed to be uniform and constant and can therefore be used directly in the non-dimensional variables and parameters. The Prandtl number Pr expresses a non-dimensional ratio of momentum diffusivity to thermal diffusivity. The parameter S_1 is the ratio of ambient density to jet density, which implies that $S_1 Re$ forms a Reynolds number based on the ambient density instead of the jet density. The Richardson number, Ri expresses a ratio of gravitational potential energy to kinetic energy. For the results in this thesis it is set to zero, but it is carried through the derivation as it may be useful in some cases, such as vertically orientated diffusion flames.

The dimensional equation of state, $\tilde{p} = \tilde{\rho}R\widetilde{T}$, implies that the ambient pressure $\tilde{p}_0$ is equal to $\tilde{\rho}_0 R\widetilde{T}_0$. Together with the definition of non-dimensional pressure, p, in table 2.1, this implies that the non-dimensional ambient pressure $p_0 = \tilde{p}_0/\tilde{\rho}_0 R\widetilde{T}_0 = 1$. Equation (2.1e) implies that $p^{(0)}$ is uniform in space and, assuming that the boundary conditions on $p^{(0)}$ are time independent, $p^{(0)}$ is also constant in time. Under the assumption of low Mach number, $p^{(0)} \approx p$ and we conclude therefore that $p^{(0)} \approx 1$.

Reference quantities:

Ambient density (kg m^{-3}):	$\tilde{\rho}_0$
Ambient temperature (K):	$\widetilde{T}_0$
Jet density (kg m^{-3}):	$\tilde{\rho}_j$
Jet temperature (K):	$\widetilde{T}_j$
Jet diameter (m):	$\tilde{d}_j$
l^2-norm of jet velocity (m s^{-1}):	$\|\tilde{\boldsymbol{u}}_j\| \equiv \tilde{u}_j$
Dynamic viscosity (N m^{-2} s):	μ
Thermal conductivity (W m^{-1} K^{-1}):	λ
Gas constant (J kg^{-1} K^{-1}):	R
Specific heat capacity at constant pressure (J kg^{-1} K^{-1}):	c_p
Ratio of specific heats:	γ
Acceleration due to gravity (m s^{-2}):	$g \equiv \|\boldsymbol{g}\|$

Non-dimensional variables:

Velocity:	$\boldsymbol{u} \equiv \tilde{\boldsymbol{u}}/\tilde{u}_j$
Density:	$\rho \equiv \tilde{\rho}/\tilde{\rho}_0$
Temperature:	$T \equiv \big(\widetilde{T} - \widetilde{T}_0\big)/\big(\widetilde{T}_j - \widetilde{T}_0\big)$
Pressure:	$p \equiv \tilde{p}/\big(\tilde{\rho}_0 R\widetilde{T}_0\big) \approx p^{(0)} + \gamma Ma^2 p^{(1)}$
Time:	$t \equiv \tilde{t}\,\tilde{u}_j/\tilde{d}_j$
Spatial derivatives:	$\boldsymbol{\nabla} \equiv \tilde{d}_j\widetilde{\boldsymbol{\nabla}}$

Non-dimensional parameters:

Mach number:	$Ma \equiv \tilde{u}_j/\big(\gamma R\widetilde{T}_0\big)^{1/2}$
Reynolds number:	$Re \equiv \tilde{\rho}_j\tilde{u}_j\tilde{d}_j/\mu$
Prandtl number:	$Pr \equiv \mu c_p/\lambda$
Richardson number:	$Ri \equiv g\tilde{d}_j/\tilde{u}_j^2$
Density ratio:	$S_1 \equiv \tilde{\rho}_0/\tilde{\rho}_j$

Table 2.1: Non-dimensionalized variables and parameters for non-reacting jets.

The base flow is a steady solution to (2.1) and satisfies

$$\boldsymbol{\nabla} \cdot \bar{\boldsymbol{m}} = 0, \tag{2.2a}$$

$$\boldsymbol{\nabla} \bar{p}^{(1)} - \boldsymbol{\nabla} \cdot \left(\frac{1}{S_1 Re} \bar{\boldsymbol{\tau}} - \bar{\rho} \bar{\boldsymbol{u}} \bar{\boldsymbol{u}} \right) + Ri \left(1 - \bar{\rho} \right) \hat{\boldsymbol{g}} = \boldsymbol{0}, \tag{2.2b}$$

$$\bar{\boldsymbol{m}} \cdot \boldsymbol{\nabla} \bar{T} - \frac{1}{S_1 Re Pr} \nabla^2 \bar{T} = 0, \tag{2.2c}$$

$$\bar{\rho} \left((S_1 - 1) \bar{T} + 1 \right) = 1, \tag{2.2d}$$

$$\bar{\boldsymbol{\tau}} \equiv \left[\boldsymbol{\nabla} \bar{\boldsymbol{u}} + (\boldsymbol{\nabla} \bar{\boldsymbol{u}})^T \right] - \frac{2}{3} \left(\boldsymbol{\nabla} \cdot \bar{\boldsymbol{u}} \right) \boldsymbol{I},$$

$$\bar{\boldsymbol{m}} \equiv \bar{\rho} \bar{\boldsymbol{u}},$$

where $p^{(0)}$ has been replaced by the value 1 in (2.2d). The nonlinear equations (2.1) are linearized about the base flow to form:

$$\frac{\partial \rho'}{\partial t} + \boldsymbol{\nabla} \cdot \boldsymbol{m}' = 0, \tag{2.3a}$$

$$\frac{\partial \boldsymbol{m}'}{\partial t} + \boldsymbol{\nabla} \cdot \left(\bar{\rho} \bar{\boldsymbol{u}} \boldsymbol{u}' + \bar{\rho} \boldsymbol{u}' \bar{\boldsymbol{u}} + \rho' \bar{\boldsymbol{u}} \bar{\boldsymbol{u}} \right) + \boldsymbol{\nabla} p' - \frac{1}{S_1 Re} \boldsymbol{\nabla} \cdot \boldsymbol{\tau}' - Ri \rho' \hat{\boldsymbol{g}} = \boldsymbol{0}, \tag{2.3b}$$

$$\bar{\rho} \frac{\partial T'}{\partial t} + \bar{\rho} \bar{\boldsymbol{u}} \cdot \boldsymbol{\nabla} T' + \boldsymbol{m}' \cdot \boldsymbol{\nabla} \bar{T} - \frac{1}{S_1 Re Pr} \nabla^2 T' = 0, \tag{2.3c}$$

$$\frac{\rho'}{\bar{\rho}} + \frac{(S_1 - 1) T'}{\left((S_1 - 1) \bar{T} + 1 \right)} = 0, \tag{2.3d}$$

$$\boldsymbol{\tau}' \equiv \left[\boldsymbol{\nabla} \boldsymbol{u}' + \left(\boldsymbol{\nabla} \boldsymbol{u}' \right)^T \right] - \frac{2}{3} \left(\boldsymbol{\nabla} \cdot \boldsymbol{u}' \right) \boldsymbol{I}, \tag{2.3e}$$

$$\boldsymbol{m}' \equiv \bar{\rho} \boldsymbol{u}' + \bar{\boldsymbol{u}} \rho', \tag{2.3f}$$

where $\boldsymbol{m}'$ is the linearized momentum and p' is the linear perturbation of $p^{(1)}$. For the rest of this chapter the primes on the direct linear perturbation variables have been dropped for clarity and p refers to the linear perturbation of the hydrodynamic pressure $p^{(1)}$.

2.3   Calculating adjoints

Introducing the direct linear operator, L, the system of linearized perturbation equations, (2.3), can be expressed as

$$\frac{\partial \boldsymbol{q}}{\partial t} - L\boldsymbol{q} = \boldsymbol{0}, \tag{2.4}$$

$$\boldsymbol{q} \equiv \begin{bmatrix} \boldsymbol{m} \\ T \end{bmatrix},$$

where $\boldsymbol{m}$ and T are functions of the axial and radial coordinates, x and r, and time t. The state vector $\boldsymbol{q}$ does not contain p and ρ because these can be derived from $\boldsymbol{m}$ and T using (2.3).

Our main interest is in the global modes of (2.4) and their corresponding frequencies and growth rates. We are therefore interested in non-trivial solutions of (2.4) of the form

$$\boldsymbol{q}\left(x, r, t\right) = \hat{\boldsymbol{q}}\left(x, r\right) \exp\left(\sigma t\right). \tag{2.5}$$

Substituting (2.5) into (2.4), we can write the new system of equations as

$$\sigma \hat{\boldsymbol{q}} - L\hat{\boldsymbol{q}} = \boldsymbol{0}. \tag{2.6}$$

To form the adjoint equations and find the adjoint global modes, (2.6) needs to be rearranged. To achieve this it is useful to define an inner product

$$\langle \boldsymbol{q}_1, \boldsymbol{q}_2 \rangle \equiv \frac{1}{V} \int_V \boldsymbol{q}_1^H \boldsymbol{q}_2 \; dV, \tag{2.7}$$

where $\boldsymbol{q}_1^H$ is the Hermitian of $\boldsymbol{q}_1$. In this notation, $\boldsymbol{q}_1^H \boldsymbol{q}_2 \equiv \sum_i q_{1i}^* q_{2i}$, where superscript $(*)$ denotes the complex conjugate. The adjoint eigenmodes themselves depend on this choice of norm but, when they are recombined with the direct modes to give the sensitivity of the eigenvalue to changes in the operator L, and other robust measures, the effect of the norm cancels out. Using the inner product, (2.6) is premultiplied by an arbitrary vector $\hat{\boldsymbol{q}}^+$, to give:

$$\langle \hat{\boldsymbol{q}}^+, \sigma\hat{\boldsymbol{q}} \rangle - \langle \hat{\boldsymbol{q}}^+, L\hat{\boldsymbol{q}} \rangle = 0. \tag{2.8}$$

The vector $\hat{\boldsymbol{q}}^+$ will soon be identified with the adjoint global mode corresponding to $\hat{\boldsymbol{q}}$. The adjoint global mode can be found before or after (2.8) is discretized and

the two methods, although subtly different, are theoretically equivalent (Giannetti & Luchini, 2007). Discretizing before is labelled the 'discrete-adjoint' approach whereas discretizing after is labelled the 'continuous-adjoint' approach. This distinction is the same as that made by Bewley (2001) between the 'optimize then discretize' (OTD) approach and the 'discretize then optimize' (DTO) approach and also the distinction made by Vogel & Wade (1995) between the 'discretization of the adjoint system' and the 'adjoint of the discrete system'. Giles & Duta (2003) outline some of the programming benefits of the discrete approach in the context of aircraft design and highlight the use of automatic differentiation software that can calculate the discrete-adjoint operator automatically. A review of research on both discrete- and continuous-adjoint design methods for steady flows is given by Newman *et al.* (1999). Sirkes & Tziperman (1997) compare the discrete- and continuous-adjoint approaches when calculating the time-dependent sensitivity of a cost function to initial conditions for an atmospheric system.

2.3.1 Continuous-adjoint approach

General formulation

The continuous-adjoint operator of L is L^+ and is defined implicitly by

$$\left\langle \left(L^+\hat{\boldsymbol{q}}^+\right),\hat{\boldsymbol{q}}\right\rangle \equiv \left\langle \hat{\boldsymbol{q}}^+, L\hat{\boldsymbol{q}}\right\rangle. \qquad (2.9)$$

L^+ can be found by rearranging (2.8) with integration by parts to give:

$$\left\langle \left(\sigma^*\hat{\boldsymbol{q}}^+\right),\hat{\boldsymbol{q}}\right\rangle - \left\langle \left(L^+\hat{\boldsymbol{q}}^+\right),\hat{\boldsymbol{q}}\right\rangle = b. \qquad (2.10)$$

By selecting appropriate boundary conditions, the boundary term b can be set to zero, which means that (2.9) is satisfied. At this point $\hat{\boldsymbol{q}}^+$ can still be an arbitrary vector but, in order for (2.10) to be satisfied for arbitrary $\hat{\boldsymbol{q}}$, $\hat{\boldsymbol{q}}^+$ must satisfy

$$\sigma^*\hat{\boldsymbol{q}}^+ - L^+\hat{\boldsymbol{q}}^+ = \boldsymbol{0}. \qquad (2.11)$$

A vector $\hat{\boldsymbol{q}}^+$ satisfying (2.11) is a global mode of the continuous-adjoint operator L^+ with a corresponding eigenvalue equal to σ^*. Global modes of L^+ will be referred to hereafter as continuous-adjoint global modes and are time-independent solutions of

the system

$$-\frac{\partial \boldsymbol{q}^+}{\partial t} - \mathrm{L}^+ \boldsymbol{q}^+ = \boldsymbol{0}, \tag{2.12}$$

$$\text{where} \quad \boldsymbol{q}^+ \equiv \boldsymbol{q}^+ (x,r,t) \equiv \hat{\boldsymbol{q}}^+ (x,r) \exp\left(-\sigma^* t\right),$$

$$\text{and} \quad \boldsymbol{q}^+ \equiv \begin{bmatrix} \boldsymbol{m}^+ \\ T^+ \end{bmatrix}.$$

The minus sign in front of the time derivative term in (2.12) appears due to the integration by parts of the time derivative term in (2.4). Remembering that adjoint simulations are run backwards in time, t could be replaced with $-t^+$, which would put the adjoint system of (2.11) and (2.12), in a similar form to the direct system of (2.4), (2.5) and (2.6).

Specific formulation

The time derivative terms and continuous-adjoint operator form a set of adjoint equations that are created by successive integration by parts of the set of direct equations (2.3). The exact form of the adjoint equations depends on the exact form of the direct equations. The aim is to find a set of adjoint equations that closely mimics the set of direct equations so that they both can be solved using a similar algorithm. The incompressible and fully-compressible direct Navier–Stokes equations are naturally in a suitable form. The low-Mach-number Navier–Stokes equations, however, are not.

A naive approach would be to apply integration by parts to (2.3). The $\partial \rho / \partial t$ term in (2.3a), however, leads to adjoint equations that require $\partial p^+ / \partial t$ to be approximated from p^+ at the current and previous time steps. This approximation is not present in the direct algorithm and leads to large numerical errors. The direct and adjoint low-Mach-number equations closely mimic one another when the direct equations take

the form

$$(S_1 - 1) \left(\bar{m}_i \frac{\partial \hat{T}}{\partial x_i} - \frac{1}{S_1 RePr} \frac{\partial^2 \hat{T}}{\partial x_i{}^2} \right) + \frac{\partial}{\partial x_i} \left(\frac{\hat{m}_i}{\bar{\rho}} \right) = 0, \tag{2.13a}$$

$$\sigma \hat{m}_i + \frac{\partial}{\partial x_j} \left(\frac{\bar{m}_j \hat{m}_i}{\bar{\rho}} + \frac{\hat{m}_j \bar{m}_i}{\bar{\rho}} - \frac{\hat{\rho} \bar{m}_j \bar{m}_i}{\bar{\rho}^2} \right) + \frac{\partial \hat{p}}{\partial x_i} \cdots$$
$$- \frac{1}{S_1 Re} \left(\frac{\partial^2}{\partial x_j{}^2} \left(\frac{\hat{m}_i}{\bar{\rho}} - \frac{\hat{\rho} \bar{m}_i}{\bar{\rho}^2} \right) + \frac{1}{3} \frac{\partial^2}{\partial x_j \partial x_i} \left(\frac{\hat{m}_j}{\bar{\rho}} - \frac{\hat{\rho} \bar{m}_j}{\bar{\rho}^2} \right) \right) - Ri \hat{\rho} \hat{g}_i = 0, \tag{2.13b}$$

$$\sigma \hat{T} + \frac{\bar{m}_i}{\bar{\rho}} \frac{\partial \hat{T}}{\partial x_i} + \frac{\hat{m}_i}{\bar{\rho}} \frac{\partial \bar{T}}{\partial x_i} - \frac{1}{S_1 RePr} \frac{1}{\bar{\rho}} \frac{\partial^2 \hat{T}}{\partial x_i{}^2} = 0, \tag{2.13c}$$

$$\frac{\hat{\rho}}{\bar{\rho}^2} + (S_1 - 1) \hat{T} = 0. \tag{2.13d}$$

To obtain (2.13) from (2.3) a number of steps have been taken: (2.5) is substituted into (2.3); $\boldsymbol{u}$ and $\boldsymbol{\tau}$ are removed by using (2.3f) and (2.3e); (2.2d) is substituted into (2.3d) to remove $\bar{T}$; (2.3a), (2.3c) and (2.3d) are divided through by $\bar{\rho}$; (2.3d) is differentiated with respect to time and substituted into (2.3c), which is then substituted into (2.3a); and the terms that contain $\hat{m}_i$ in (2.13a) have been combined using (2.2d) to form:

$$(S_1 - 1) \hat{m}_i \frac{\partial \bar{T}}{\partial x_i} + \frac{1}{\bar{\rho}} \frac{\partial \hat{m}_i}{\partial x_i} = \hat{m}_i \frac{\partial}{\partial x_i} \left((S_1 - 1) \bar{T} + 1 \right) + \left((S_1 - 1) \bar{T} + 1 \right) \frac{\partial \hat{m}_i}{\partial x_i}$$
$$= \frac{\partial}{\partial x_i} \left(\frac{\hat{m}_i}{\bar{\rho}} \right). \tag{2.14}$$

If the adjoint variable multiplying (2.13a) is labelled $\hat{p}^+$, then forming the adjoint equations with the terms on the left hand side in (2.14) would result in both $\hat{p}^+$ and $\nabla \hat{p}^+$ appearing in the adjoint momentum equation. This would make the formation and solution of a Poisson equation more difficult. The rearrangement in (2.14) allows the adjoint momentum equation to be formed with just $\nabla \hat{p}^+$ and is therefore necessary for the adjoint Poisson equation to be solved.

Premultiplication of each equation in (2.13) requires the introduction of two extra adjoint variables to premultiply (2.13a) and (2.13d). The labelling of these variables is unimportant, but it is helpful to think of the variable premultiplying (2.13a) as the adjoint pressure and the variable premultiplying (2.13d) as the adjoint density. The adjoint momentum and temperature naturally premultiply (2.13b) and (2.13c) respectively. Through successive integration by parts, the adjoint equations corresponding to

(2.13) are

$$\frac{\partial \hat{m}_i^+}{\partial x_i} = 0, \tag{2.15a}$$

$$\sigma^* \hat{m}_i^+ - \frac{\bar{m}_j}{\bar{\rho}} \left(\frac{\partial \hat{m}_i^+}{\partial x_j} + \frac{\partial \hat{m}_j^+}{\partial x_i} \right) - \frac{1}{S_1 Re \bar{\rho}} \left(\frac{\partial^2 \hat{m}_i^+}{\partial x_j{}^2} + \frac{1}{3} \frac{\partial^2 \hat{m}_j^+}{\partial x_j \partial x_i} \right) - \frac{1}{\bar{\rho}} \frac{\partial \hat{p}^+}{\partial x_i} + \frac{\hat{T}^+}{\bar{\rho}} \frac{\partial \bar{T}}{\partial x_i} = 0, \tag{2.15b}$$

$$\sigma^* \hat{T}^+ - \bar{m}_i \frac{\partial}{\partial x_i} \left(\frac{\hat{T}^+}{\bar{\rho}} + (S_1 - 1) \hat{p}^+ \right) - \dots$$
$$\frac{1}{S_1 Re Pr} \frac{\partial^2}{\partial x_i{}^2} \left(\frac{\hat{T}^+}{\bar{\rho}} + (S_1 - 1) \hat{p}^+ \right) + (S_1 - 1) \hat{\rho}^+ = 0, \tag{2.15c}$$

$$\bar{m}_i \bar{m}_j \frac{\partial \hat{m}_i^+}{\partial x_j} + Ri \bar{\rho}^2 \hat{m}_i^+ \hat{g}_i + \frac{\bar{m}_i}{S_1 Re} \left(\frac{\partial^2 \hat{m}_i^+}{\partial x_j{}^2} + \frac{1}{3} \frac{\partial^2 \hat{m}_j^+}{\partial x_j \partial x_i} \right) + \hat{\rho}^+ = 0. \tag{2.15d}$$

Equation (2.15) shows that $\hat{p}^+$ and $\hat{\rho}^+$ can be derived from $\hat{\boldsymbol{m}}^+$ and $\hat{T}^+$ in the same way as $\hat{p}$ and $\hat{\rho}$ can be derived from $\hat{\boldsymbol{m}}$ and $\hat{T}$ using (2.13).

In forming (2.15c), the base flow condition (2.2a) has been used to shift $\bar{m}_i$ outside the derivative. This ensures that the adjoint pressure appears only inside a derivative, which reduces numerical error because the solution to the adjoint pressure Poisson equation is accurate only up to an arbitrary constant. Alternatively, $\left(\hat{T}/\bar{\rho} \right) \boldsymbol{\nabla} \cdot \bar{\boldsymbol{m}}$ could have been added to the left-hand side of (2.13c). The base flow condition (2.2a) ensures this extra term is approximately zero, but now integration by parts gives (2.15c) directly without requiring any further use of (2.2a). In practice, the forms in (2.13c) and (2.15c) give the smallest discrepancy between the direct and adjoint global mode frequencies and have been used for this work.

2.3.2 Discrete-adjoint approach

Equations (2.4), (2.6) and (2.8) are discretized to give:

$$\frac{\partial \boldsymbol{q}}{\partial t} - \boldsymbol{A} \boldsymbol{q} = \boldsymbol{0}, \tag{2.16}$$

$$\sigma \hat{\boldsymbol{q}} - \boldsymbol{A} \hat{\boldsymbol{q}} = \boldsymbol{0}, \tag{2.17}$$

$$\left(\hat{\boldsymbol{q}}^+ \right)^H \left(\boldsymbol{D} \sigma \hat{\boldsymbol{q}} \right) - \left(\hat{\boldsymbol{q}}^+ \right)^H \left(\boldsymbol{D} \boldsymbol{A} \hat{\boldsymbol{q}} \right) = \boldsymbol{0}, \tag{2.18}$$

where the state vector, $\boldsymbol{q}$, and global mode vector, $\hat{\boldsymbol{q}}$, have changed from continuous functions, $\boldsymbol{q}\left(x, r, t\right)$ and $\hat{\boldsymbol{q}}\left(x, r\right)$, to discrete arrays of vectors located at grid points that

span the domain. Alternatively the continuous scalar fields that form the continuous vectors can be discretized to form separate discrete scalar fields, which are then combined to form discrete vectors of arrays. The matrix $\boldsymbol{A}$ is the discretized version of the direct linear operator L. The diagonal volume distribution matrix $\boldsymbol{D}$ represents the volumes associated with each grid point as a fraction of the total volume of the domain and is required so that the terms in (2.18) are equivalent to the inner products in (2.8). The product $\boldsymbol{q}_1^H \boldsymbol{D} \boldsymbol{q}_2$ represents a discrete volume summation in the same way that the inner product (2.7) represents a volume integral.

To find the discrete-adjoint global mode, each of the terms in (2.18) is rearranged so that the discrete direct global mode alone follows the Hermitian operator:

$$\left(\sigma^* \boldsymbol{D}^H \hat{\boldsymbol{q}}^+\right)^H (\hat{\boldsymbol{q}}) - \left(\boldsymbol{A}^H \boldsymbol{D}^H \hat{\boldsymbol{q}}^+\right)^H (\hat{\boldsymbol{q}}) = \boldsymbol{0}, \tag{2.19}$$

$$\Rightarrow \quad \text{for arbitrary } \hat{\boldsymbol{q}}: \qquad \sigma^* \boldsymbol{D}^H \hat{\boldsymbol{q}}^+ - \boldsymbol{A}^H \boldsymbol{D}^H \hat{\boldsymbol{q}}^+ = \boldsymbol{0}. \tag{2.20}$$

By comparing (2.20) to (2.11) it is clear that the discrete-adjoint global mode, labelled $\hat{\boldsymbol{q}}^\oplus$, is

$$\hat{\boldsymbol{q}}^\oplus \equiv \boldsymbol{D}^H \hat{\boldsymbol{q}}^+, \tag{2.21}$$

$$\Rightarrow \sigma^* \hat{\boldsymbol{q}}^\oplus - \boldsymbol{A}^H \hat{\boldsymbol{q}}^\oplus = \boldsymbol{0}. \tag{2.22}$$

The matrix $\boldsymbol{A}^H$ is the conjugate transpose of $\boldsymbol{A}$. This is different to $\boldsymbol{A}^+$, the discretized version of the continuous adjoint operator L$^+$. The discrete-adjoint global mode $\hat{\boldsymbol{q}}^\oplus$ and eigenvalue σ^* are solutions of the system

$$-\frac{\partial \boldsymbol{q}^\oplus}{\partial t} - \boldsymbol{A}^H \boldsymbol{q}^\oplus = \boldsymbol{0}, \tag{2.23}$$

$$\text{where} \quad \boldsymbol{q}^\oplus \equiv \boldsymbol{q}^\oplus (x, r, t) \equiv \hat{\boldsymbol{q}}^\oplus (x, r) \exp\left(-\sigma^* t\right),$$

$$\text{and} \quad \boldsymbol{q}^\oplus \equiv \begin{bmatrix} \boldsymbol{m}^\oplus \\ T^\oplus \end{bmatrix}.$$

By establishing a rigorous relationship between the discrete- and continuous-adjoint global modes and eigenvalues, the two approaches can be seen to be equivalent. A continuous-adjoint global mode, $\hat{\boldsymbol{q}}^+$, can be found either by using the continuous-adjoint approach or by using the discrete-adjoint approach and converting $\hat{\boldsymbol{q}}^\oplus$ to $\hat{\boldsymbol{q}}^+$ via (2.21).

2.4   Numerical approach

A nonlinear DNS code, provided by Joseph Nichols, is used to obtain a steady solution of the base flow equations and is used as the starting point for the direct linear and adjoint codes. If the flow is unstable, the base flow may be calculated by adding selective frequency damping (SFD) to the nonlinear equations (2.1) (Åkervik *et al.*, 2006). If (2.1) is written as

$$\frac{\partial \boldsymbol{q}}{\partial t} = f(\boldsymbol{q}), \tag{2.24}$$

then adding SFD creates the sytem:

$$\frac{\partial \boldsymbol{q}}{\partial t} = f(\boldsymbol{q}) - \chi(\boldsymbol{q} - \boldsymbol{w}), \tag{2.25}$$

$$\frac{\partial \boldsymbol{w}}{\partial t} = \frac{(\boldsymbol{q} - \boldsymbol{w})}{\Delta}, \tag{2.26}$$

where χ and Δ are control parameters and $\boldsymbol{w}$ is a temporally low-pass filtered solution of $\boldsymbol{q}$. Equation (2.26) is the differential form of an exponential low-pass temporal filter. At a fixed point, $\boldsymbol{w} = \boldsymbol{q}$, and the effect of the SFD terms is nil, but they allow an unstable fixed point to be reached numerically by artificially damping unstable frequencies along the convergence path. To produce the base flows in this thesis, simple time-stepping is used until the SFD system converges to a steady solution that satisfies (2.2).

All versions of the code use sixth-order compact finite difference schemes (Lele, 1992) to compute spatial derivatives in the axial and radial directions. Values along the centreline of the domain are calculated with asymptotic equations (Constantinescu & Lele, 2002) that differ slightly from the regular equations. A 4th-order Runga–Kutta time marching scheme is used, involving an explicit version of the projection method used by Chorin (1968), which requires the solution of a pressure Poisson equation. The Poisson solver uses direct cosine transforms (DCTs) along each line of grid points in the axial direction to decouple the system into separate wave numbers. A standard complex fast Fourier transform (FFT) algorithm is used with pre- and postprocessing routines that allow the efficient computation of two real DCTs for each complex FFT (Cooley *et al.*, 1970; Swarztrauber, 1977; Schumann & Sweet, 1988). The forward DCTs are applied first to the right hand side of the Poisson equation. An efficient algorithm (based on the Thomas algorithm) is then applied to solve the decoupled system of one-dimensional equations. Finally the inverse DCTs are applied to give the pressure.

Further details of the code can be found in Nichols (2005). This section contains a summary of the relevant parts of the direct and adjoint solution algorithms.

2.4.1   Computing global modes

The eigenvalues and global modes are found using ARPACK, which uses the implicitly restarted Arnoldi method (Lehoucq *et al.*, 1998). An introduction to these methods is given by Schmid (2007). ARPACK calculates the eigenvalues and eigenvectors of a virtual time-stepper matrix that represents the evolution of the flow from time t to time $t + N\Delta t$, where Δt is the time advanced by a single application of the time-stepping algorithm and N is the number of applications. If an explicit single-step time discretization is used, such as a Runge–Kutta method, (2.16) and (2.23) can be expressed as

$$q(t + N\Delta t) = M^N q(t), \tag{2.27}$$

$$q^\oplus(t - N\Delta t) = \left(M^H\right)^N q^\oplus(t), \tag{2.28}$$

where M is the matrix exponential of $A\Delta t$, M^H is the matrix exponential of $A^H \Delta t$ and superscript (N) denotes the matrix raised to the power of N.

The continuous-adjoint described by (2.12) is discretized in space and time to give:

$$-\frac{\partial q^+}{\partial t} - A^+ q^+ = 0, \tag{2.29}$$

$$\text{and} \quad q^+(t - N\Delta t) = M^{+N} q^+(t), \tag{2.30}$$

where M^+ is the matrix exponential of $A^+\Delta t$.

The eigenmodes and eigenvalues calculated by ARPACK correspond to the matrices M^N, $(M^H)^N$ and M^{+N}. The eigenmodes are the same as those of the matrices A, A^H and A^+, but the eigenvalues depend on $N\Delta t$. From (2.17), σ is an eigenvalue of A and if λ is the corresponding eigenvalue of M^N then

$$\lambda \equiv \exp\left(\sigma N\Delta t\right), \tag{2.31}$$

$$\Rightarrow \sigma \equiv \frac{1}{N\Delta t}\left(\ln\left(|\lambda|\right) + i\arg\left(\lambda\right)\right), \tag{2.32}$$

where $|\ |$ is the absolute value of a complex number.

A two-sided Arnoldi algorithm, which gives both the direct and adjoint eigenmodes, has been proposed by Ruhe (1983). The two-sided algorithm uses a combination of the approximate left eigenvectors of the direct solution as the initial state for the adjoint calculation. While this improves the speed of convergence of the adjoint algorithm, the use of parallel computing allows the direct and adjoint calculations to be run side by

side and is therefore quicker overall. Giannetti & Luchini (2007) use a two-sided inverse iteration algorithm to efficiently calculate the discrete-adjoint modes at the same time as the direct modes.

2.4.2 Direct linear algorithm

Converting (2.13) into time-dependent form and discretizing in time with a 1st-order explicit Euler scheme, the direct system can be written as

$$\boldsymbol{\nabla} \cdot \boldsymbol{m}_{n+1} - k\,\mathrm{h}(\boldsymbol{m}_{n+1}, T_{n+1}) = 0, \tag{2.33a}$$

$$\frac{\boldsymbol{m}_{n+1} - \boldsymbol{m}_n}{\Delta t} + \boldsymbol{\nabla} p_* - \mathrm{f}(\boldsymbol{m}_n, \rho_n) = \boldsymbol{0}, \tag{2.33b}$$

$$\frac{T_{n+1} - T_n}{\Delta t} - \mathrm{h}(\boldsymbol{m}_n, T_n) = 0, \tag{2.33c}$$

$$\rho_n + kT_n = 0, \tag{2.33d}$$

where f and h are functions representing the remaining terms in the equations and k is a constant scalar field that is dependent upon the base flow. Subscript (n) denotes the value of the variable at time step n and subscript $(*)$ denotes an intermediate value.

The variable ρ_n can be eliminated using (2.33d). The variable p_*, however, requires the formation of a Poisson equation. Taking the divergence of (2.33b) and rearranging gives

$$\nabla^2 p_* = \frac{1}{\Delta t} \left(\boldsymbol{\nabla} \cdot [\boldsymbol{m}_n + \Delta t\,\mathrm{f}(\boldsymbol{m}_n, \rho_n)] - \boldsymbol{\nabla} \cdot \boldsymbol{m}_{n+1} \right). \tag{2.34}$$

The variables T_{n+1} from (2.33c) and $\boldsymbol{m}_n$ are substituted into (2.33a) to give an approximation for $\boldsymbol{\nabla} \cdot \boldsymbol{m}_{n+1}$:

$$\boldsymbol{\nabla} \cdot \boldsymbol{m}_{n+1} \approx k\,\mathrm{h}(\boldsymbol{m}_n, T_{n+1}),$$

$$\Rightarrow \boldsymbol{\nabla} \cdot \boldsymbol{m}_{n+1} \approx (S_1 - 1)\,\bar{\rho}\left(-\boldsymbol{m}_n \cdot \boldsymbol{\nabla}\bar{T} - \bar{\boldsymbol{m}} \cdot \boldsymbol{\nabla} T_{n+1} + \frac{1}{S_1 Re Pr} \nabla^2 T_{n+1} \right). \tag{2.35}$$

The Poisson equation is then solved for p_* and (2.33b) can then be used to find $\boldsymbol{m}_{n+1}$. The term inside the square brackets in (2.34) is the auxiliary momentum

$$\boldsymbol{m}_* = [\boldsymbol{m}_n + \Delta t\,\mathrm{f}(\boldsymbol{m}_n, \rho_n)], \tag{2.36}$$

$$\Rightarrow \boldsymbol{m}_{n+1} = \boldsymbol{m}_* - \Delta t\boldsymbol{\nabla} p_*. \tag{2.37}$$

To improve temporal accuracy the 4th-order Runge–Kutta scheme is used, which is formed from the 1st-order Euler scheme shown above.

2.4.3   Continuous-adjoint algorithm

Converting (2.15) into time-dependent form and discretizing in time with a 1st-order explicit Euler scheme, the continuous-adjoint system can be written as

$$\boldsymbol{\nabla} \cdot \boldsymbol{m}_{n+1}^+ = 0, \tag{2.38a}$$

$$-\left(\frac{\boldsymbol{m}_{n+1}^+ - \boldsymbol{m}_n^+}{\Delta t}\right) - \frac{1}{\bar{\rho}} \boldsymbol{\nabla} p_*^+ + \mathrm{f}^+\left(\boldsymbol{m}_n^+, T_n^+\right) = \boldsymbol{0}, \tag{2.38b}$$

$$-\frac{T_{n+1}^+ - T_n^+}{\Delta t} + \mathrm{h}^+\left(\rho_n^+, T_n^+, p_n^+\right) = 0, \tag{2.38c}$$

$$\rho_n^+ + \mathrm{k}^+\left(\boldsymbol{m}_n^+\right) = 0, \tag{2.38d}$$

where f^+, h^+ and k^+ are functions representing the remaining terms in (2.15b), (2.15c) and (2.15d) respectively.

The derived variable ρ_n^+ can be eliminated by substituting (2.38d) into (2.38c) . The derived variable p_*^+, however, requires the formation of a Poisson equation. Taking the divergence of (2.38b) and rearranging gives

$$\nabla^2 p_*^+ = \frac{1}{\Delta t} \left(\boldsymbol{\nabla} \cdot \left(\bar{\rho} \left[\boldsymbol{m}_n^+ + \Delta t \, \mathrm{f}^+\left(\boldsymbol{m}_n^+, T_n^+\right)\right] \right) - \boldsymbol{m}_{n+1}^+ \cdot \boldsymbol{\nabla}\bar{\rho} - \bar{\rho}\boldsymbol{\nabla} \cdot \boldsymbol{m}_{n+1}^+ \right). \tag{2.39}$$

Equation (2.38a) is used to remove the $\boldsymbol{\nabla} \cdot \boldsymbol{m}_{n+1}^+$ term from (2.39). The remaining $\boldsymbol{m}_{n+1}^+$ is approximated by $\boldsymbol{m}_n^+$ in a similar way to the way in which $\boldsymbol{m}_{n+1}$ is approximated by $\boldsymbol{m}_n$ in (2.35). The adjoint Poisson equation is then solved for p_*^+. The adjoint pressure is then substituted into (2.38) to find $\boldsymbol{m}_{n+1}^+$ and T_{n+1}^+. The term inside the square brackets in (2.39) is the adjoint auxiliary momentum field

$$\boldsymbol{m}_*^+ = \left[\boldsymbol{m}_n^+ + \Delta t \, \mathrm{f}^+\left(\boldsymbol{m}_n^+, T_n^+\right)\right], \tag{2.40}$$

$$\Rightarrow \boldsymbol{m}_{n+1}^+ = \boldsymbol{m}_*^+ - \frac{\Delta t}{\bar{\rho}} \boldsymbol{\nabla} p_*^+. \tag{2.41}$$

In order for the diffusive term in the adjoint momentum equation to be well-behaved it is necessary to use a negative time step, which is achieved by changing the sign in front of terms containing Δt in the above equations. Again, the 4th-order Runge–Kutta scheme is used to improve temporal accuracy.

2.4.4 Discrete-adjoint algorithm

To form a discrete-adjoint algorithm, the direct algorithm needs to be represented as one large matrix, although this matrix is never actually formed. The discrete-adjoint algorithm is formed from the conjugate transpose of this matrix representation. The direct code was not initially written with the discrete-adjoint approach in mind and a matrix representation method, which expands and contracts the state vector, is therefore employed. This method can cope with a wide range of algorithmic structures and has been adapted to transpose accurately, for example, the centreline equations, the Poisson solver and the 4th-order Runga–Kutta scheme.

First, all the steps in the direct solution algorithm are broken down and represented as simple matrix-vector products. At the start of the time step, only the variables contained in the state vector exist. At points in the time step algorithm, derived variables are introduced and the vector grows. When the derived variables are no longer needed they are removed and the vector shrinks, eventually back to the size at which the time step started. For example, the state equation, (2.3d), is represented as a matrix with 4 rows and 3 columns that multiplies the state vector containing three scalar fields: m_x, m_r and T. The top 3 rows of this matrix form a 3×3 identity matrix. The bottom row calculates ρ from a combination of m_x, m_r and T and this forms the fourth field in a new vector containing m_x, m_r, T and ρ. Once ρ is no longer needed a matrix with 3 rows and 4 columns is used to convert back to a three-field vector.

The scalar fields are discretized to form a single state vector containing scalar values. This is achieved by consecutively storing values in the axial direction at each discrete radial location in turn. The middle values for each discretized scalar field correspond therefore to the centreline of the domain. The middle rows of the corresponding matrix represent the centreline equations and the other rows represent the regular equations. Transposing this matrix is most easily achieved by forming one vector with zeros everywhere except at the centreline and another vector, equal to the current state vector, except with zeros only at the centreline. The transposed centreline equations are applied to the first vector and the transposed regular equations are applied to the second vector. The two resulting vectors are then added to form the final state vector for the transposed step.

The compact finite difference scheme (Lele, 1992) solves the system:

$$A \frac{\partial \boldsymbol{q}}{\partial x} = B \boldsymbol{q}, \tag{2.42}$$

where $\boldsymbol{A}$ is tridiagonal. By noting that $\left(\boldsymbol{A}^{-1}\right)^{T} = \left(\boldsymbol{A}^{T}\right)^{-1}$ the transpose of this difference scheme is found by solving

$$\boldsymbol{A}^{T} \boldsymbol{q}_{*}^{\oplus} = \boldsymbol{q}^{\oplus}, \tag{2.43}$$

$$\frac{\partial \boldsymbol{q}^{\oplus}}{\partial x} = \boldsymbol{B}^{T} \boldsymbol{q}_{*}^{\oplus}, \tag{2.44}$$

where $\boldsymbol{q}_{*}^{\oplus}$ is a temporary vector.

For the Poisson solver, the transpose of the matrix representations results in transposed inverse DCTs being applied first, the transposed decoupled Poisson solver being applied next, and transposed forward DCTs being applied last. Conveniently the inverse DCT is similar to the transpose of the forward DCT and the forward DCT is similar to the transpose of the inverse DCT. In both cases, only the value corresponding to the constant coefficient requires altering, which can be easily done in the pre- and postprocessing routines. The decoupled Poisson solver is transposed in a similar way to the way in which the compact difference scheme is transposed.

A matrix representation of the 4th-order Runge–Kutta scheme is formed by expanding the state vector at each of the four steps. At each intermediate Runge–Kutta step the new vector is added to the bottom of the state vector. The last matrix-vector product is then

$$\left[\boldsymbol{q}_{n+1}\right] = \left[\, 0 \;\; \boldsymbol{I}/6 \;\; \boldsymbol{I}/3 \;\; \boldsymbol{I}/3 \;\; \boldsymbol{I}/6 \,\right] \begin{bmatrix} \boldsymbol{q}_{n} \\ \boldsymbol{q}_{n}^{1} \\ \boldsymbol{q}_{n}^{2} \\ \boldsymbol{q}_{n}^{3} \\ \boldsymbol{q}_{n}^{4} \end{bmatrix}. \tag{2.45}$$

The Runge–Kutta matrices can be transposed and reordered accordingly to provide the exact transpose of the whole 4th-order Runga–Kutta algorithm.

The usual way to implement axisymmetry is to mirror the domain about the centreline at the end of the time step. The transpose of this matrix is consequently placed at the start of the time step and sets half of the domain to zero. With this matrix, the adjoint is not axisymmetric. To overcome this, a symmetrical matrix that sets values in the domain to the average value of both sides about the centreline is used at the start and at the end of the time step in both the adjoint and direct algorithms.

A derived boundary value is one that is derived from the values of the state vector that lie inside the boundary. A derived boundary value at a new time step is therefore

independent of the value currently stored at the boundary. Numerical Dirichlet and Neumann boundaries are of this type, whereas a convection boundary is not and relies on the previous value at the boundary. Passing derived boundary values to ARPACK is not only unnecessary, it can be detrimental to convergence. The complete step, from one Arnoldi vector to the next, first applies a matrix that sets the derived boundary values and adds these to the state vector received form ARPACK. The axisymmetry and time-evolution matrices are then applied and finally a matrix is used that removes any derived boundary values from the state vector. Now that the whole matrix sequence has been established it is straightforward to transpose it for the complete discrete-adjoint algorithm.

2.4.5   Boundary conditions

The boundary conditions used for the base flow, direct perturbations and continuous-adjoint perturbations are summarized in table 2.2. The discrete-adjoint boundary conditions are the exact matrix transpose of the discretized direct boundary conditions.

Before discussing the boundary conditions for the different simulations, some general points can be made. Although setting boundary conditions on momentum and temperature is enough information to describe a unique solution (Sani *et al.*, 2006), the efficient solution of the pressure Poisson equation in the projection method requires boundary conditions for the hydrodynamic pressure and auxiliary momentum fields, which must be consistent with the system of equations and the boundary conditions already set.

On the boundaries, the projection steps ((2.37) for the direct case) imply that the auxiliary momentum is equal to the actual momentum plus a multiple of ∇p_*. It is convenient therefore to set $\nabla p_* = 0$, which allows the boundary conditions on the auxiliary momentum to be the same as those for the actual momentum. To set $\nabla p_* = 0$, it is necessary and sufficient to set the spatial derivatives tangential to the boundary $(\partial p_*/\partial \tau)$ and normal to the boundary $(\partial p_*/\partial n)$ to zero, where the spatial co-ordinates τ and n are tangential and normal to the boundary surface respectively. For the axisymmetric case with no swirl and $Re \gg 1$, $\partial p_*/\partial \tau \approx 0$ on all boundaries. Assuming no swirl is necessary because swirl can create a significant pressure drop towards the centreline. A high Reynolds number is required so that viscous corrections near the inlet, which cause a radial pressure gradient at inlet, are small. The solution

of the pressure Poisson equation defines the pressure only to within a constant and the overall pressure level can therefore drift if a Dirichlet condition is not set on part of the pressure boundary. Far from the inlet, where the flow is varying slowly, $\partial p_*/\partial n \approx 0$, allowing a homogeneous-Dirichlet condition to be set explicitly on the lateral and outlet boundaries. $\partial p_*/\partial n = 0$ can then be set as the pressure boundary condition at the inlet. Setting a homogeneous-Neumann pressure condition at the inlet and a homogeneous-Dirichlet condition at the outlet helps generate a pressure build up at start up, which pushes any transients towards the outlet and out of the domain (Joseph Nichols, personal communication).

Field	Base flow			Direct linear			Continuous-adjoint		
	$x=0$	X_{max}	R_{max}	$x=0$	X_{max}	R_{max}	$x=0$	X_{max}	R_{max}
m_x	D	C	v-T-F	h-D	C	h-D	h-D	h-D	h-D
m_r	h-N	C	v-T-F	h-D	C	h-D	h-D	h-D	h-D
T	D	C	h-D	h-D	C	h-D	h-D	h-D	h-D
p	h-N	h-D	h-D	h-N	h-D	h-D	h-D	h-N	h-D
m_{x*}	D	C	v-T-F	h-D	C	h-D	h-D	h-D	h-D
m_{r*}	h-N	C	v-T-F	h-D	C	h-D	h-D	h-D	h-D

Table 2.2: Boundary conditions. D$\rightarrow$ Dirichlet, h-D$\rightarrow$ homogeneous Dirichlet, h-N$\rightarrow$ homogeneous Neumann, C$\rightarrow$ convective, v-T-F$\rightarrow$ viscous traction free.

Base flow boundary conditions

The boundary conditions for the base flow are the same as those used in the nonlinear simulations by Nichols *et al.* (2007). At inlet these are Dirichlet for axial momentum and temperature, with top-hat inlet profiles formed from Michalke's profile number two (Michalke, 1984):

$$y(0,r) \equiv \frac{1}{2}\left(1 + \tanh\left(\frac{1}{4}\frac{\tilde{d}_j}{2\theta}\left(\frac{1}{2r} - 2r\right)\right)\right), \tag{2.46}$$

$$T(0,r) = y(0,r), \tag{2.47}$$

$$\rho(0,r) = \frac{1}{(S_1 - 1)\,T(0,r) + 1}, \tag{2.48}$$

$$m_x(0,r) = \rho(0,r)\Big(u_c + (1 - u_c)\,y(0,r)\Big), \tag{2.49}$$

where θ is the momentum thickness, u_c is the non-dimensional coflow velocity and the non-dimensional jet diameter is 1. A homogeneous-Neumann condition is used for the radial momentum. A small positive coflow velocity helps reduce the accumulation of numerical errors by slowly advecting them out of the domain. With $u_c \ll 1$, however, the inlet conditions approximate a jet exiting from a hole in a flat wall. The lateral boundaries allow fluid entrainment through a viscous traction-free momentum boundary condition and a homogeneous-Dirichlet temperature condition. The outlet boundary is a convection boundary condition for all fields (Gresho, 1991).

Direct linear boundary conditions

The base flow at the inlet and lateral boundaries is assumed to be inwards and a homogeneous-Dirichlet boundary condition is set for the momentum and temperature perturbation fields. This is a restrictive boundary condition, particularly on the inlet plane, where the flow can be absolutely unstable. The flow and geometry upstream of the jet exit plane can make a significant difference (Flavio Giannetti, personal communication) and this will be examined in the future either by including the upstream region or by allowing perturbations to travel upstream through the inlet. Gresho (1991) points out that the convective boundary condition can be used for inlets as well as outlets and that this is sometimes necessary for meaningful results. It may then be beneficial to impose at the jet exit plane a homogeneous-Dirichlet condition outside the jet, mimicking a solid wall, and a convection condition inside the jet, mimicking a hole.

For shorter domains a convection outlet boundary condition is necessary for all perturbation fields to allow disturbances to flow out of the domain with minimal reflections. For long domains a homogeneous-Dirichlet condition can be used if perturbations have reached a small enough amplitude at the exit. If this is the case, a convection condition produces almost identical results, which is why it has been used for all simulations. If needed, a numerical sponge can be used to reduce reflections at the outlet boundary further. Although it has not been tried with this code, a Robin outlet boundary condition used by Ehrenstein & Gallaire (2005) that matches the global mode to a linear approximation of the local dispersion relation at the outlet may reduce unwanted reflections further.

Continuous-adjoint boundary conditions

The boundary terms, arising from the integration by parts in the derivation of the adjoint equations, are represented by b in equation (2.10). Assuming $Re \gg 1$, the boundary terms containing a factor of $1/Re$ can be neglected. The remaining boundary terms forming b are

$$\frac{1}{V}\int_V \frac{\partial}{\partial x_i}\left(\frac{\hat{p}^{+*}\hat{m}_i}{\bar{\rho}}\right) + (S_1 - 1)\frac{\partial}{\partial x_i}\left(\hat{p}^{+*}\hat{T}\bar{m}_i\right) + \frac{\partial}{\partial x_i}\left(\hat{m}_i^{+*}\hat{p}\right) + \frac{\partial}{\partial x_i}\left(\frac{\hat{T}^{+*}\hat{T}\bar{m}_i}{\bar{\rho}}\right)\dots$$

$$+ \frac{\partial}{\partial x_i}\left(\frac{\bar{m}_i\hat{m}_j\hat{m}_j^{+*}}{\bar{\rho}}\right) + \frac{\partial}{\partial x_i}\left(\frac{\hat{m}_i\bar{m}_j\hat{m}_j^{+*}}{\bar{\rho}}\right) + (S_1 - 1)\frac{\partial}{\partial x_i}\left(\hat{T}\bar{m}_i\bar{m}_j\hat{m}_j^{+*}\right)\ dV = 0.$$

(2.50)

Using the divergence theorem the volume integral in (2.50) can be transformed into a surface integral

$$\frac{1}{V}\int_S \left(\frac{\hat{p}^{+*}\hat{m}_i}{\bar{\rho}}\right) + (S_1 - 1)\left(\hat{p}^{+*}\hat{T}\bar{m}_i\right) + \left(\hat{m}_i^{+*}\hat{p}\right) + \left(\frac{\hat{T}^{+*}\hat{T}\bar{m}_i}{\bar{\rho}}\right)\dots$$

$$+ \left(\frac{\bar{m}_i\hat{m}_j\hat{m}_j^{+*}}{\bar{\rho}}\right) + \left(\frac{\hat{m}_i\bar{m}_j\hat{m}_j^{+*}}{\bar{\rho}}\right) + (S_1 - 1)\left(\hat{T}\bar{m}_i\bar{m}_j\hat{m}_j^{+*}\right)\ n_i dS = 0,$$

(2.51)

where n_i is the outward pointing unit normal vector of the surface S.

The flow direction for the adjoint is reversed. The inlet is at X_{max} and the outlet is at $x = 0$. The boundary conditions for the adjoint pressure are therefore also reversed to push any transients out of the domain. p_*^+ is therefore set to zero on $x = 0$, and on $r = R_{max}$. For the axisymmetric case with no swirl, $\partial p_*^+/\partial \tau \approx 0$ on all boundaries, implying $p_*^+ \approx 0$ on X_{max}. $\partial p_*^+/\partial n$ is set to zero on X_{max} and it is still reasonable to assume $\partial p_*^+/\partial n \approx 0$ on R_{max}. The assumption that $\partial p_*^+/\partial n \approx 0$ on $x = 0$ is probably less valid and it may be the cause of some of the discrepancy noticed between the direct and continuous-adjoint results in section 2.6. It has been assumed, however, that $\partial p_*^+/\partial n \approx 0$ on $x = 0$ in order to set $\nabla p_*^+ = 0$ on $x = 0$. An improvement might be found in future by storing $\partial p_*^+/\partial n$ from the previous time step and setting $m_{x*}^+ = m_x^+ + (\Delta t/\bar{\rho})(\partial p_{*(n-1)}^+/\partial n)$ on $x = 0$.

On the lateral boundaries, the homogenous-Dirichlet conditions imposed on all the direct perturbation variables ensure the boundary terms in (2.51) are zero. A convenient choice is to set the same conditions on the adjoint variables. At $x = X_{max}$, a

homogeneous-Dirichlet condition on $\boldsymbol{m}^+$ and T^+, together with $p_*^+ \approx 0$, ensures the boundary terms in (2.51) are approximately zero. At $x = 0$ a homogeneous-Dirichlet condition set on $\boldsymbol{m}^+$ together with the homogeneous-Dirichlet conditions on $\boldsymbol{m}$ and T ensure all the boundary terms in (2.51) are zero. It is also convenient to set a homogeneous-Dirichlet condition on T^+ at $x = 0$.

Unlike at the direct outlet at X_{max}, the adjoint perturbations are large near $x = 0$ and this causes reflections at the homogeneous-Dirichlet boundary condition. If the domain is too short, the reflections set up standing waves between the inlet and outlet. This type of behaviour has also been observed in spatial mixing layers by Buell & Huerre (1988), who suggested that the streamwise boundaries of the finite domain triggered the global resonances.

If a convection condition is used for $\hat{m}_i^+$ at $x = 0$ instead of a homogeneous-Dirichlet condition, the boundary term $(\hat{m}_i^{+*}\hat{p})$ is no longer precisely zero. It is, however, approximately zero, because $\hat{p}$ is approximately zero at $x = 0$. There is also the question of which is physically more correct. The jet is modelled as exiting through a hole in a wall. A wall suggests that no perturbations, adjoint or direct, should pass out through the boundary at the jet exit plane, implying that a homogeneous-Dirichlet condition for the adjoint momentum is appropriate. Inside the jet, however, perturbations could travel upstream of the jet exit plane, implying a convection condition for the adjoint momentum could be more appropriate. In practice it was found that the homogeneous-Dirichlet condition produces continuous-adjoint eigenvalues slightly closer to the direct eigenvalues and so this is the condition that has been used for this work. Although it has not been tested, an adjoint boundary condition that is homogeneous Dirichlet outside the jet and convection inside the jet may have some benefits.

Comparisons between the continuous-adjoint boundary conditions and the discrete-adjoint boundary conditions are difficult because the algorithms in which they are applied are different. In both cases, an approximation of the true adjoint boundary condition is satisfied at the end of the time step. The continuous-adjoint algorithm enforces the boundary conditions directly after the state vector is altered, whereas the discrete-adjoint algorithm applies the transpose of the direct boundary conditions at the start of the time step and then updates the state vector.

2.5   Code validation

To check the direct linear code, the boundary between absolute and convective instability is calculated as S_1 is varied and the results are compared to those of Lesshafft & Huerre (2007). The response to an impulse is calculated in a long domain with a parallel base flow and the energy at the site of the impulse is monitored. The flow parameters of $Re = 1000$ and $R/\theta = 20$ from Lesshafft & Huerre (2007) were used with a non-dimensional domain size of 6.0×84.5 (diameter $\times$ length) with 285×7271 grid points and time step $\Delta t = 0.003$. The energy at the site of the impulse was found to decay for density ratios $S_1 \leqslant 1.61$ and grow for ratios above this. For this flow configuration, the absolute/convective instability boundary in figure 9 of Lesshafft & Huerre (2007) lies at $S_1 \approx 1.54$ (corresponding to $S \approx 0.65$ in their figure). Given the difficulties in using a time marching code to obtain absolute/convective boundaries for parallel flow, this agreement is better than expected. It is likely an improvement could be found if unwanted numerical disturbances could be filtered out. Above a certain time, these disturbances grow too large and dominate the site of the original impulse, despite the impulse response further downstream being many order of magnitudes larger. If these disturbances could be reduced, the true impulse response could be realized for much longer times. It is then likely that the energy at the site of the impulse, for density ratios between 1.54 and 1.61, would eventually start to grow.

A comparison between the direct, discrete-adjoint and continuous-adjoint results is useful to check the validity of all three codes. The three approaches will only match if all three sets of equations and solution algorithms are correctly modelling the flow and if the discretization and boundary errors are small. The discrete-adjoint code was continuously checked during the implementation and debugging process by calculating $\boldsymbol{q}^{\oplus}(t_1) \cdot \boldsymbol{M}^N \boldsymbol{q}(t_2) - \boldsymbol{q}(t_2) \cdot \left(\boldsymbol{M}^H\right)^N \boldsymbol{q}^{\oplus}(t_1)$, which is zero to machine precision. A similar check for the continuous-adjoint code showed fairly small discrepancies, but these were sensitive to the time window represented by $\boldsymbol{M}^N$ and the times t_1 and t_2 and are therefore not conclusive. The discrepancies arise because the numerical scheme of the continuous-adjoint algorithm has different truncation errors to that of the direct algorithm.

Comparing the direct and adjoint eigenvalues and global modes, however, provides a much better validity check. The direct and adjoint global modes from ARPACK were first time marched to check that they kept their form and grew at the predicted rate.

This was always found to be the case. The discrete-adjoint eigenvalues calculated by ARPACK match the direct eigenvalues to the convergence tolerance specified. Figure 2.1 in the next section shows the discrepancy between the largest magnitude eigenvalues for the direct and continuous-adjoint systems to be relatively small. Figures 2.4 and 2.5, and figures 2.7 and 2.6 show that the continuous- and discrete-adjoint global mode shapes are in reasonable agreement for the highest resolution case.

Figures 2.1, 2.7 and 2.6 can also be used to check the resolution. The minimal change between the medium-resolution and high-resolution results suggests the high resolution used is adequate for this problem.

In table 4.1 (in chapter 4), a comparison is made between the eigenvalues of the direct global mode, the results of local analyses and the nonlinear global mode frequencies observed in the numerical study of Nichols & Schmid (2008). The non-reacting frequency calculated by ARPACK is within 4% of the frequencies predicted by the local analysis in this work and the local analysis of Nichols & Schmid. These values, however, are approximately 20% lower than the frequency of the nonlinear global mode, but Nichols & Schmid point out that this in in agreement with the findings of Lesshafft *et al.* (2006). The origins of this discrepancy are discussed in section 4.1.1.

Computations were also carried out to compare the direct linear eigenvalues to the experimental results of Monkewitz *et al.* (1990). This was perhaps slightly ambitious given that the relatively high Reynolds numbers used by Monkewitz *et al.* resulted in near parallel base flows and therefore a highly non-normal linear operator (see section 4.1.1). A further limitation was imposed by the thin shear layer at the nozzle exit that required a higher resolution than previously used. The domain was subsequently shortened to reduce the total number of grid points back to a reasonable level, but this is believed to have led to triggering of numerical global resonances (Buell & Huerre, 1988). Nevertheless the dominant Strouhal numbers predicted by the linear code are comparable to those observed by Monkewitz *et al.*. For $S_1 = 1.333$ a dominant Strouhal number of $St = 0.59$ is predicted by the linear code, which compares to the value of $St \approx 0.3$ observed by Monkewitz *et al.*. For $S_1 = 1.538$ a dominant Strouhal number of $St = 0.57$ is predicted by the linear code, while Monkewitz *et al.* note that the jet seems to flip-flop between two modes with $St \approx 0.3$ and $St \approx 0.45$. ARPACK successfully converged to 10 eigenvalues for each value of S_1. All 20 eigenvalues were of comparable magnitude and frequency, with some of the less dominant eigenvalues giving Strouhal numbers close to 0.3 and 0.45. This finding compares well to those of Monkewitz *et al.*,

who found a number of pressure spectra peaks in the range $0.3 < St < 1.0$.

Taking into account all the validity checks performed, there is nothing to suggest the new non-reacting codes are functioning incorrectly. All the checks have given plausible results for a linear analysis and the discrepancies compared to nonlinear results are within what is expected.

2.6   Results

All the results are at a Reynolds number of 1000. This is large enough to satisfy the assumption that $1/Re \ll 1$, but small enough to allow sufficient spreading of the shear layer over the length of the domain. The Prandtl number is 0.7. The inlet profile has a shear layer thickness parameter $\tilde{d}_j/(2\theta) = 12.5$ and coflow $u_c = 0.01$. The Richardson number is zero and $S_1 = 7.0$. The non-dimensional axial domain length is 36.0 and the non-dimensional domain diameter is 8.0. This setup represents a confinement ratio (domain diameter to jet diameter) of 8, which is large enough for the effects of confinement to be negligible (Juniper, 2008).

Three grid sizes are used: 127×1027 (low-res), 181×1449 (mid-res) and 255×2049 (high-res), corresponding to radial $\times$ axial grid points ($N_r \times N_x$). The corresponding time steps are $\Delta t = 0.00707$ for the high-res simulations and $\Delta t = 0.01$ for the others. The grid is uniform in the axial direction, but skewed in the radial direction to give higher resolution near the shear layers and boundaries.

Figure 2.1 shows the eigenvalues with largest real part (highest growth rate) for the direct, discrete- and continuous-adjoint cases at low-, mid-, and high-res. The direct and discrete-adjoint eigenvalues at each resolution match to 6 decimal places, which is the tolerance specified for the convergence of ARPACK. The imaginary part is equal to $2\pi St$, where $St \equiv \tilde{f}\tilde{d}_j/\tilde{u}_j$ is the Strouhal number and $\tilde{f}$ is the dimensional frequency of the global mode in Hertz. The discrepancy between $\text{Im}(\sigma)$ for the direct and continuous-adjoint systems at each resolution is $\sim 0.1\%$ of $|\sigma|$, whereas the discrepancy between $\text{Re}(\sigma)$ at each resolution is $\sim 1.5\%$ of $|\sigma|$, where $|\;|$ is the absolute value of a complex number.

The base flow is given in figure 2.2. The real part of the most-unstable direct, discrete-adjoint, and continuous-adjoint global modes at high-res are given in figures 2.3, 2.4, and 2.5 respectively. A convention used throughout this work is that if the minimum/maximum values of the figures are stated as 'min'/'max', they also refer to the
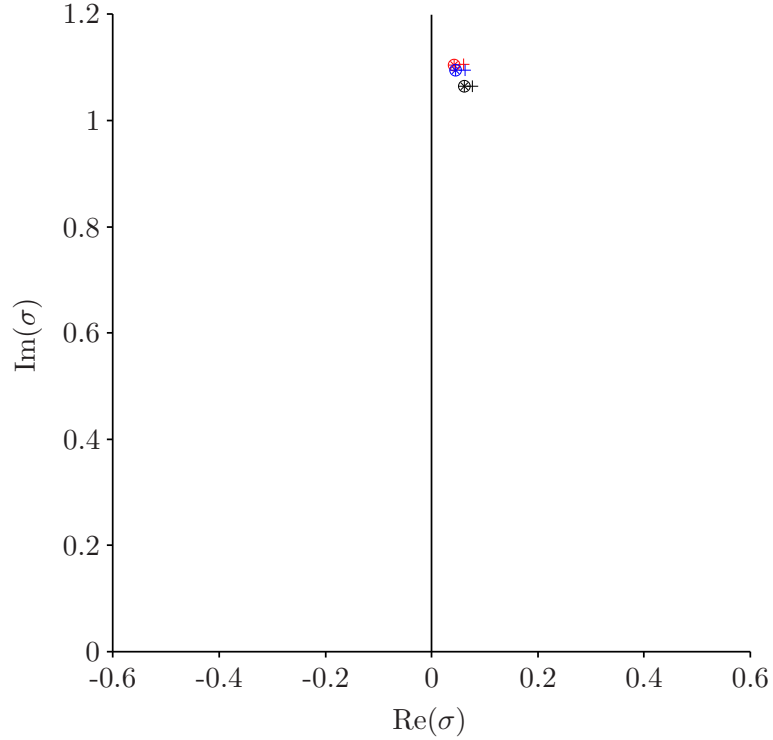
Figure 2.1: Comparison of the most-unstable eigenvalue calculated by the direct ($*$), discrete-adjoint ($\oplus$) and continuous-adjoint ($+$) algorithms using low-res (black), mid-res (blue) and high-res (red). The origin has been included to show the relative magnitudes of the real and imaginary parts of the eigenvalue estimates and to show the size of the discrepancies between the different estimates relative to the magnitude of the eigenvalue.

minimum/maximum values of the data, whereas if they are stated as 'figure min'/'figure max', they refer to the figure values only and differ from the actual minimum/maximum values of the data. In the modal figures, the minimum/maximum values have been set using the value with larger magnitude so that the figure is centred on zero. Only a portion of the domain close to the inlet is shown in figures 2.4 and 2.5 because the low-amplitude downstream structure of the adjoint modes does not show up with the contours used in these figures. The discrete-adjoint mode has been multiplied by $(\boldsymbol{D}^H)^{-1}$ (volume distribution corrected) so that a comparison can be made to the continuous-adjoint mode (see equation (2.21)). The modes have been normalized so that $\langle \hat{\boldsymbol{q}}, \hat{\boldsymbol{q}} \rangle = \langle \hat{\boldsymbol{q}}^+, \hat{\boldsymbol{q}}^+ \rangle = \langle (\boldsymbol{D}^H)^{-1}\hat{\boldsymbol{q}}^{\oplus}, (\boldsymbol{D}^H)^{-1}\hat{\boldsymbol{q}}^{\oplus} \rangle = 1$.
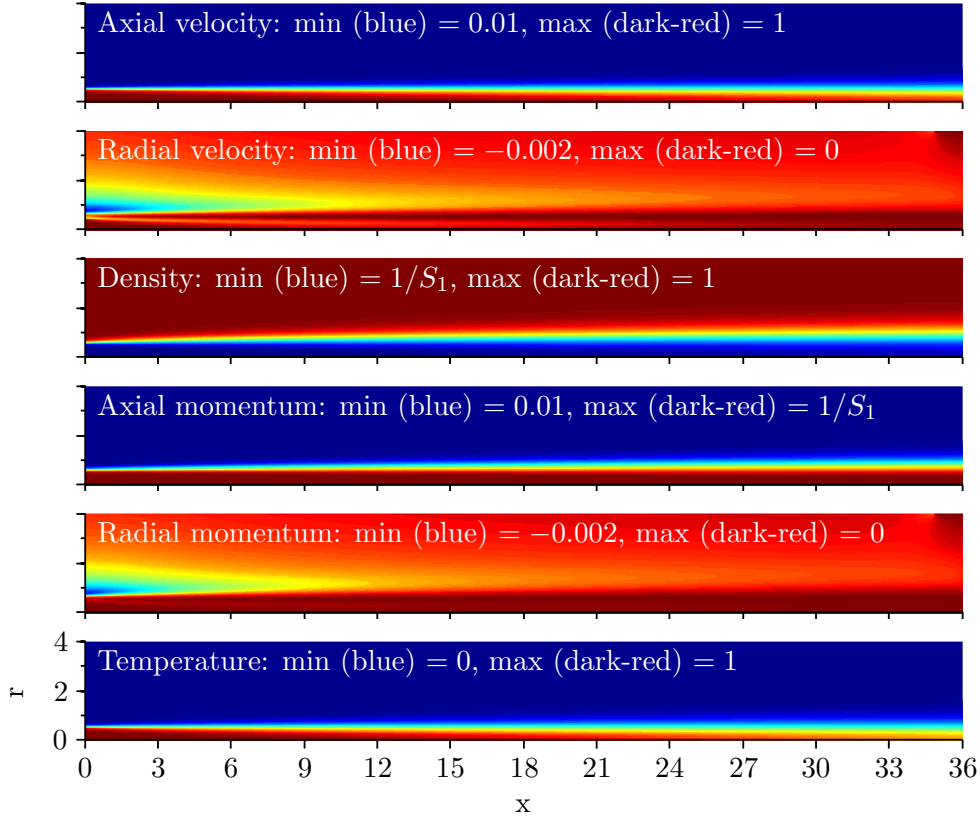
Figure 2.2: Non-dimensional base flow at high resolution.

Figures 2.4 and 2.5 show that the discrete-adjoint mode has a similar structure to the continuous-adjoint mode, but is obscured by a numerical artefact close to the inlet. This nonphysical behaviour near boundaries has been seen by the author in other discrete-adjoint systems and is possibly related to the strong nonphysical behaviour found by Sirkes & Tziperman (1997) when using the discrete-adjoint approach. The maximum and minimum values quoted on the graph are for the normalized amplitude of the physical mode. The numerical spikes near the inlet extend beyond the quoted maximum and minimum and cause the normalized amplitude of the physical mode in the discrete-adjoint case to be lower than in the continuous-adjoint case.

To analyze the adjoint mode structure further downstream it is useful to overlay each adjoint mode field with each corresponding direct mode field by taking the absolute value of their product at every point in the domain. The absolute values of the overlaid fields are shown in figures 2.7 and 2.6. In chapter 4 the physical meaning of this will
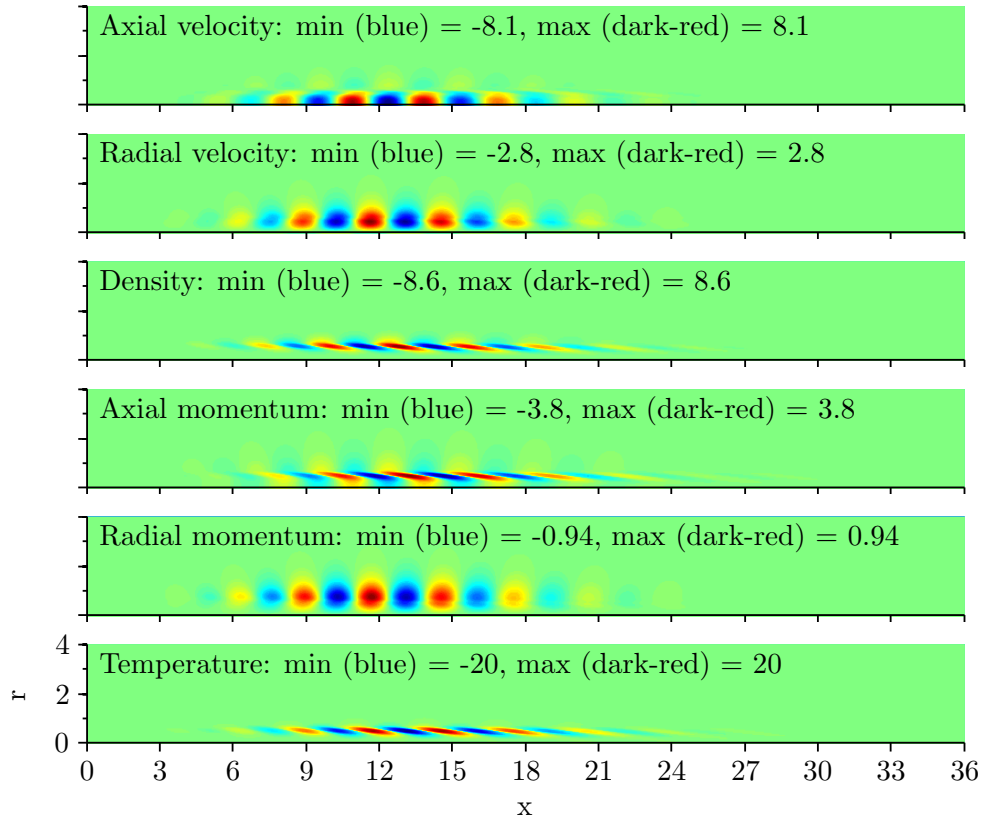
Figure 2.3: Real part of the non-dimensional most-unstable direct global mode at high resolution.

be explored, but at present it provides a useful means of comparing the adjoint mode structure throughout the domain.

The discrepancy between the mid-res and high-res results for both the continuous-adjoint (figure 2.7) and discrete-adjoint (figure 2.6) is quite small, but the discrepancy between the continuous-adjoint and discrete-adjoint results is more significant. In fact the high-res discrete-adjoint mode shape closely resembles the low-res continuous-adjoint mode shape, which suggests the continuous-adjoint global mode is slightly more accurate. The trends shown by the discrete- and continuous-adjoint mode shapes with increasing resolution suggest that further increases may lead to convergence, but this is prohibitively expensive for the length of domain required.

Axial momentum: figure min = -38, figure max = 38

Radial momentum: figure min = -32, figure max = 32

Temperature: figure min = -13, figure max = 13
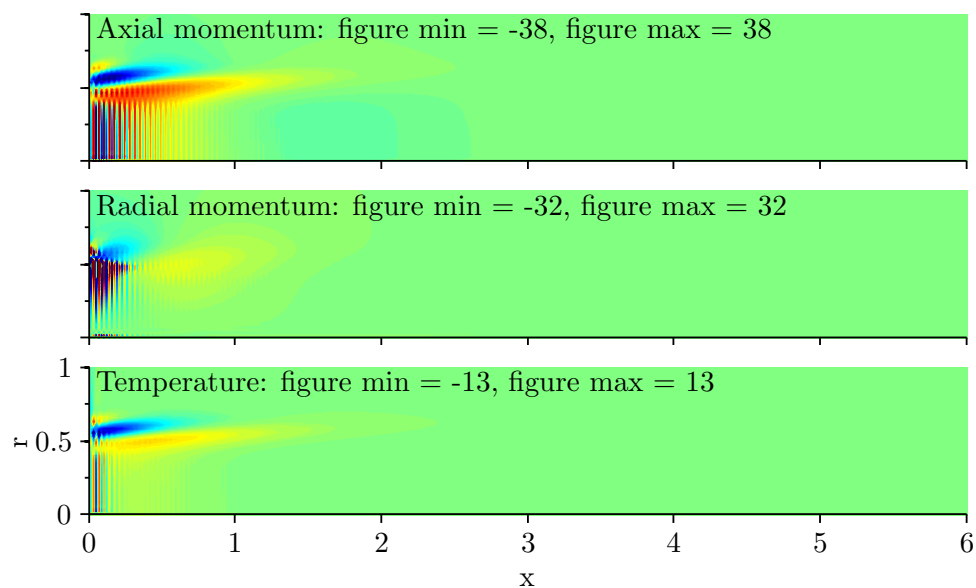
Figure 2.4: Real part of the non-dimensional most-unstable discrete-adjoint global mode at high resolution (volume distribution corrected). Blue regions correspond to minimum values, dark-red regions correspond to maximum values.

Axial momentum: min (blue) = -64, max (dark-red) = 64

Radial momentum: min (blue) = -51, max (dark-red) = 51

Temperature: min (blue) = -18, max (dark-red) = 18
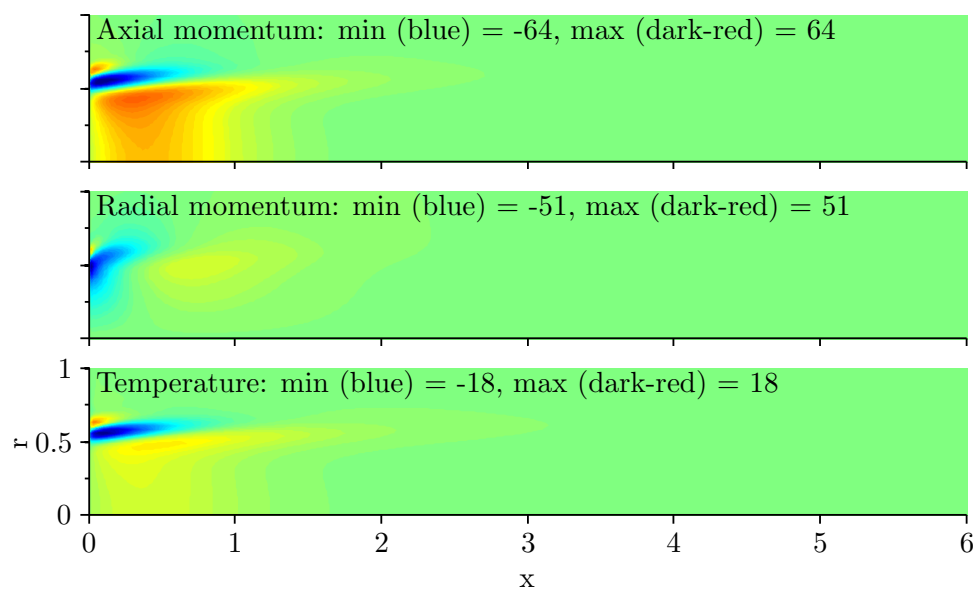
Figure 2.5: Real part of the non-dimensional most-unstable continuous-adjoint global mode at high resolution.
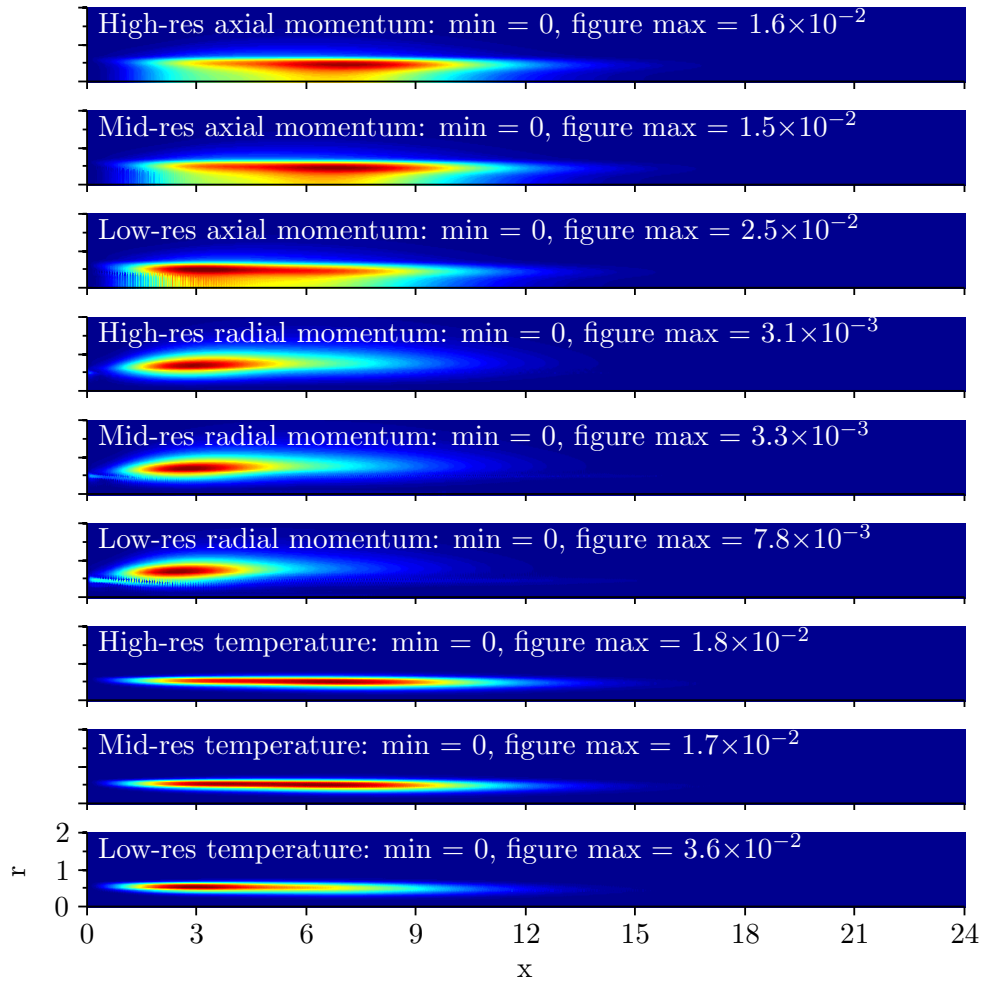
Figure 2.6: Absolute value of the non-dimensional discrete-adjoint global mode multiplied by the direct global mode at every grid point (volume distribution corrected). Blue regions correspond to minimum values, dark-red regions correspond to maximum values.
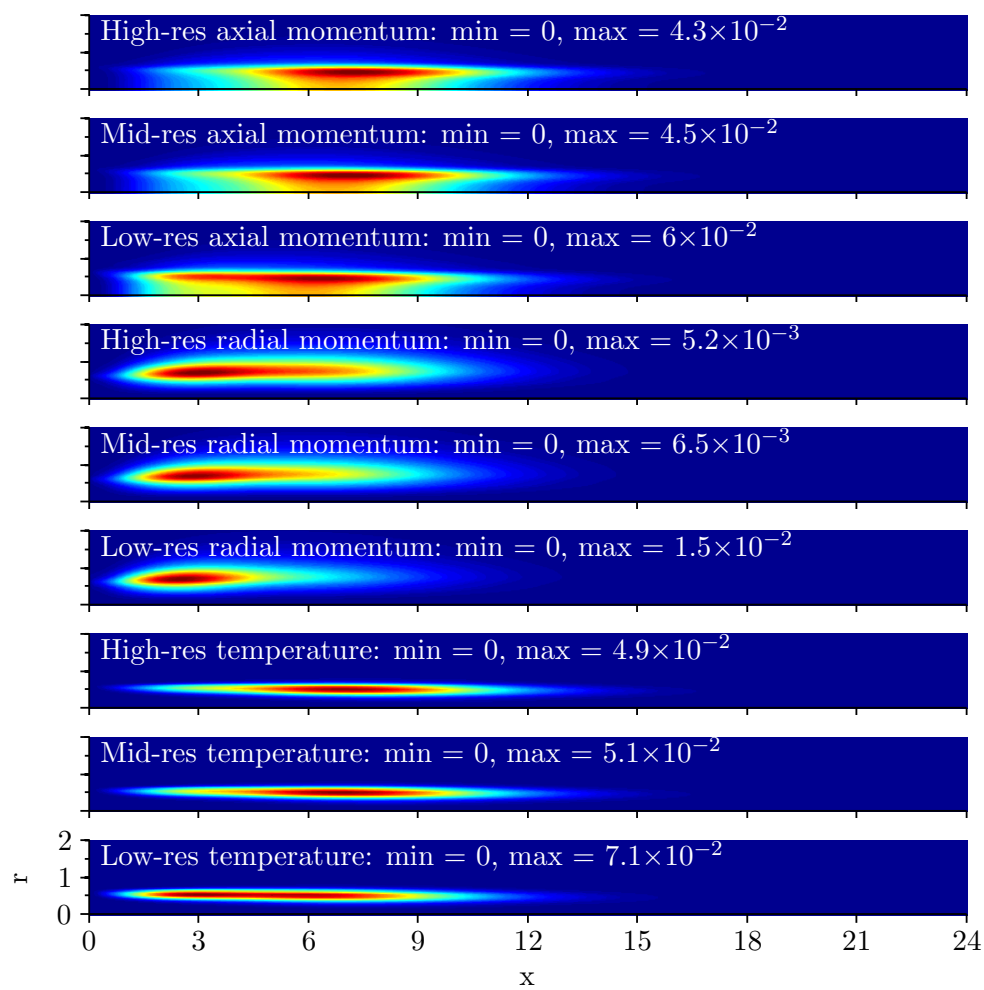
Figure 2.7: Absolute value of the non-dimensional continuous-adjoint global mode multiplied by the direct global mode at every grid point. Blue regions correspond to minimum values, dark-red regions correspond to maximum values.

2.7   Conclusions

The primary goal of the work contained in this chapter was to develop the capability of calculating adjoint global modes for variable density shear flows using a low-Mach-number formulation of the Navier–Stokes equations. Although this capability exists for the incompressible and fully-compressible Navier–Stokes equations, it has not, up until now, existed for the low-Mach-number Navier–Stokes equations. The low-Mach-number formulation can be easily extended to include reaction and there is no need to resolve acoustic length scales, which makes this work a good first step towards creating sensitivity maps for variable-density reacting shear flows.

Due to the treatment of density, the formation of the adjoint equations for the low-Mach-number equations is more complex than for the incompressible or fully-compressible equations. By careful rearrangement of the linear equations, a set of adjoint equations has been derived that can be solved with a similar algorithm. This is essential for the accuracy of the continuous-adjoint solution.

To implement the discrete-adjoint algorithm, a matrix representation method was constructed that expands and contracts the state vector. This method was successfully applied to the entire code and provides an efficient framework to calculate the matrix transpose for a wide range of algorithmic structures, whilst maintaining programming efficiency.

In carrying out the primary investigation, a secondary investigation showed the differences between the continuous-adjoint and discrete-adjoint approaches. It seems that a detailed comparison of the discrete- and continuous-adjoint approaches has not been made before for the calculation of adjoint global modes. The discrete-adjoint approach was formulated in such a way that gives a rigorous relationship between the discrete- and continuous-adjoint global modes and eigenvalues. A direct comparison could then be made between the two.

The small discrepancies between the physically relevant results of the two approaches support the notion that they are theoretically equivalent. While there is a discrepancy of 1.5% between the continuous-adjoint eigenvalue and direct eigenvalue of the most-unstable mode, the continuous-adjoint mode shape is arguably more accurate than the physical part of discrete-adjoint mode shape. The discrete-adjoint mode shape contained strong nonphysical behaviour near the inlet. This reduced with increased resolution, but did not disappear completely in the high resolution case. The

continuous-adjoint numerical scheme requires therefore less resolution and usually converged more quickly than the discrete-adjoint numerical scheme. This, however, is offset by the much harder debugging process and the lack of a reliable test for each procedure in the code.

CHAPTER 3

Jet diffusion flames

3.1   Introduction

The hot jet in chapter 2 is extended to include chemical reaction. The result is a diffusion flame and the particular case considered is that of a lifted diffusion flame as studied by Nichols (2005), Nichols & Schmid (2008) and Nichols *et al.* (2009), who carried out DNS and local analyses to investigate the nature of the self-sustained oscillations that occur in low-density lifted flames.

Lifted diffusion flames are only a small subgroup of the much wider class of diffusion flames, which have been subjected to numerous theoretical, numerical and experimental studies. Kimura (1965) and Toong *et al.* (1965) carried out early experimental studies into diffusion flame instabilities, which were followed by the theoretical work of Buckmaster (1986). The effect of buoyancy on the instability of diffusion flames has been studied experimentally and theoretically by Lingens *et al.* (1996), and numerically by Sato *et al.* (2002). The studies all show that the amount of gravitational acceleration has a significant effect on the instability of the flow, with buoyancy promoting absolute instability. Sripakagorn *et al.* (2004) carried out a DNS study into the extinction and re-ignition in diffusion flames. Of greater interest to the present study are the investigations by Maxworthy (1999) and Juniper *et al.* (2009). Maxworthy experimentally investigates axisymmetric global oscillations in propane diffusion flames and observes the effects of various external modifications. Juniper *et al.* carry out an experimental and numerical study into the effects of external forcing of self-excited round jet diffusion flames.

In a flame, the heat release due to reaction causes local expansion and a reduction

in density in the surrounding fluid. This has significant effects on the hydrodynamic stability of low-density lifted flames. Including heat release from reaction is therefore a necessary and vital next step towards understanding the dynamics of real fuel injectors and combustion chambers.

3.2   Governing equations

The low-Mach-number equations for hot jets are now extended to look at reacting jets. The purpose of this extension is to look at the effect of heat release due to reaction on the stability properties of the jet and, ultimately, to extend adjoint techniques to reacting flows. At this stage, a one-step chemistry model is used with an Arrhenius reaction term. This is sufficient to model the heat release, but avoids the extra complication of multi-step chemistry. (To include multi-step chemistry into the low-Mach-number equations, see Najm *et al.* 1998.) It is also not necessary to model reaction at physical flame length scales, as long as the modelled length scales are small compared to those of the fluid instability.

The problem considered in this analysis is that of a light gaseous fuel exiting through a hole in a wall into an oxidizer. The fuel is at the ambient temperature of the oxidizer at the jet exit and the value of S_1 (the ambient to jet density ratio) is therefore due only to the difference in the densities of the two species. Definitions of new non-dimensional variables and parameters are given in table 3.1. The nonlinear reacting equations, derived by Nichols & Schmid (2008), are

$$\frac{\mathrm{D}\rho}{\mathrm{D}t} + \rho(\boldsymbol{\nabla}\cdot\boldsymbol{u}) = 0, \tag{3.1a}$$

$$\frac{\partial(\rho\boldsymbol{u})}{\partial t} + \boldsymbol{\nabla}p^{(1)} - \boldsymbol{\nabla}\cdot\left(\frac{1}{S_1 Re}\boldsymbol{\tau} - \rho\boldsymbol{u}\boldsymbol{u}\right) + Ri\,(1-\rho)\,\hat{\boldsymbol{g}} = \boldsymbol{0}, \tag{3.1b}$$

$$\rho\frac{\mathrm{D}Z}{\mathrm{D}t} - \frac{1}{S_1 Re\,Sc}\nabla^2 Z = 0, \tag{3.1c}$$

$$\rho\frac{\mathrm{D}T}{\mathrm{D}t} - \frac{1}{S_1 Re\,Pr}\nabla^2 T = Da\rho^3\omega, \tag{3.1d}$$

$$\rho\left((S_1-1)\,Z+1\right)\left((S_2-1)\,T+1\right) = p^{(0)}, \tag{3.1e}$$

$$\boldsymbol{\nabla}p^{(0)} = \boldsymbol{0}, \tag{3.1f}$$

$$\boldsymbol{\tau} \equiv \left[\boldsymbol{\nabla}\boldsymbol{u} + (\boldsymbol{\nabla}\boldsymbol{u})^T\right] - \frac{2}{3}\left(\boldsymbol{\nabla}\cdot\boldsymbol{u}\right)\boldsymbol{I},$$

$$\omega \equiv \left\{\left(Z - \frac{T}{s+1}\right)\left(1 - Z - \frac{sT}{s+1}\right) - \kappa T^2\right\}\exp\left[\frac{-\beta\,(1-T)}{1-\alpha\,(1-T)}\right].$$

Equation (3.1c) describes the convection of mass between the jet and the surroundings and is similar in form to the energy equation for the hot jet. The mixture fraction Z is equivalent to the conserved mass fraction of fuel and has therefore a value 1 for pure fuel and 0 for pure oxidizer. Due to species conservation, after a certain amount of reaction has taken place, Z represents the mass fraction of fuel not yet reacted, Y_F, plus the mass fraction of fuel contained in the product of reaction. If Y_O is the mass fraction of oxidizer not yet reacted and Y_P is the mass fraction of reaction product, then $Y_F + Y_O + Y_P = 1$ and $(1 - Z)$ represents the mass fraction of oxidizer not yet reacted plus the mass fraction of oxidizer contained in the product of reaction. The mass fractions of fuel and oxidizer contained in the product of reaction are $Y_p/(1+s)$ and $sY_P/(1+s)$ respectively, where s is the mass stoichiometric ratio. The Schmidt number Sc expresses the ratio of momentum diffusivity to mass diffusivity, where the product of the local density $\tilde{\rho}$ and local diffusivity D_Z is assumed to be uniform and constant. The similarity between equation (3.1c) and equation (2.1c) for the hot jet is intuitive given that the mixing of a hot jet with cold surroundings is physically similar to the mixing of two species, e.g. a helium jet in air.

The energy equation (3.1d) describes the evolution of a new reduced temperature based on the constant pressure adiabatic flame temperature $\widetilde{T}_f$, which is the temperature reached with complete combustion at constant pressure with no heat loss to the surroundings. Formally $\widetilde{T}_f \equiv \widetilde{T}_0 + \Delta\tilde{h}_P/c_p$, where $\tilde{T}_0$ and c_p are the ambient tempera-

Reference quantities:	
Diffusivity of Z (m^2 s^{-1}):	D_Z
Fuel mass fraction:	Y_F
Oxidizer mass fraction:	Y_O
Product mass fraction:	Y_P
Adiabatic flame temperature (K):	$\widetilde{T}_f$
Activation temperature (K):	$\widetilde{T}_a$
Reaction pre-exponential factor (s^{-1}):	A
Mass stoichiometric ratio:	s
Reversible chemistry equilibrium constant:	κ
Non-dimensional variables:	
Mixture fraction:	$Z \equiv Y_F + Y_P/\left(1+s\right)$
Temperature:	$T \equiv \left(\widetilde{T} - \widetilde{T}_0\right)/\left(\widetilde{T}_f - \widetilde{T}_0\right)$
Non-dimensional parameters:	
Schmidt number:	$Sc \equiv \mu/\left(\tilde{\rho}D_Z\right)$
Damköhler number:	$Da \equiv A\tilde{d}_j/\tilde{u}_j$
Heat release parameter:	$\alpha \equiv \left(\widetilde{T}_f - \widetilde{T}_0\right)/\widetilde{T}_f$
Zeldovich number:	$\beta \equiv \alpha\widetilde{T}_a/\widetilde{T}_f$
Temperature ratio:	$S_2 \equiv \widetilde{T}_f/\widetilde{T}_0$

Table 3.1: Additional non-dimensionalized variables and parameters for reacting jets.

ture and specific heat capacity defined in table 3.1 and $\Delta\tilde{h}_P$ is the enthalpy released per unit mass of product produced. In forming (3.1d), $\Delta\tilde{h}_P$ has been non-dimensionalized with $c_p\left(\widetilde{T}_f - \widetilde{T}_0\right)$ and becomes therefore a factor of unity in front of the reaction rate term $Da\rho^3\omega$. This form is slightly different to that stated in Nichols & Schmid (2008), where ρ^2 is used instead of ρ^3. The ρ^3 form is used in this work because it matches the actual code used in Nichols & Schmid (2008). Given the simplifying assumptions present, a valid argument can be made for either form and both have a physically similar effect on the flow. $Da\rho^3\omega$ is the non-dimensional mass of product produced per unit volume per unit time but, given the non-dimensional enthalpy released per unit mass of product produced is unity, $Da\rho^3\omega$ is equivalent to the non-dimensional enthalpy released per unit volume per unit time or the non-dimensional rate of reaction. The

Damköhler number Da expresses a ratio of the rate of production of reaction product to the rate of fluid convection. The form of ω comes from an Arrhenius law for a simple one-step chemical reaction that assumes one mole of fuel and one mole of oxidizer combine to make two moles of product (for further details see Poinsot & Veynante, 2005).

Assuming $Pr = Sc$, the energy equation (3.1d) takes an identical form to the conservation equation for the mass fraction of reaction product Y_P. Using the same initial and boundary conditions for Y_P and T ensures Y_P is equivalent to T. The variables T and Z can therefore be used to get the mass fractions of unreacted fuel, unreacted oxidizer, and reaction product everywhere in the domain by

$$Y_F \equiv Z - \frac{T}{(1+s)}, \tag{3.2}$$

$$Y_O \equiv 1 - Z - \frac{sT}{(1+s)}, \tag{3.3}$$

$$Y_P \equiv T. \tag{3.4}$$

The state equation, (3.1e), has been altered to include the effects of both species and temperature on density. S_2 is defined as the ratio of $\widetilde{T}_f$ to $\widetilde{T}_0$, which, at constant Z, is equivalent to the ratio of density at temperature $\widetilde{T}_0$ to density at temperature $\widetilde{T}_f$.

The base flow is a steady solution to (3.1) and satisfies

$$\boldsymbol{\nabla} \cdot (\bar{\boldsymbol{m}}) = 0, \tag{3.5a}$$

$$\boldsymbol{\nabla}\bar{p}^{(1)} - \boldsymbol{\nabla} \cdot \left(\frac{1}{S_1 Re}\bar{\boldsymbol{\tau}} - \bar{\rho}\bar{\boldsymbol{u}}\bar{\boldsymbol{u}} \right) + Ri \left(1 - \bar{\rho}\right)\hat{\boldsymbol{g}} = \boldsymbol{0}, \tag{3.5b}$$

$$\bar{\boldsymbol{m}} \cdot \boldsymbol{\nabla}\bar{Z} - \frac{1}{S_1 Re Sc}\nabla^2\bar{Z} = 0, \tag{3.5c}$$

$$\bar{\boldsymbol{m}} \cdot \boldsymbol{\nabla}\bar{T} - \frac{1}{S_1 Re Pr}\nabla^2\bar{T} = Da\bar{\rho}^3\bar{\omega}, \tag{3.5d}$$

$$\bar{\rho}\left((S_1 - 1)\bar{Z} + 1\right)\left((S_2 - 1)\bar{T} + 1\right) = 1, \tag{3.5e}$$

$$\bar{\boldsymbol{\tau}} \equiv \left[\boldsymbol{\nabla}\bar{\boldsymbol{u}} + (\boldsymbol{\nabla}\bar{\boldsymbol{u}})^T\right] - \frac{2}{3}\left(\boldsymbol{\nabla} \cdot \bar{\boldsymbol{u}}\right)\boldsymbol{I},$$

$$\bar{\omega} \equiv \left\{ \left(\bar{Z} - \frac{\bar{T}}{s+1}\right)\left(1 - \bar{Z} - \frac{s\bar{T}}{s+1}\right) - \kappa\bar{T}^2 \right\}\exp\left[\frac{-\beta\left(1 - \bar{T}\right)}{1 - \alpha\left(1 - \bar{T}\right)}\right],$$

$$\bar{\boldsymbol{m}} \equiv \bar{\rho}\bar{\boldsymbol{u}},$$

where it is again assumed that $p^{(1)} = 1$.

The nonlinear equations (3.1) are linearized about the base flow to form

$$\frac{\partial \rho'}{\partial t} + \boldsymbol{\nabla} \cdot \boldsymbol{m}' = 0, \tag{3.6a}$$

$$\frac{\partial \boldsymbol{m}'}{\partial t} + \boldsymbol{\nabla} \cdot \left(\bar{\rho}\bar{\boldsymbol{u}}\boldsymbol{u}' + \bar{\rho}\boldsymbol{u}'\bar{\boldsymbol{u}} + \rho'\bar{\boldsymbol{u}}\bar{\boldsymbol{u}} \right) + \boldsymbol{\nabla}p' - \frac{1}{S_1 Re}\boldsymbol{\nabla} \cdot \boldsymbol{\tau}' - Ri\rho'\hat{\boldsymbol{g}} = \boldsymbol{0}, \tag{3.6b}$$

$$\bar{\rho}\frac{\partial Z'}{\partial t} + \bar{\rho}\bar{\boldsymbol{u}} \cdot \boldsymbol{\nabla}Z' + \boldsymbol{m}' \cdot \boldsymbol{\nabla}\bar{Z} - \frac{1}{S_1 Re Sc}\nabla^2 Z' = 0, \tag{3.6c}$$

$$\bar{\rho}\frac{\partial T'}{\partial t} + \bar{\rho}\bar{\boldsymbol{u}} \cdot \boldsymbol{\nabla}T' + \boldsymbol{m}' \cdot \boldsymbol{\nabla}\bar{T} - \frac{1}{S_1 Re Pr}\nabla^2 T' = Da\left(\bar{\rho}^3\omega' + 3\rho'\bar{\rho}^2\bar{\omega}\right), \tag{3.6d}$$

$$\frac{\rho'}{\bar{\rho}} + \frac{(S_1 - 1)\,Z'}{((S_1 - 1)\,\bar{Z} + 1)} + \frac{(S_2 - 1)\,T'}{((S_2 - 1)\,\bar{T} + 1)} = 0, \tag{3.6e}$$

$$\boldsymbol{\tau}' \equiv \left[\boldsymbol{\nabla}\boldsymbol{u}' + \left(\boldsymbol{\nabla}\boldsymbol{u}'\right)^T\right] - \frac{2}{3}\left(\boldsymbol{\nabla} \cdot \boldsymbol{u}'\right)\boldsymbol{I},$$

$$\omega' \equiv \left\{ \left(1 - 2\bar{Z} - \frac{s-1}{s+1}\bar{T}\right) Z' + \left(2\bar{T}\left(\frac{s}{(s+1)^2} - \kappa\right) - \frac{1 + (s-1)\,\bar{Z}}{s+1}\right) T' \ldots \right.$$

$$\left. + \left[\left(\bar{Z} - \frac{\bar{T}}{s+1}\right)\left(1 - \bar{Z} - \frac{s\bar{T}}{s+1}\right) - \kappa\bar{T}^2\right] \frac{\beta T'}{\left(1 - \alpha\left(1 - \bar{T}\right)\right)^2} \right\} \exp\left[\frac{-\beta\left(1 - \bar{T}\right)}{1 - \alpha\left(1 - \bar{T}\right)}\right],$$

$$\boldsymbol{m}' \equiv \bar{\rho}\boldsymbol{u}' + \bar{\boldsymbol{u}}\rho'.$$

The exponential part of ω is linearized by taking a binomial expansion of the denominator inside the exponential and then taking a power series expansion of the exponential itself. It is worth pointing out that the exponential in the reaction rate term makes the linearized reaction rate term very sensitive to $\bar{T}$.

3.3   Adjoint equations

Removing primes for clarity and following a similar method to the one used for the non-reacting case, the linear equations (3.6) are rearranged in the form

$$\bar{K}_1 \left(\bar{m}_i \frac{\partial T}{\partial x_i} - \frac{1}{S_1 Re Pr} \frac{\partial^2 T}{\partial x_i{}^2} - Da\bar{\rho}^2 \left(\bar{\rho}\bar{K}_Z Z + \bar{\rho}\bar{K}_T T + 3\bar{\omega}\rho \right) \right) \dots$$

$$+ \bar{K}_2 \left(\bar{m}_i \frac{\partial Z}{\partial x_i} - \frac{1}{S_1 Re Sc} \frac{\partial^2 Z}{\partial x_i{}^2} \right) + \frac{\partial}{\partial x_i} \left(\frac{m_i}{\bar{\rho}} \right) = 0, \tag{3.7a}$$

$$\frac{\partial m_i}{\partial t} + \frac{\partial}{\partial x_j} \left(\frac{\bar{m}_j m_i}{\bar{\rho}} + \frac{m_j \bar{m}_i}{\bar{\rho}} - \frac{\rho \bar{m}_j \bar{m}_i}{\bar{\rho}^2} \right) + \frac{\partial p}{\partial x_i} \dots$$

$$- \frac{1}{S_1 Re} \left(\frac{\partial^2}{\partial x_j{}^2} \left(\frac{m_i}{\bar{\rho}} - \frac{\rho \bar{m}_i}{\bar{\rho}^2} \right) + \frac{1}{3} \frac{\partial^2}{\partial x_j \partial x_i} \left(\frac{m_j}{\bar{\rho}} - \frac{\rho \bar{m}_j}{\bar{\rho}^2} \right) \right) - Ri\rho \hat{g}_i = 0, \tag{3.7b}$$

$$\frac{\partial Z}{\partial t} + \frac{\bar{m}_i}{\bar{\rho}} \frac{\partial Z}{\partial x_i} + \frac{m_i}{\bar{\rho}} \frac{\partial \bar{Z}}{\partial x_i} - \frac{1}{S_1 Re Sc \bar{\rho}} \frac{\partial^2 Z}{\partial x_i{}^2} = 0, \tag{3.7c}$$

$$\frac{\partial T}{\partial t} + \frac{\bar{m}_i}{\bar{\rho}} \frac{\partial T}{\partial x_i} + \frac{m_i}{\bar{\rho}} \frac{\partial \bar{T}}{\partial x_i} - \frac{1}{S_1 Re Pr \bar{\rho}} \frac{\partial^2 T}{\partial x_i{}^2} - Da\bar{\rho} \left(\bar{\rho}\bar{K}_Z Z + \bar{\rho}\bar{K}_T T + 3\bar{\omega}\rho \right) = 0, \tag{3.7d}$$

$$\frac{\rho}{\bar{\rho}^2} + \bar{K}_1 T + \bar{K}_2 Z = 0, \tag{3.7e}$$

where $\bar{K}_1$, $\bar{K}_2$, $\bar{K}_Z$ and $\bar{K}_T$ are constant scalar fields given by

$$\bar{K}_1 \equiv (S_2 - 1) \left((S_1 - 1) \bar{Z} + 1 \right), \tag{3.8}$$

$$\bar{K}_2 \equiv (S_1 - 1) \left((S_2 - 1) \bar{T} + 1 \right), \tag{3.9}$$

$$\bar{K}_Z \equiv \left(1 - 2\bar{Z} - \frac{s-1}{s+1}\bar{T} \right) \exp \left[\frac{-\beta \left(1 - \bar{T} \right)}{1 - \alpha \left(1 - \bar{T} \right)} \right], \tag{3.10}$$

$$\bar{K}_T \equiv \left\{ \left[\left(\bar{Z} - \frac{\bar{T}}{s+1} \right) \left(1 - \bar{Z} - \frac{s\bar{T}}{s+1} \right) - \kappa \bar{T}^2 \right] \frac{\beta}{\left(1 - \alpha \left(1 - \bar{T} \right) \right)^2} \dots$$

$$+ 2\bar{T} \left(\frac{s}{(s+1)^2} - \kappa \right) - \frac{1 + (s-1)\bar{Z}}{s+1} \right\} \exp \left[\frac{-\beta \left(1 - \bar{T} \right)}{1 - \alpha \left(1 - \bar{T} \right)} \right]. \tag{3.11}$$

In a similar way to the non-reacting system of equations, the term containing m_i in

(3.7a) has been formed by using (3.5c):

$$
\bar{K}_1 m_i \frac{\partial \bar{T}}{\partial x_i} + \bar{K}_2 m_i \frac{\partial \bar{Z}}{\partial x_i} + \frac{1}{\bar{\rho}} \frac{\partial m_i}{\partial x_i}
$$

$$
= (S_2 - 1)\left((S_1 - 1)\bar{Z} + 1\right) m_i \frac{\partial \bar{T}}{\partial x_i} \dots
$$

$$
\qquad + (S_1 - 1)\left((S_2 - 1)\bar{T} + 1\right) m_i \frac{\partial \bar{Z}}{\partial x_i} + \left((S_1 - 1)\bar{Z} + 1\right)\left((S_2 - 1)\bar{T} + 1\right) \frac{\partial m_i}{\partial x_i},
$$

$$
= \left((S_1 - 1)\bar{Z} + 1\right) m_i \frac{\partial}{\partial x_i}\left((S_2 - 1)\bar{T} + 1\right) \dots
$$

$$
\qquad + \left((S_2 - 1)\bar{T} + 1\right) m_i \frac{\partial}{\partial x_i}\left((S_1 - 1)\bar{Z} + 1\right) + \left((S_1 - 1)\bar{Z} + 1\right)\left((S_2 - 1)\bar{T} + 1\right) \frac{\partial m_i}{\partial x_i},
$$

$$
= \frac{\partial}{\partial x_i}\left(\frac{m_i}{\bar{\rho}}\right).
$$

The set of direct reacting equations in the form of (3.7) provides the best known rearrangement to produce a set of adjoint equations that are similar in form. The rearrangement in (3.7) is also very similar to the best rearrangement found for the non-reacting system (2.13). The corresponding adjoint equations, formed using the same method as in the non-reacting case, are

$$
\frac{\partial m_i^+}{\partial x_i} = 0, \tag{3.12a}
$$

$$
-\frac{\partial m_i^+}{\partial t} - \frac{\bar{m}_j}{\bar{\rho}}\left(\frac{\partial m_i^+}{\partial x_j} + \frac{\partial m_j^+}{\partial x_i}\right) - \frac{1}{S_1 Re \bar{\rho}}\left(\frac{\partial^2 m_i^+}{\partial x_j^2} + \frac{1}{3}\frac{\partial^2 m_j^+}{\partial x_j \partial x_i}\right) \dots
$$
$$
-\frac{1}{\bar{\rho}}\frac{\partial p^+}{\partial x_i} + \frac{T^+}{\bar{\rho}}\frac{\partial \bar{T}}{\partial x_i} + \frac{Z^+}{\bar{\rho}}\frac{\partial \bar{Z}}{\partial x_i} = 0, \tag{3.12b}
$$

$$
-\frac{\partial Z^+}{\partial t} - \bar{m}_i \frac{\partial}{\partial x_i}\left(\frac{Z^+}{\bar{\rho}} + \bar{K}_2 p^+\right) - \frac{1}{S_1 Re Sc}\frac{\partial^2}{\partial x_i^2}\left(\frac{Z^+}{\bar{\rho}} + \bar{K}_2 p^+\right) \dots
$$
$$
- Da \bar{\rho}^3 \bar{K}_Z \left(\frac{T^+}{\bar{\rho}} + \bar{K}_1 p^+\right) + \bar{K}_2 \hat{\rho}^+ = 0, \tag{3.12c}
$$

$$
-\frac{\partial T^+}{\partial t} - \bar{m}_i \frac{\partial}{\partial x_i}\left(\frac{T^+}{\bar{\rho}} + \bar{K}_1 p^+\right) - \frac{1}{S_1 Re Pr}\frac{\partial^2}{\partial x_i^2}\left(\frac{T^+}{\bar{\rho}} + \bar{K}_1 p^+\right) \dots
$$
$$
- Da \bar{\rho}^3 \bar{K}_T \left(\frac{T^+}{\bar{\rho}} + \bar{K}_1 p^+\right) + \bar{K}_1 \hat{\rho}^+ = 0, \tag{3.12d}
$$

$$
\bar{m}_i \bar{m}_j \frac{\partial m_i^+}{\partial x_j} + Ri \bar{\rho}^2 m_i^+ \hat{g}_i + \frac{\bar{m}_i}{S_1 Re}\left(\frac{\partial^2 m_i^+}{\partial x_j^2} + \frac{1}{3}\frac{\partial^2 m_j^+}{\partial x_j \partial x_i}\right) \dots
$$
$$
- 3 Da \bar{\rho}^4 \bar{\omega}\left(\frac{T^+}{\bar{\rho}} + \bar{K}_1 p^+\right) + \rho^+ = 0. \tag{3.12e}
$$

3.4   Changes to the non-reacting code

Despite the extra variables and equations, only minimal changes were required to implement the reacting system in the direct linear and discrete-adjoint codes. A nonlinear code provided by Joseph Nichols was used for nonlinear time stepping and to compute the base flow fields.

In the direct and discrete-adjoint codes the scalar fields Z and T are stored together as a vector field. The time evolution algorithms for both fields are very similar and it is possible to use the same subroutines, by just changing the input variables. This is achieved by a simple loop changing the index of the of the vector field from 1 to 2 to access Z and T. The new discrete-adjoint code follows the changes to the direct code exactly. This results in linear and discrete-adjoint codes that can be switched between non-reacting and reacting flows by changing the size of the vector field from 1 to 2 respectively.

Direct-linear and discrete-adjoint reacting codes have been developed. The discrete-adjoint approach was chosen ahead of the continuous-adjoint approach due to the fewer changes required and because it is easier to debug. The required resolution for reacting simulations is greater than that for non-reacting simulations in order to resolve the smaller flame length scales. For the reacting simulations used in this work, the resolution is approximately 1.6 times greater than that used in the high-resolution non-reacting simulations. Given the reasonable comparison between the discrete-adjoint and continuous-adjoint approaches in the high-resolution non-reacting case, it is assumed that the hydrodynamics in the reacting adjoint modes are sufficiently resolved using the discrete-adjoint method for the purpose of this work.

Field	Base flow			Direct linear		
	$x = 0$	X_{max}	R_{max}	$x = 0$	X_{max}	R_{max}
T	h-D	C	h-D	h-D	C	h-D
Z	D	C	h-D	h-D	C	h-D

Table 3.2:   Boundary condition changes for the reacting jet.   D→ Dirichlet, h-D→ homogeneous Dirichlet, C→ convective.

Changes to the boundary conditions for the reacting case are given in table 3.2. The base flow inlet boundary condition on temperature is now homogeneous Dirichlet

and top-hat inlet profiles, formed from Michalke's profile number two (Michalke, 1984), are used for the base flow momentum and mixture fraction:

$$y(0,r) \equiv \frac{1}{2}\left(1 + \tanh\left(\frac{1}{4}\frac{\tilde{d}_j}{2\theta}\left(\frac{1}{2r} - 2r\right)\right)\right), \qquad (3.13)$$

$$Z(0,r) = y(0,r), \qquad (3.14)$$

$$T(0,r) = 0 \ \Rightarrow \ \rho(0,r) = \frac{1}{(S_1 - 1)\,Z(0,r) + 1}, \qquad (3.15)$$

$$m_x(0,r) = \rho(0,r)\Big(u_c + (1 - u_c)\,y(0,r)\Big). \qquad (3.16)$$

For the reacting base flow, the numerical simulation needs to be ignited. This is achieved by using a Gaussian-shaped impulse of magnitude 1 at $r = \pm 0.5$ in the temperature initial condition.

3.5   Code validation

The first check for the reacting code was to set the Damköhler number to zero and apply the initial and boundary conditions used for the non-reacting results to the momentum and temperature fields. Setting initial and boundary conditions on the mixture fraction to zero then led to the non-reacting results being recovered.

Using the same conditions as Nichols & Schmid (2008), table 4.1 in chapter 4 compares the eigenvalues of the direct global modes calculated in this chapter to results from local analyses and the nonlinear global mode frequencies observed in the numerical study of Nichols & Schmid (2008). The reacting case with liftoff height $h_l = 0.858$ is equivalent to the 'marginally stable' case in Nichols & Schmid (2008) with $Da = 6 \times 10^5$. The discrepancy between the frequency calculated by ARPACK and the frequency of the nonlinear global mode is approximately 10%, which is a reasonable agreement. The frequencies predicted by the local analyses in this case are significantly lower.

The discrete-adjoint code was continuously checked during the implementation and debugging process by comparing $\boldsymbol{q}^{\oplus}(t_1) \cdot \boldsymbol{M}^N \boldsymbol{q}(t_2)$ to $\boldsymbol{q}(t_2) \cdot \left(\boldsymbol{M}^H\right)^N \boldsymbol{q}^{\oplus}(t_1)$, which match to machine precision. The discrete-adjoint eigenvalues calculated by ARPACK match the direct eigenvalues to the convergence tolerance specified.

The domain size, resolution and flow parameters are identical to those used by Nichols & Schmid (2008). The resolution is also approximately 1.6 times that used in

the high resolution non-reacting simulations.

Taking these checks into account, there is nothing to suggest the new reacting codes are functioning incorrectly. All the checks have given plausible results for a linear analysis and the discrepancies with the nonlinear results are reasonably small.

3.6   Results
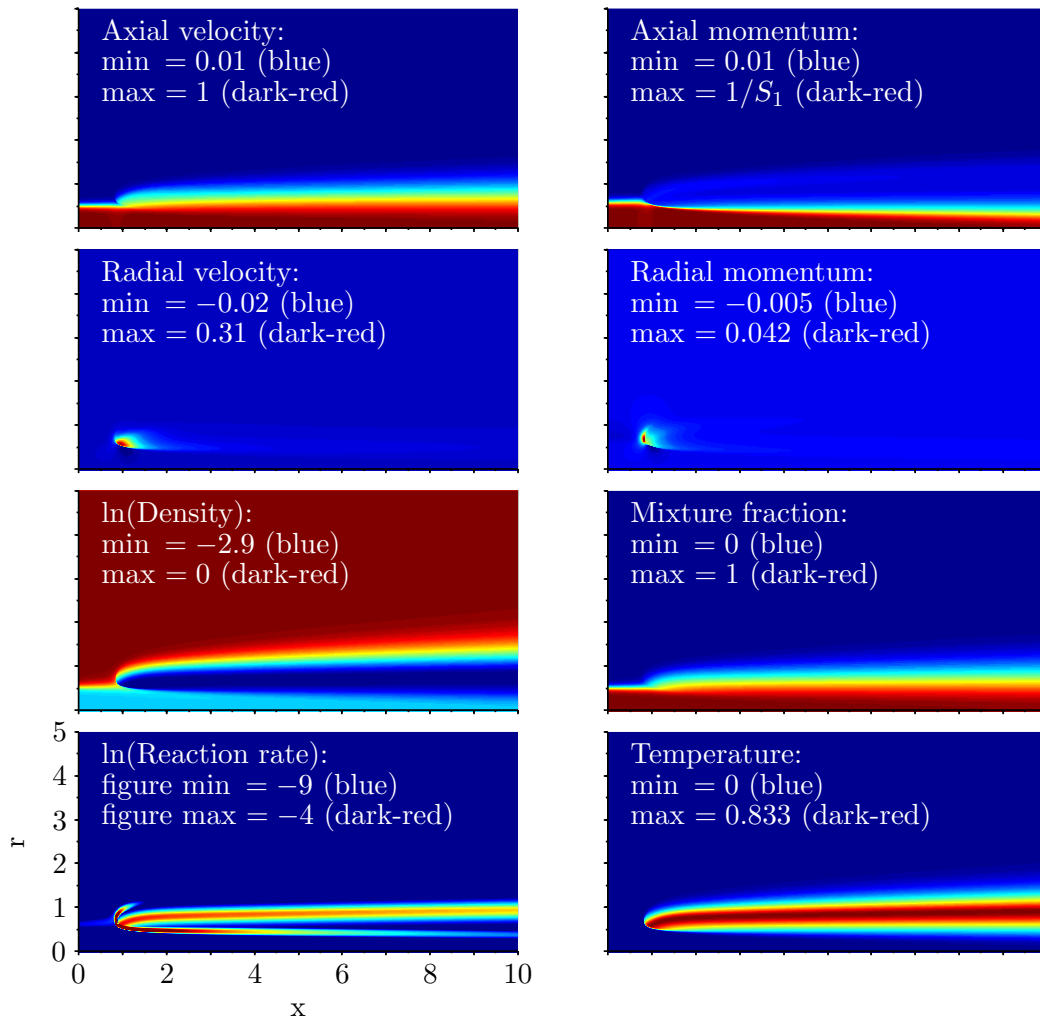
Figure 3.1: Non-dimensional reacting base flow.

The flow parameters used are the same as those used in the non-reacting results. The extra parameters needed are set to those used by Nichols & Schmid (2008), these

are: $s = 2$, $\kappa = 0.01$, $Sc = 0.7$, $Da = 6 \times 10^5$, $S_2 = 6.0$, $\alpha = 1 - 1/S_2 = 0.833$, $\beta = 3$. The highly non-parallel nature of the lifted flame allows for a much shorter domain than that used in the non-reacting case. The non-dimensional axial domain length is 10.0 and the non-dimensional domain diameter is 10.0. The grid size is 511×1025, corresponding to radial $\times$ axial grid points ($N_r \times N_x$), with time step $\Delta t = 0.0025$. With $Da = 6 \times 10^5$, this set up exactly matches that of the marginally stable ($Da = 6 \times 10^5$) case in the nonlinear simulations of Nichols & Schmid.

A steady base flow (figure 3.1), calculated with selective frequency damping (Åkervik *et al.*, 2006), with an initial spark at $x = 2$ and $r = \pm 0.5$, converged to a liftoff height $h_l = 0.858$, which approximately matches that found in Nichols & Schmid (2008). The small discrepancy is due to the definition of the flame base; in the present work this is taken to be the position of the most upstream point of the $T = 0.6$ contour line.

The base flow fields in figure 3.1 show that a large change occurs in the spanwise profiles between the pre-mixing zone and flame region for all fields. Nichols & Schmid (2008) showed that a pocket of absolute instability exists in the pre-mixing zone and that for sufficiently large liftoff heights this pocket of absolute instability leads to global oscillations. This suggests that the instability develops in the pre-mixing zone and it is likely therefore that the most sensitive region of the flow is also in the pre-mixing zone. This topic is covered in greater depth in chapter 4.

A convention used throughout this work is that if the minimum/maximum values of the figures are stated as 'min'/'max', they also refer to the minimum/maximum values of the data, whereas if they are stated as 'figure min'/'figure max', they refer to the figure values only and differ from the actual minimum/maximum values of the data. In the modal figures, the minimum/maximum values have been set using the value with larger magnitude so that the figure is centred on zero.

The real parts of the most-unstable direct and discrete-adjoint global modes are given in figures 3.2, and 3.3. The discrete-adjoint mode has been multiplied by $(\boldsymbol{D}^H)^{-1}$ (volume distribution corrected). The modes have been normalized so that $\langle \hat{\boldsymbol{q}}, \hat{\boldsymbol{q}} \rangle = 1$ and $\langle (\boldsymbol{D}^H)^{-1}\hat{\boldsymbol{q}}^\oplus, (\boldsymbol{D}^H)^{-1}\hat{\boldsymbol{q}}^\oplus \rangle = 1$. The eigenvalue corresponding to this mode is $\sigma = -0.0939 + \mathrm{i}\,1.981$. The small negative real part of this eigenvalue implies that the mode is slowly decaying over time. The Strouhal number is $St = \mathrm{Im}(\sigma)/(2\pi) = 0.315$, which is within approximately 10% of the nonlinear Strouhal number ($St = 0.284$) observed by Nichols & Schmid for the marginally stable case.

While the direct mode shape is most dominant in the flame (figure 3.2), the adjoint
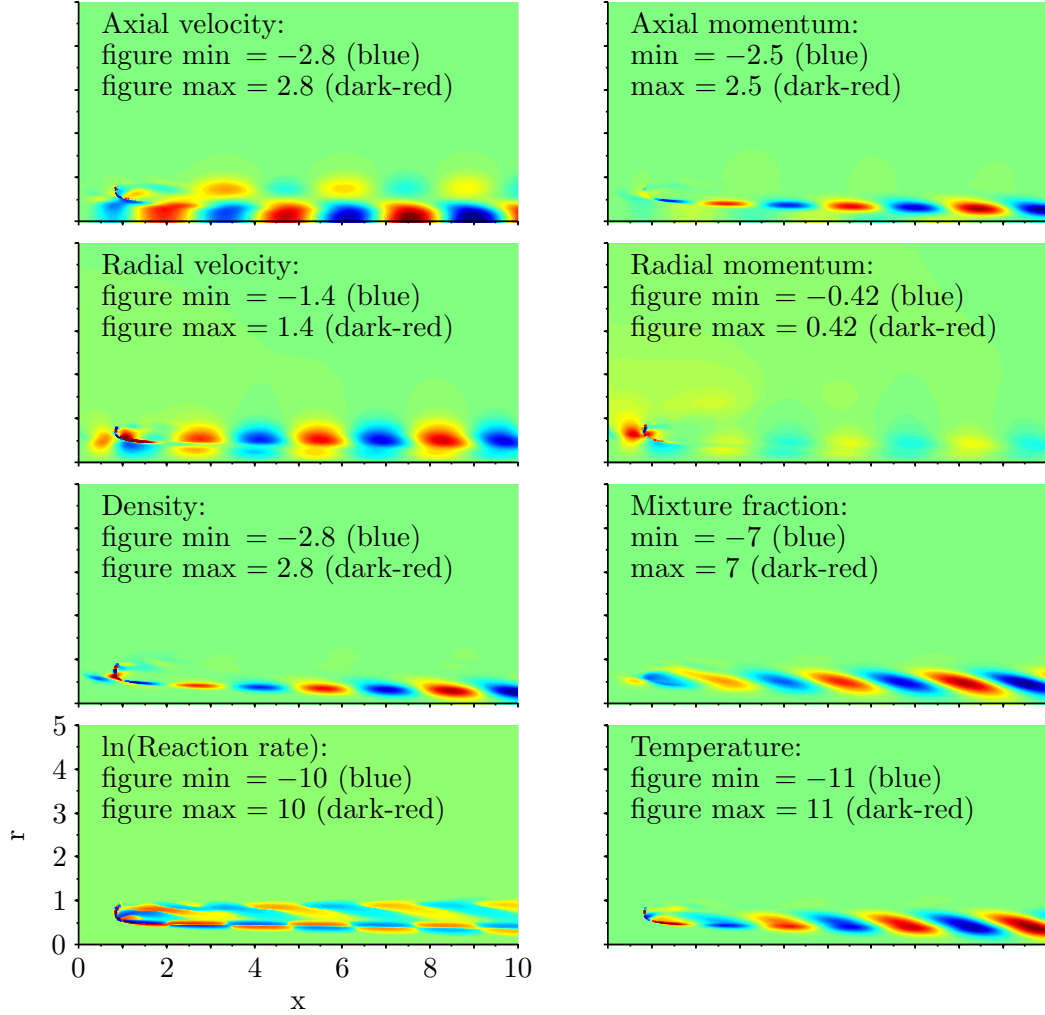
Figure 3.2: Real part of the non-dimensional reacting most-unstable direct global mode. The ln(reaction rate) subfigure shows the natural logarithm of the right hand side of (3.6d). The subfigure contains separate plots for the positive and negative parts of the reaction rate with one superimposed onto the other. For the positive parts, ln(reaction rate) + 7 is plotted for values between 0 and 10. For the negative parts, $-\ln(-(\text{reaction rate})) - 7$ is potted for values between -10 and 0. The subfigure is therefore centred on zero (green), which corresponds to a reaction rate with magnitude less than $\exp(-7)$.

mode shape is most dominant in the pre-mixing zone between the inlet and the flame base (figure 3.3). The overlays of the momentum and mixture fraction fields in figure 3.4 are dominant in the pre-mixing zone. This implies that the adjoint mode structures for these fields are small in the flame and grow rapidly in the pre-mixing zone and/or that the direct mode structures have a significant component in the pre-mixing zone despite the observed dominance in the flame.

The overlay of the temperature field, however, is dominant in the flame. This implies that the direct mode structure is small in the pre-mixing zone and grows rapidly in the flame, (which can be seen in figure 3.2 when compared to other fields) and/or that the adjoint mode structure has a significant component in the flame despite the observed dominance in the pre-mixing zone. This is likely to be due to the large amount of heat release and sudden temperature rise in the flame.

The temperature itself does not directly affect the hydrodynamic instability. The effect of the temperature on the hydrodynamic instability occurs through the effect of temperature on the density. The exact form of the temperature field is therefore of minimal interest when investigating the nature of the hydrodynamic instability. Figure 3.2 shows that while the temperature field has relatively minimal presence in the pre-mixing zone, the density field has a structure of comparable magnitude to the rest of
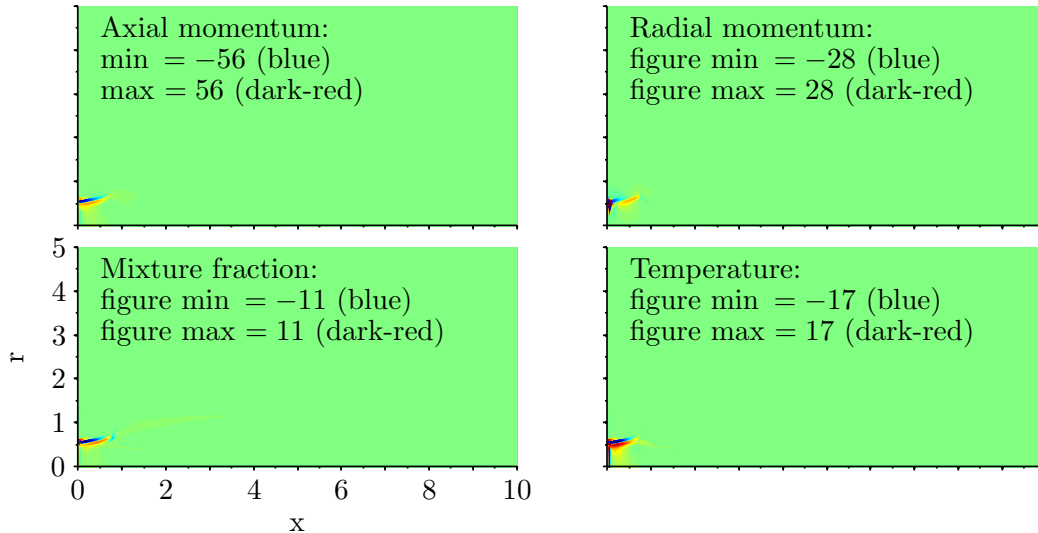
Figure 3.3: Real part of the non-dimensional reacting most-unstable discrete-adjoint global mode (volume distribution corrected).
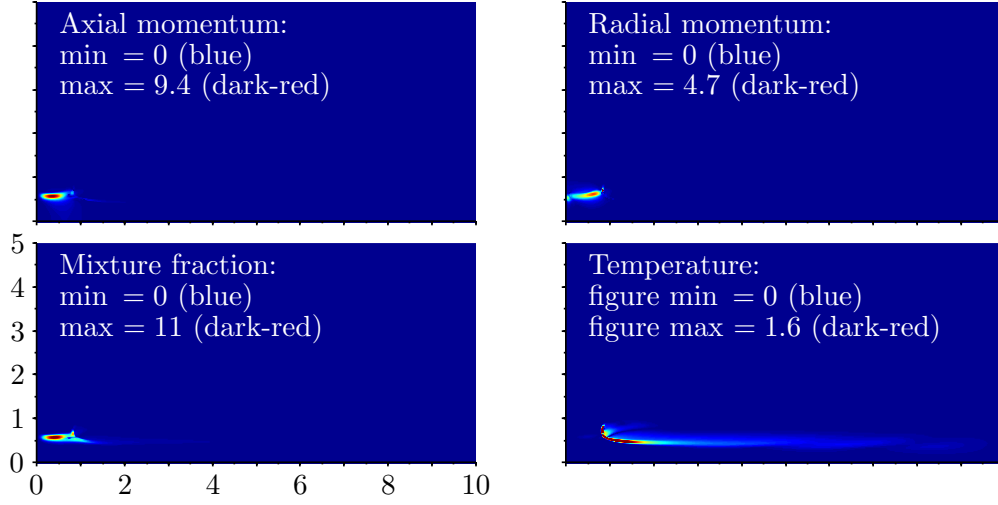
Figure 3.4: Absolute value of the non-dimensional reacting most-unstable discrete-adjoint global mode multiplied by the most-unstable direct global mode at every grid point (volume distribution corrected).

the mode.

By varying the initial condition, other steady converged solutions were found. Moving the spark upstream to $x = 0.9$ and $r = \pm 0.5$ resulted in a steady converged solution with liftoff height $h_l = 0.794$, whereas using a converged solution for $Da = 5 \times 10^5$ as the initial condition resulted in a steady converged solution with $h_l = 1.92$. The former of these two solutions is a steady and stable solution, with the most-unstable eigenvalue $\sigma = -0.0155 + \mathrm{i}\,0.226$, whereas the latter is a steady but unstable solution, with the most-unstable eigenvalue $\sigma = 0.180 + \mathrm{i}\,1.345$. The corresponding Strouhal numbers are $St = 0.036$ and $St = 0.213$ respectively. The linear stability properties of these base flows support the finding by Nichols & Schmid (2008) that if the flame base moves sufficiently far upstream, the global instability will be suppressed.

When the steady but unstable solution ($h_l = 1.92$) is used as an initial condition for an unsteady nonlinear time evolution, the flow eventually converges to the $h_l = 0.858$ steady solution. The fact that different steady solutions exist needs some further investigation, but for the present work it is not too important and provides some different cases to investigate further how heat release can affect the underlying hydrodynamic instability.

The base flows with $h_l = 0.794$ and $h_l = 1.92$ are qualitatively similar to the one shown in figure 3.1 for $h_l = 0.858$. For the case with $h_l = 1.92$ the spatial component developing in the pre-mixing zone is more pronounced and is shown for the axial velocity and density fields in figure 3.5. The adjoint mode structure and direct-adjoint overlay structure are qualitatively similar throughout the domain for all three modes, with the structures in the pre-mixing zone stretched to fill the different zone lengths.

The axial-momentum field of the discrete-adjoint mode for the $h_l = 1.92$ case is given in figure 3.6. The longer pre-mixing zone means that the adjoint mode shape is affected less by the flame. Figure 3.6 compares favourably with the axial-momentum field of the non-reacting continuous-adjoint mode in figure 2.5. The higher resolution used for the reacting simulations has significantly reduced the nonphysical behaviour that plagued the non-reacting discrete-adjoint mode in figure 2.4.
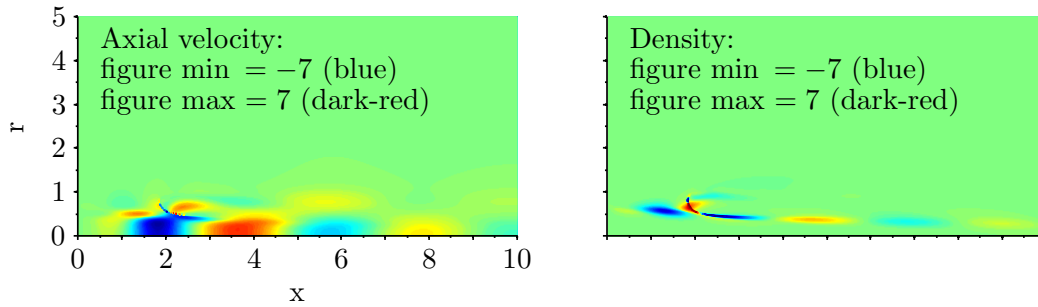
Figure 3.5: Real part of the axial velocity and density most-unstable direct global mode fields for the flame with liftoff height of 1.92.
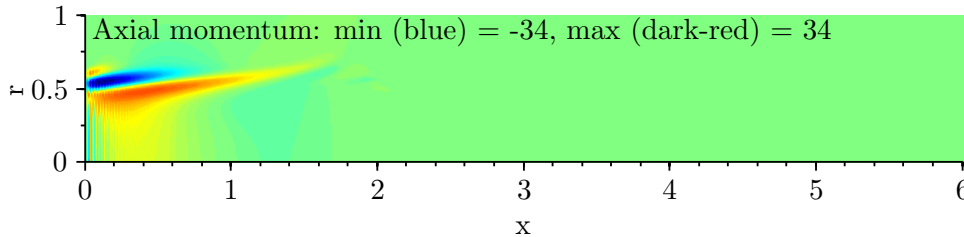
Figure 3.6: Real part of the axial-momentum most-unstable discrete-adjoint global mode field for the flame with liftoff height of 1.92 (volume distribution corrected).

3.7   Conclusions

The work contained in this chapter successfully calculates adjoint global modes for a reacting shear flow. The reacting adjoint equations and reacting discrete-adjoint numerical scheme follow closely that of the non-reacting case. Only minor changes were needed therefore to the non-reacting code. The form of the linear equations is again important for the derivation of the adjoint equations and some careful rearrangement is required to ensure that the linear and adjoint equation sets are of similar form.

The choice of configuration near to the first bifurcation point of the lifted flame yielded linear results that are close to the nonlinear results of Nichols & Schmid (2008). The eigenvalue of the most unstable mode suggests that the flow is marginally stable and gives a Strouhal number within 10% of the nonlinear Strouhal number observed by Nichols & Schmid.

The most-unstable direct global mode is dominant in the flame region, whereas the adjoint global mode is dominant in the pre-mixing zone. A superposition of the two modes is dominant in the pre-mixing zone. These qualitative assessments, together with the observation by Nichols & Schmid that as the flame base moves upstream the global instability is suppressed, suggest that the spatial component of the direct mode developing in the pre-mixing zone is driving the spatial component in the flame, and that the pre-mixing zone is therefore the most sensitive region of the flow. The most sensitive region of a flow is derived quantitatively in the next chapter.

Two alternative steady solutions were found with differing liftoff heights. The steady but unstable alternative solution highlighted the role of the pre-mixing zone in the global instability by showing greater direct-mode structure in the pre-mixing zone. The greater pre-mixing zone length suggests the flame interferes with the underlying non-reacting hydrodynamic instability less than for the marginally stable case. This is supported by comparing the adjoint mode structure, which bears greater similarity to the non-reacting case when the pre-mixing zone is larger.

CHAPTER 4

Sensitivity analysis

4.1 The physical meaning of adjoint global modes

The non-reacting and reacting linearized equations can be expressed in the same operational form of

$$\frac{\partial \boldsymbol{q}}{\partial t} - \mathrm{L}\boldsymbol{q} = \boldsymbol{s}, \tag{4.1}$$

where L is the linear operator and $\boldsymbol{s}$ is a vector introducing source terms to the right hand side of the linear equations. In the reacting case, the linearized term describing the heat release due to reaction has been moved to the left hand side of the linearized reacting energy equation (3.6d) and forms part of the linear operator L. For the non-reacting and reacting cases, $\boldsymbol{q}$ and $\boldsymbol{s}$ take the following forms

$$
\text{Non-reacting:} \quad \boldsymbol{q} = \left[\begin{array}{c} \boldsymbol{m}' \\ T' \end{array} \right], \quad \boldsymbol{s} = \left[\begin{array}{c} \boldsymbol{f}' \\ \varphi'/\bar{\rho} \end{array} \right],
$$

$$
\text{Reacting:} \quad \boldsymbol{q} = \left[\begin{array}{c} \boldsymbol{m}' \\ T' \\ Z' \end{array} \right], \quad \boldsymbol{s} = \left[\begin{array}{c} \boldsymbol{f}' \\ \varphi'/\bar{\rho} \\ 0 \end{array} \right],
\tag{4.2}
$$

where $\boldsymbol{f}'$ is the linearized, non-dimensional external applied force per unit volume and φ' is the linearized, non-dimensional rate of heat addition per unit volume. For the following analysis, $\boldsymbol{f}'$ and φ' are considered as open-loop source terms, i.e. they do not have any dependence on the state vector $\boldsymbol{q}$. The acoustic forcing used in Juniper *et al.* (2009) and Schmid *et al.* (2010) are examples of open-loop forcing. Acoustic forcing can

be modelled by a body force in the low-Mach-number equations in a similar way to the reduced order model of acoustic forcing used by Moeck *et al.* (2009) in a finite-difference zero-Mach-number solver for a Rijke tube.

The solution of the homogeneous problem can be divided into two parts: the discrete eigenmodes and the continuous spectrum (Drazin & Reid, 1981; Huerre & Monkewitz, 1985; Hill, 1995). Including a particular solution, due to the source term on the right hand side (Schmid, 2007), the full time dependent solution of (4.1) can be written as

$$\boldsymbol{q}\left(x,r,t\right) = \boldsymbol{q}_s\left(x,r,t\right) + \boldsymbol{q}_d\left(x,r,t\right) + \boldsymbol{q}_{cs}\left(x,r,t\right), \tag{4.3}$$

$$\boldsymbol{q}\left(x,r,0\right) = \boldsymbol{q}_0\left(x,r\right), \tag{4.4}$$

where $\boldsymbol{q}_s$, $\boldsymbol{q}_d$ and $\boldsymbol{q}_{cs}$ are the components of $\boldsymbol{q}$ arising from the source term, discrete eigenmodes and the continuous spectrum respectively and $\boldsymbol{q}_0$ is the initial condition. The source term $\boldsymbol{s}$ and, consequently, $\boldsymbol{q}_s$ are assumed to be be harmonic and take the forms

$$\boldsymbol{s}\left(x,r,t\right) = \hat{\boldsymbol{s}}\left(x,r\right)\exp(\sigma_s t), \tag{4.5}$$

$$\boldsymbol{q}_s\left(x,r,t\right) = \hat{\boldsymbol{q}}_s\left(x,r\right)\exp(\sigma_s t), \tag{4.6}$$

where σ_s is complex and describes the growth/decay and the frequency of the source term.

Writing $\boldsymbol{q}_d\left(x,r,t\right)$ as a summation of all N discrete eigenmodes with coefficients β_j, (4.3) becomes

$$\boldsymbol{q}\left(x,r,t\right) = \hat{\boldsymbol{q}}_s\left(x,r\right)\exp(\sigma_s t) + \sum_{j=1}^{N}\beta_j\hat{\boldsymbol{q}}_j\left(x,r\right)\exp(\sigma_j t) + \boldsymbol{q}_{cs}\left(x,r,t\right), \tag{4.7}$$

with each eigenmode, j, satisfying

$$\sigma_j\hat{\boldsymbol{q}}_j - \mathrm{L}\hat{\boldsymbol{q}}_j = 0. \tag{4.8}$$

Assuming that the discrete eigenmodes and continuous spectrum cover the whole of the solution space, it is possible to project the spatial terms $\hat{\boldsymbol{q}}_s$ and $\boldsymbol{q}_0$, which vary in space but not in time, onto them:

$$\hat{\boldsymbol{q}}_s = \sum_{j=1}^{N} \alpha_j \hat{\boldsymbol{q}}_j + \hat{\boldsymbol{q}}_{s\_cs}, \tag{4.9}$$

$$\boldsymbol{q}_0 = \sum_{j=1}^{N} \zeta_j \hat{\boldsymbol{q}}_j + \hat{\boldsymbol{q}}_{0\_cs}, \tag{4.10}$$

where $\hat{\boldsymbol{q}}_{s\_cs}$ and $\hat{\boldsymbol{q}}_{0\_cs}$ are the projections of the source term and initial conditions respectively onto the continuous spectrum. The coefficients α_j can be found by first substituting (4.6) and (4.5) into (4.1) and cancelling out the exponential terms:

$$\sigma_s \hat{\boldsymbol{q}}_s - \mathrm{L}\hat{\boldsymbol{q}}_s = \hat{\boldsymbol{s}}. \tag{4.11}$$

To proceed further it is necessary to define the inner product,

$$\langle \boldsymbol{q}_1, \boldsymbol{q}_2 \rangle = \frac{1}{V} \int_V \boldsymbol{q}_1^H \boldsymbol{q}_2 \; dV, \tag{4.12}$$

where $\boldsymbol{q}_1^H$ is the conjugate transpose of $\boldsymbol{q}_1$. Using the inner product, (4.11) is premultiplied by the adjoint mode $\hat{\boldsymbol{q}}_k^+$, corresponding to the discrete eigenmode k, to give

$$\langle \hat{\boldsymbol{q}}_k^+, \sigma_s \hat{\boldsymbol{q}}_s \rangle - \langle \hat{\boldsymbol{q}}_k^+, \mathrm{L}\hat{\boldsymbol{q}}_s \rangle = \langle \hat{\boldsymbol{q}}_k^+, \hat{\boldsymbol{s}} \rangle . \tag{4.13}$$

Using the analyses of Salwen & Grosch (1981) and Hill (1995), the bi-orthogonality of the discrete and continuum mode solutions implies

$$\langle \hat{\boldsymbol{q}}_k^+, \hat{\boldsymbol{q}}_{j\neq k} \rangle = \langle \hat{\boldsymbol{q}}_k^+, \hat{\boldsymbol{q}}_{s\_cs} \rangle = 0. \tag{4.14}$$

Substituting (4.9) and (4.8) into (4.13) and using (4.14) gives

$$\langle \hat{\boldsymbol{q}}_k^+, \sigma_s \alpha_k \hat{\boldsymbol{q}}_k \rangle - \langle \hat{\boldsymbol{q}}_k^+, \sigma_k \alpha_k \hat{\boldsymbol{q}}_k \rangle = \langle \hat{\boldsymbol{q}}_k^+, \hat{\boldsymbol{s}} \rangle . \tag{4.15}$$

$$\Rightarrow \alpha_k = \frac{1}{(\sigma_s - \sigma_k)} \frac{\langle \hat{\boldsymbol{q}}_k^+, \hat{\boldsymbol{s}} \rangle}{\langle \hat{\boldsymbol{q}}_k^+, \hat{\boldsymbol{q}}_k \rangle}. \tag{4.16}$$

The coefficients ζ_j can be found by first premultiplying (4.10) by the adjoint mode $\hat{\boldsymbol{q}}_k^+$. Then, using the bi-orthogonality condition (4.14), (4.10) can be rearranged to give

$$\zeta_k = \frac{\langle \hat{\boldsymbol{q}}_k^+, \hat{\boldsymbol{q}}_0 \rangle}{\langle \hat{\boldsymbol{q}}_k^+, \hat{\boldsymbol{q}}_k \rangle}. \tag{4.17}$$

Applying the initial condition at $t = 0$ to (4.7) and then substituting in (4.9) and (4.10) gives

$$\beta_j = \zeta_j - \alpha_j = \frac{\langle \hat{\boldsymbol{q}}_j^+, \hat{\boldsymbol{q}}_0 \rangle}{\langle \hat{\boldsymbol{q}}_j^+, \hat{\boldsymbol{q}}_j \rangle} - \frac{1}{(\sigma_s - \sigma_j)} \frac{\langle \hat{\boldsymbol{q}}_j^+, \hat{\boldsymbol{s}} \rangle}{\langle \hat{\boldsymbol{q}}_j^+, \hat{\boldsymbol{q}}_j \rangle}. \tag{4.18}$$

Substituting (4.9), (4.17) and (4.18) into (4.7) gives

$$
\boldsymbol{q}\left(x,r,t\right) = \sum_{j=1}^{N} \left\langle \hat{\boldsymbol{q}}_{j}^{+}, \hat{\boldsymbol{q}}_{0}\exp(\sigma_{j}t) + \hat{\boldsymbol{s}}\frac{(\exp(\sigma_{s}t) - \exp(\sigma_{j}t))}{(\sigma_{s} - \sigma_{j})} \right\rangle \frac{\hat{\boldsymbol{q}}_{j}\left(x,r\right)}{\langle \hat{\boldsymbol{q}}_{j}^{+}, \hat{\boldsymbol{q}}_{j}\rangle}
$$

$$
+ \hat{\boldsymbol{q}}_{s\_cs}\exp(\sigma_{s}t) + \boldsymbol{q}_{cs}. \quad (4.19)
$$

Equation (4.19) can provide useful insights into the effects of $\hat{\boldsymbol{q}}_{0}$, $\hat{\boldsymbol{s}}$ and σ_{s} on the time evolution of the state vector and also into the role the adjoint global modes play in quantifying these effects.

The source term is usually of fixed amplitude, which corresponds to $\mathrm{Re}(\sigma_{s}) = 0$. For a globally unstable flow, the eigenvalue of the most-unstable mode, σ_{1}, has a positive real component, which implies $\mathrm{Re}(\sigma_{1}) > \mathrm{Re}(\sigma_{s})$. Under these conditions, in the limit $t \to \infty$, (4.19) reduces to

$$
\boldsymbol{q}\left(x,r,t\right) = \left\langle \hat{\boldsymbol{q}}_{1}^{+}, \hat{\boldsymbol{q}}_{0} + \frac{\hat{\boldsymbol{s}}}{(\sigma_{1} - \sigma_{s})} \right\rangle \frac{\hat{\boldsymbol{q}}_{1}\left(x,r\right)}{\langle \hat{\boldsymbol{q}}_{1}^{+}, \hat{\boldsymbol{q}}_{1}\rangle}\exp(\sigma_{1}t). \quad (4.20)
$$

Neglecting nonlinear effects for the moment, equation (4.20) shows that, in the long time limit, the flow takes the form of the most-unstable direct global mode, $\hat{\boldsymbol{q}}_{1}$, growing exponentially according to $\mathrm{Re}(\sigma_{1})$ with a frequency of $2\pi\,\mathrm{Im}(\sigma_{1})$. The flow behaves therefore as an oscillator (Huerre & Monkewitz, 1990). The amplitude of the global mode at a particular time depends on $\left\langle \hat{\boldsymbol{q}}_{1}^{+}, \hat{\boldsymbol{q}}_{0} + \hat{\boldsymbol{s}}/\left(\sigma_{1} - \sigma_{s}\right) \right\rangle$. When $\hat{\boldsymbol{q}}_{1}^{+}$ and $(\hat{\boldsymbol{q}}_{0} + \hat{\boldsymbol{s}}/\left(\sigma_{1} - \sigma_{s}\right))$ are linearly dependent, the amplitude is at a maximum for a given initial energy, source amplitude and source frequency. The sensitivity of the global-mode amplitude to changes in the spatial distribution of the source term or initial conditions is therefore $\hat{\boldsymbol{q}}_{1}^{+}$.

Comparing the form of $\hat{\boldsymbol{q}}_{1}^{+}$ to the form of $\hat{\boldsymbol{s}}$ implies that the adjoint momentum is the sensitivity to external force and the adjoint temperature is the sensitivity to a heat source. With some extra algebraic manipulation, the analysis above can be extended to include a linearized, non-dimensional, rate of mass addition per unit volume, $\hat{\varrho}$, which results in $\langle \hat{\boldsymbol{q}}_{k}^{+}, \hat{\boldsymbol{s}}\rangle$ being replaced with $\langle \hat{\boldsymbol{q}}_{k}^{+}, \hat{\boldsymbol{s}}\rangle + \left\langle \left(\hat{p}_{k}^{+}/\bar{\rho}\right), \hat{\varrho}\right\rangle$ in equations (4.13), (4.16) and (4.18). The factor of $1/\bar{\rho}$ appears due to the way p^{+} was formed in the previous chapter. The adjoint pressure divided by the base density is therefore the sensitivity to mass injection.

It is also possible to introduce a new term to the right hand side of (4.13) that would allow the calculation of the sensitivity to boundary perturbations. A boundary condition, $\hat{\boldsymbol{q}}|_b = \hat{\boldsymbol{q}}_w$ (where $|_b$ denotes the part of $\hat{\boldsymbol{q}}$ located on the boundary and $\hat{\boldsymbol{q}}_w$ is the desired boundary value), can be made to be part of the linear operator by including it in the system of linearized equations. This extra equation is then multiplied by a new adjoint variable, $\hat{\boldsymbol{q}}_w^+$ say, inside a boundary surface integral. This results in the surface integral $\int_s \hat{\boldsymbol{q}}_w^{+H} \hat{\boldsymbol{q}}|_b\, ds$ being added to the boundary terms in (2.51), which allows $\hat{\boldsymbol{q}}_w^+$ to be calculated. We also get $\langle \hat{\boldsymbol{q}}_k^+, \hat{\boldsymbol{s}} \rangle$ being replaced with $\langle \hat{\boldsymbol{q}}_k^+, \hat{\boldsymbol{s}} \rangle + \int_s \hat{\boldsymbol{q}}_{wk}^{+H} \hat{\boldsymbol{q}}_w\, ds$ in equations (4.13), (4.16) and (4.18), which implies that the sensitivity to boundary perturbations is $\hat{\boldsymbol{q}}_w^+$. Due to the direct and adjoint perturbation boundary conditions in this work being homogeneous Dirichlet or the boundary values being assumed to be zero, boundary perturbations can not occur and the sensitivity to boundary perturbations is therefore zero.

For a globally stable flow, $\text{Re}(\sigma_1) < 0$ and therefore $\text{Re}(\sigma_1) < \text{Re}(\sigma_s)$. In the long time limit (4.19) reduces to

$$\boldsymbol{q}(x,r,t) = \sum_{j=1}^{N} \left\langle \hat{\boldsymbol{q}}_j^+, \frac{\hat{\boldsymbol{s}}}{(\sigma_s - \sigma_j)} \right\rangle \frac{\hat{\boldsymbol{q}}_j(x,r)}{\langle \hat{\boldsymbol{q}}_j^+, \hat{\boldsymbol{q}}_j \rangle} \exp(\sigma_s t) + \hat{\boldsymbol{q}}_{s\_cs} \exp(\sigma_s t). \qquad (4.21)$$

Equation (4.21) implies that a global mode will develop at the the source frequency σ_s, which is now an important factor in determining the form of the flow. The flow behaves now as a spatial amplifier (Huerre & Monkewitz, 1990). If σ_s is close to an eigenvalue, σ_k for example, then provided $\hat{\boldsymbol{s}}/(\sigma_s - \sigma_k)$ is not orthogonal to $\hat{\boldsymbol{q}}_k^+$, there will be a strong component of $\hat{\boldsymbol{q}}_k$ in the flow. Provided σ_s is not near to the continuous spectrum, the contribution of $\hat{\boldsymbol{q}}_{s\_cs}$ will be small. For $\sigma_s \approx \sigma_k$, the amplitude of the mode at a particular time depends most significantly on $\langle \hat{\boldsymbol{q}}_k^+, \hat{\boldsymbol{s}}/(\sigma_k - \sigma_s) \rangle$. When $\hat{\boldsymbol{q}}_k^+$ and $(\hat{\boldsymbol{s}}/(\sigma_k - \sigma_s))$ are linearly dependent, the amplitude is at a maximum for a given source amplitude and frequency. The sensitivity of the amplitude to changes in the spatial distribution of the source term is now approximately $\hat{\boldsymbol{q}}_k^+$.

In the theoretical limit of $\sigma_s \to \sigma_k$ and $t \to \infty$, (4.19) reduces to

$$\boldsymbol{q}(x,r,t) = \langle \hat{\boldsymbol{q}}_k^+, \hat{\boldsymbol{s}} \rangle \frac{\hat{\boldsymbol{q}}_k(x,r)}{\langle \hat{\boldsymbol{q}}_k^+, \hat{\boldsymbol{q}}_k \rangle} t \exp(\sigma_k t). \qquad (4.22)$$

The sensitivity of the modal amplitude to changes in the spatial distribution of the source term is now precisely $\hat{\boldsymbol{q}}_k^+$.

Equations (4.20) and (4.21) support the conclusion by Chomaz (2005) that, in a flow acting as an amplifier, the exponential decay of initial perturbations causes the flow to respond to harmonic source terms, whereas in a flow acting as an oscillator the exponential growth of initial perturbations overshadows the response to harmonic source terms. As well as the exponential growth of the initial perturbations, equation (4.20) shows that, for an oscillator-type flow, the structure of the source terms at $t = 0$ (from (4.5) $\boldsymbol{s}\,(x, r, 0) = \hat{\boldsymbol{s}}\,(x, r)$) also gets amplified exponentially. In some cases, if the source is switched on early enough, this may drown the contribution from the initial conditions.

4.1.1   Relation to previous results

For both the non-reacting and reacting flows considered in chapters 2 and 3, the largest components of the most-unstable adjoint global mode are located near the inlet and near to the shear layer. For an amplifier, this region is the region of maximum sensitivity of the global mode amplitude to the spatial distribution of the source term. For an oscillator, it is the region of maximum sensitivity of the global mode amplitude to the spatial distribution of the initial conditions and initial source term structure. For the lifted flame, the spatial structure of the adjoint global mode has low amplitude in the flame region and grows rapidly in the pre-mixing zone, which suggests that the direct global mode amplitude is relatively insensitive to external open-loop forcing and/or heating applied locally in the flame region.

The time-asymptotic analysis above is only valid in the time window (if it exists) from the onset of domination by the leading exponential term in (4.19) until the nonlinear effects become significant. Chomaz (2005) points out that for a highly non-normal linear global evolution operator, linear global mode theory is a poor indicator of fully nonlinear behaviour. With increasingly parallel flows, the direct and adjoint eigenmode separation increases due to the difference in sign of the corresponding advection terms, and this increases the amount of non-normality.

The increase in non-normality is associated with the direct global modes becoming less orthogonal to one another, which implies that the corresponding adjoint modes become less orthogonal to one another as well. The vectors in each direct-adjoint global mode pair become therefore more orthogonal to one another. This means that the inner product $\langle \hat{\boldsymbol{q}}_k^+, \hat{\boldsymbol{q}}_k \rangle$ becomes smaller as non-normality increases, which increases

the sensitivity.

For the most-unstable global modes calculated in the previous chapters, $\langle \hat{\boldsymbol{q}}^+, \hat{\boldsymbol{q}} \rangle$ is $\sim 4 \times 10^{-6}$ for the non-reacting case, ~ 0.003 for the $h_l = 0.858$ reacting case and ~ 0.013 for the $h_l = 1.92$ reacting case. The values for the reacting cases are much larger than for the non-reacting case because of the highly non-parallel region at the flame base, which reduces the separation between the adjoint and direct modes in the pre-mixing zone. If just the pre-mixing zone is considered then $\langle \hat{\boldsymbol{q}}^+, \hat{\boldsymbol{q}} \rangle$ is ~ 0.02 for $h_l = 0.858$ and ~ 0.04 for $h_l = 1.92$, which suggests that a significant amount of the non-normality is due to the long and weakly non-parallel flame region.

Moderate non-normality means that, in the vicinity of a bifurcation point, the nonlinear saturation amplitude is less sensitive to changes in the bifurcation parameters and a weakly nonlinear approach involving a Landau equation for the global mode amplitude is valid (Chomaz, 2005). If the assumptions of the weakly nonlinear approach are met, the theory shows that the physical interpretation of the adjoint global modes given above is valid in the nonlinear regime. Giannetti & Luchini (2007) point out that, for a cylinder wake, linear theory is unable to predict the real vortex-shedding frequency in the unstable regime far from the stable-unstable bifurcation point at $Re \approx 47$. As non-normality increases the flow needs to be closer to the bifurcation point in order to extend the interpretation of the adjoint modes to the fully nonlinear regime.

Extending the non-reacting results to the fully nonlinear regime is unlikely to give a good comparison because of the high non-normality. For the reacting cases, however, the non-normality is much less. The $h_l = 0.858$ case is also close to the bifurcation point, which suggests that the $h_l = 0.858$ results have greater validity in the fully-nonlinear regime. Comparing the Strouhal numbers calculated from the linear eigenvalues to the nonlinear Strouhal numbers observed by Nichols & Schmid (2008) gives approximately a 25% discrepancy for the non-reacting case and approximately a 10% discrepancy in the reacting $h_l = 0.858$ case.

4.2 Structural Sensitivity

Structural sensitivity refers to the sensitivity of an eigenvalue to changes in the governing linear operator. These changes can be due to changes in the governing parameters, such as Re or Pr, due to changes in the base flow fields, or due to changes in a feedback mechanism if one exists. A feedback mechanism is fundamentally different to the

open-loop source terms discussed in the previous section. In a feedback mechanism, a feedback operator acts on the state vector and the mechanism depends therefore on the state vector itself. Examples include drag from small cylinders or lift from small aerofoils placed in the flow or sensor-actuator arrangements used in flow control applications.

If a feedback mechanism exists as a source term in the governing equations, the feedback operator forms part of the linear governing operator. The following analysis for a structural perturbation in the linear operator L, is therefore equally valid for a structural perturbation in a feedback operator as well.

To find the structural sensitivity of the eigenvalue, σ, a similar analysis to that of Giannetti & Luchini (2007) is performed. It is first necessary to introduce a small perturbation to the linear operator $L \rightarrow L + \varepsilon \delta L$ and consider the limit as $\varepsilon \rightarrow 0$. A perturbed linear operator results in a perturbed eigenvalue as well as perturbed direct and adjoint eigenmodes: $\sigma \rightarrow \sigma + \varepsilon \delta \sigma$, $\hat{\boldsymbol{q}} \rightarrow \hat{\boldsymbol{q}} + \varepsilon \delta \hat{\boldsymbol{q}}$ and $\hat{\boldsymbol{q}}^+ \rightarrow \hat{\boldsymbol{q}}^+ + \varepsilon \delta \hat{\boldsymbol{q}}^+$. Substituting these perturbed quantities into equation (2.8) gives

$$
\left\langle (\hat{\boldsymbol{q}}^+ + \varepsilon \delta \hat{\boldsymbol{q}}^+), (\sigma + \varepsilon \delta \sigma)(\hat{\boldsymbol{q}} + \varepsilon \delta \hat{\boldsymbol{q}}) \right\rangle - \left\langle (\hat{\boldsymbol{q}}^+ + \varepsilon \delta \hat{\boldsymbol{q}}^+), (L + \varepsilon \delta L)(\hat{\boldsymbol{q}} + \varepsilon \delta \hat{\boldsymbol{q}}) \right\rangle = 0.
$$

$$
\Rightarrow \langle \hat{\boldsymbol{q}}^+, \sigma \hat{\boldsymbol{q}} \rangle - \langle \hat{\boldsymbol{q}}^+, L\hat{\boldsymbol{q}} \rangle + \langle \varepsilon \delta \hat{\boldsymbol{q}}^+, \sigma \hat{\boldsymbol{q}} \rangle - \langle \varepsilon \delta \hat{\boldsymbol{q}}^+, L\hat{\boldsymbol{q}} \rangle \ldots
$$

$$
+ \langle \hat{\boldsymbol{q}}^+, \sigma \, \varepsilon \delta \hat{\boldsymbol{q}} \rangle - \langle \hat{\boldsymbol{q}}^+, L(\varepsilon \delta \hat{\boldsymbol{q}}) \rangle + \langle \hat{\boldsymbol{q}}^+, \varepsilon \delta \sigma \hat{\boldsymbol{q}} \rangle - \langle \hat{\boldsymbol{q}}^+, \varepsilon \delta L \hat{\boldsymbol{q}} \rangle + O(\varepsilon^2) = 0.
$$

$$
\Rightarrow \langle \hat{\boldsymbol{q}}^+ + \varepsilon \delta \hat{\boldsymbol{q}}^+, \sigma \hat{\boldsymbol{q}} - L\hat{\boldsymbol{q}} \rangle + \langle \sigma^* \hat{\boldsymbol{q}}^+ - L^+ \hat{\boldsymbol{q}}^+, \varepsilon \delta \hat{\boldsymbol{q}} \rangle \ldots
$$

$$
\tag{4.23}
+ \varepsilon \delta \sigma \langle \hat{\boldsymbol{q}}^+, \hat{\boldsymbol{q}} \rangle - \varepsilon \langle \hat{\boldsymbol{q}}^+, \delta L \hat{\boldsymbol{q}} \rangle + O(\varepsilon^2) = 0.
$$

The first two terms in (4.23) can be eliminated using equations (2.6) and (2.11). This step highlights the requirement to pre-multiply by the adjoint global and not an arbitrary vector to obtain equation (2.8). Taking the limit $\varepsilon \rightarrow 0$, the remaining terms in (4.23) give

$$
\delta \sigma = \frac{\langle \hat{\boldsymbol{q}}^+, \delta L \hat{\boldsymbol{q}} \rangle}{\langle \hat{\boldsymbol{q}}^+, \hat{\boldsymbol{q}} \rangle}. \tag{4.24}
$$

The sensitivity of the eigenvalue σ to a structural perturbation in L is denoted $\nabla_L \sigma$ and is defined by

$$
\langle \nabla_L \sigma, \delta L \rangle \equiv \lim_{\varepsilon \rightarrow 0} \left(\frac{\sigma(L + \varepsilon \delta L) - \sigma(L)}{\varepsilon} \right). \tag{4.25}
$$

The right hand side in (4.25) describes the change in σ due to a change in L and is therefore equivalent to $\delta\sigma$ in (4.24). Combining (4.24) and (4.25) gives

$$\delta\sigma = \langle \nabla_{\mathrm{L}}\sigma, \delta\mathrm{L} \rangle, \tag{4.26}$$

$$\Rightarrow \langle \nabla_{\mathrm{L}}\sigma, \delta\mathrm{L} \rangle = \frac{\langle \hat{\boldsymbol{q}}^{+}, \delta\mathrm{L}\hat{\boldsymbol{q}} \rangle}{\langle \hat{\boldsymbol{q}}^{+}, \hat{\boldsymbol{q}} \rangle}. \tag{4.27}$$

Depending on the application, the structural perturbation may be expressed in a form that allows the direct mode $\hat{\boldsymbol{q}}$ to be shifted to the left hand side of the inner product in (4.27). The sensitivity $\nabla_{\mathrm{L}}\sigma$ can then be found on its own without the need for the inner product.

4.3 Sensitivity to force feedback

It can be assumed that the self sustained oscillations of global modes arise from a feedback mechanism that is inherent in the governing operator. Giannetti & Luchini (2007) suggest the momentum of the fluid feeds back as a force and drives itself creating the unstable global mode. To analyze the effect of this feedback mechanism on the eigenvalue of the global mode it is necessary to artificially perturb it. In practice this could be done by inserting an object in the flow that disrupts the feedback loop or using a sensor-actuator feedback device. Following Giannetti & Luchini, we can perturb this feedback mechanism by assuming the feedback force has the form $\boldsymbol{GUm}$, where G is the feedback gain and $\boldsymbol{U}$ is, for the axisymmetric case, a 2×2 unitary matrix that represents a unitary transformation of the momentum vector, such as a rotation and/or phase shift, where $\|\boldsymbol{Um}\| = \|\boldsymbol{m}\|$. It is assumed that the feedback force vector at a particular point is dependent only on the momentum vector at that point. The matrix $\boldsymbol{U}$ and scalar G can vary throughout the domain and the force and momentum vectors do not have to be linearly dependent.

To analyse the sensitivity of the eigenvalue it is necessary to substitute $\boldsymbol{GUm}$ for $\boldsymbol{f}$ in (4.2) and set the rate of heat addition, φ, to zero. Defining a feedback operator F_f, which represents the force feedback as an operator acting on the state vector $\boldsymbol{q}$, (4.1) can be written as

$$\frac{\partial \boldsymbol{q}}{\partial t} - (\mathrm{L} + \mathrm{F}_f)\boldsymbol{q} = 0. \tag{4.28}$$

Equation (4.28) is a homogeneous equation that has a different set of eigenvalues and eigenvectors to (4.1) corresponding to the new operator $(\mathrm{L}+\mathrm{F}_f)$. We are interested in non trivial solutions of (4.28) of the form

$$\boldsymbol{q}(x, r, t) = \hat{\boldsymbol{q}}(x, r) \exp(\sigma t). \tag{4.29}$$

Substituting (4.29) into (4.28), we can write the new system of equations in the form

$$\sigma \hat{\boldsymbol{q}} - (\mathrm{L} + \mathrm{F}_f)\hat{\boldsymbol{q}} = 0. \tag{4.30}$$

It is now possible to find the structural sensitivity of the eigenvalue, σ, to a change in the feedback operator, $\delta \mathrm{F}_f$. Substituting F_f for L in (4.27) gives

$$\langle \nabla_{\mathrm{F}_f} \sigma, \delta \mathrm{F}_f \rangle = \frac{\langle \hat{\boldsymbol{q}}^+, \delta \mathrm{F}_f \hat{\boldsymbol{q}} \rangle}{\langle \hat{\boldsymbol{q}}^+, \hat{\boldsymbol{q}} \rangle} = \frac{\langle \hat{\boldsymbol{m}}^+, \delta(G\boldsymbol{U})\hat{\boldsymbol{m}} \rangle}{\langle \hat{\boldsymbol{q}}^+, \hat{\boldsymbol{q}} \rangle}. \tag{4.31}$$

The inner product $\langle \hat{\boldsymbol{q}}^+, \delta \mathrm{F}_f \hat{\boldsymbol{q}} \rangle$ has been reduced to $\langle \hat{\boldsymbol{m}}^+, \delta(G\boldsymbol{U})\hat{\boldsymbol{m}} \rangle$ by first expanding $\langle \hat{\boldsymbol{q}}^+, \delta \mathrm{F}_f \hat{\boldsymbol{q}} \rangle$ to a summation of separate inner products (one for each field contained in the state vector) and then noting that, for all fields except momentum, the separate inner products are zero.

For the present study, we are interested in the case where the feedback operator is perturbed from zero. It can be assumed therefore that $\boldsymbol{U}$ is fixed and that the gain is perturbed from $G = 0$ to $G = \delta G$. This implies that $\delta(G\boldsymbol{U}) = \boldsymbol{U}\delta G$. This also implies that $\langle \nabla_{\mathrm{F}_f} \sigma, \delta \mathrm{F}_f \rangle = \langle \nabla_G \sigma, \delta G \rangle$. From (4.31) this leads to

$$
\begin{aligned}
\langle \nabla_G \sigma, \delta G \rangle &= \frac{\langle \hat{\boldsymbol{m}}^+, \boldsymbol{U}\hat{\boldsymbol{m}}\delta G \rangle}{\langle \hat{\boldsymbol{q}}^+, \hat{\boldsymbol{q}} \rangle}, \\
\Rightarrow \langle \nabla_G \sigma, \delta G \rangle &= \frac{\langle (\boldsymbol{U}\hat{\boldsymbol{m}})^H \hat{\boldsymbol{m}}^+, \delta G \rangle}{\langle \hat{\boldsymbol{q}}^+, \hat{\boldsymbol{q}} \rangle}, \\
\Rightarrow \nabla_G \sigma &= \frac{(\boldsymbol{U}\hat{\boldsymbol{m}})^H \hat{\boldsymbol{m}}^+}{\langle \hat{\boldsymbol{q}}^+, \hat{\boldsymbol{q}} \rangle}.
\end{aligned} \tag{4.32}
$$

Noting that $\nabla_G \sigma$ is a scalar field and using (4.26) and (4.12), the change in the eigenvalue due to a change in the feedback gain is

$$\delta \sigma = \frac{1}{V} \int_V (\nabla_G \sigma)^* \delta G \, dV. \tag{4.33}$$

The real and imaginary parts of $(\nabla_G \sigma)^*$ correspond to the sensitivities of the real and imaginary parts of σ to changes in G. For instance, if G is increased in a region where the real and imaginary parts of $\nabla_G \sigma$ are positive, then the modal growth rate will increase and, if the imaginary part of σ is positive, the modal frequency will decrease because of the conjugation.

The inner product $\langle \hat{\boldsymbol{q}}^+, \hat{\boldsymbol{q}} \rangle$ is complex and has therefore a significant effect on the real and imaginary parts of $\nabla_G \sigma$. The arbitrary phase shifts introduced in the calculation of the complex values of the direct and adjoint global modes are cancelled out in (4.32) between the momentum fields in the numerator and the inner product in the denominator.

Equation (4.32) shows that, for a large sensitivity to the force-momentum coupling at a particular point, it is necessary to have both a large value of the direct momentum, to give a large feedback force, and a large value of the adjoint momentum to give a good sensitivity to that force. Equation (4.32) also shows, however, that the linear dependence between the feedback force vector ($\boldsymbol{U}\hat{\boldsymbol{m}}$) and the adjoint momentum vector $\hat{\boldsymbol{m}}^+$ affects the sensitivity significantly, which emphasizes the importance of the unitary transform represented by $\boldsymbol{U}$.

If the coupling is constrained so that the feedback force is in the same direction as the direct momentum vector and has no phase shift, then $\boldsymbol{U}$ becomes the identity matrix. The resulting inner product, $\hat{\boldsymbol{m}}^H \hat{\boldsymbol{m}}^+$, effectively projects the direct momentum vector (feedback force vector) onto the adjoint momentum vector (force sensitivity vector). If the direct and adjoint momentum vectors are linearly dependent there is a strong feedback, but if they are orthogonal there is no feedback.

Treating $(\boldsymbol{U}\hat{\boldsymbol{m}})^H \hat{\boldsymbol{m}}^+$ as an inner product, the Cauchy–Schwarz inequality gives

$$|(\boldsymbol{U}\hat{\boldsymbol{m}})^H \hat{\boldsymbol{m}}^+| \leqslant \|\boldsymbol{U}\hat{\boldsymbol{m}}\|\|\hat{\boldsymbol{m}}^+\|,$$
$$\Rightarrow |(\boldsymbol{U}\hat{\boldsymbol{m}})^H \hat{\boldsymbol{m}}^+| \leqslant \|\hat{\boldsymbol{m}}\|\|\hat{\boldsymbol{m}}^+\|, \tag{4.34}$$

where $|\ |$ is the absolute value of a complex number and $\|\ \|$ is the l^2-norm of the momentum vector at each point in space. Using (4.34), the maximum absolute value of the sensitivity of σ to changes in G at each spatial location is

$$|\nabla_G \sigma|_{max} = \frac{\|\hat{\boldsymbol{m}}\|\|\hat{\boldsymbol{m}}^+\|}{|\langle \hat{\boldsymbol{q}}^+, \hat{\boldsymbol{q}} \rangle|}. \tag{4.35}$$

Equation (4.35) is equivalent to equation (8.11) in Giannetti & Luchini (2007). The spatial location where $|\nabla_G \sigma|_{max}$ is greatest is denoted by Giannetti & Luchini (2007) as the instability core. For a globally oscillating flow, the instability core is the region where the eigenvalue of the global mode is most sensitive to perturbations in the inherent feedback mechanism driving the instability. The instability core plays an important role in the origin and development of a global instability, which implies that any mechanism that disrupts the perturbation dynamics and the base flow in the vicinity of the instability core will have a large effect on the instability properties of the global mode. This could partly explain the success achieved by Giannetti & Luchini (2007) using the instability core to predict theoretically the experimental findings of Strykowski & Sreenivasan (1990), despite not directly taking into account modifications to the base flow caused by the presence of the control cylinder.

4.3.1 Results

The most-unstable global modes from chapters 2 and 3 are used to calculate $\nabla_G \sigma$ (with $\boldsymbol{U} = \boldsymbol{I}$) and $|\nabla_G \sigma|_{max}$ for the hot jet (using the direct and continuous-adjoint global modes) and for the lifted flames with liftoff heights $h_l = 0.858$ and $h_l = 1.92$ (using the direct and volume-distribution-corrected discrete-adjoint global modes). These sensitivity maps are shown in figures 4.1, 4.2 and 4.3. A convention used throughout this work is that if the minimum/maximum values of the figures are stated as 'min'/'max', they also refer to the minimum/maximum values of the data, whereas if they are stated as 'figure min'/'figure max', they refer to the figure values only and differ from the actual minimum/maximum values of the data. In the modal figures, the minimum/maximum values have been set using the value with larger magnitude so that the figure is centred on zero.

The instability core is located in the region where $|\nabla_G \sigma|_{max}$ is largest. $|\nabla_G \sigma|_{max}$ is the sensitivity when $\boldsymbol{U}$ is such that the feedback force is aligned with and in phase with the adjoint momentum vector, which is the direction and phase of greatest sensitivity. The instability core is located at approximately $x = 7$, $r = 0.5$, for the non-reacting case, at approximately $x = 0.35$, $r = 0.58$, for the $h_l = 0.858$ case, and at approximately $x = 0.9$, $r = 0.58$, for the $h_l = 1.92$ case. This suggests that the feedback mechanism driving the global mode is near the middle of the pre-mixing zone for the lifted flames, but at a significant distance (7 jet diameters) downstream of the inlet for the hot jet.
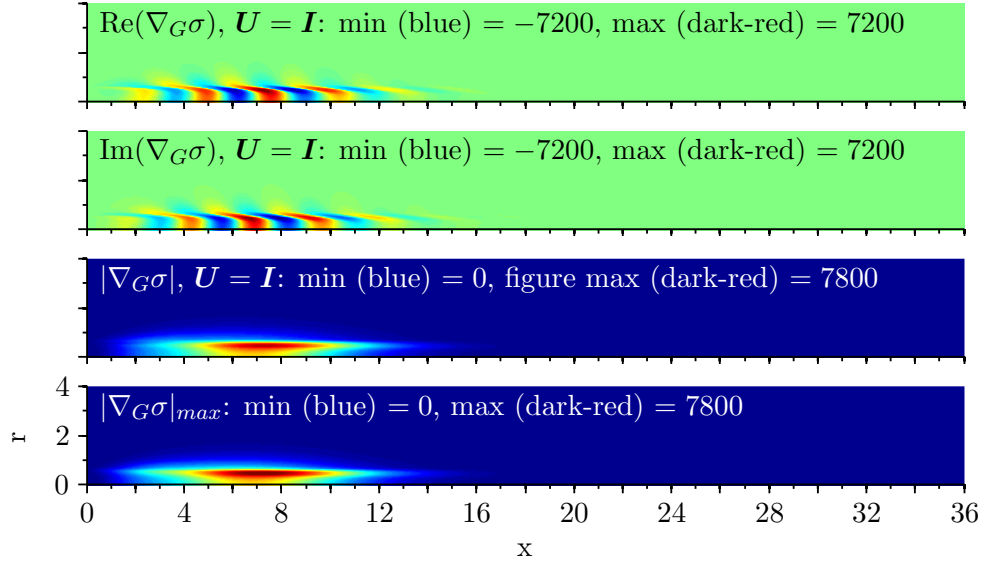
Figure 4.1: Sensitivity ($\nabla_G\sigma$) of the most-unstable eigenvalue (σ) to an increase the force feedback gain (G) for the hot jet. For $U = I$ the feedback force is aligned with and in phase with the direct momentum vector. The real and imaginary parts of $\nabla_G\sigma$ correspond to the sensitivity of the growth rate and frequency of the global mode.

The flame has therefore shifted the centre of the feedback mechanism upstream.

For $U = I$ the feedback force is aligned with and in phase with the direct momentum vector. $\nabla_G\sigma$ is the sensitivity of the eigenvalue σ to an increase in the feedback gain G, which is initially zero. $\mathrm{Re}(\nabla_G\sigma)$ is the sensitivity of the growth rate ($\mathrm{Re}(\sigma)$) of the global mode and $\mathrm{Im}(\nabla_G\sigma)$ is the sensitivity of the frequency ($\mathrm{Im}(\sigma)$) of the global mode.

Considering equation (4.33), figures 4.1, 4.2 and 4.3 can be interpreted in terms of the change in the growth rate and frequency of the global mode for a small localized increase in the feedback gain G. For instance, if a sensor-actuator, providing a gain such that $\int_V \delta G \, dV = 0.01$, is placed at $x = 7$, $r = 0.5$, in the hot jet (figure 4.1), (where $\mathrm{Re}(\nabla_G\sigma) = 6240$ and $\mathrm{Im}(\nabla_G\sigma) = -1220$) the growth rate ($\mathrm{Re}(\sigma)$) will increase by $\sim 82\%$ and the Strouhal number will increase by $\sim 0.6\%$.

The non-reacting real and imaginary parts of $\nabla_G\sigma$ (figure 4.1) alternate in the streamwise direction, whereas the reacting real and imaginary parts of $\nabla_G\sigma$ (figures 4.2 and 4.3) alternate in the spanwise direction. The absolute values of $\nabla_G\sigma$, however,
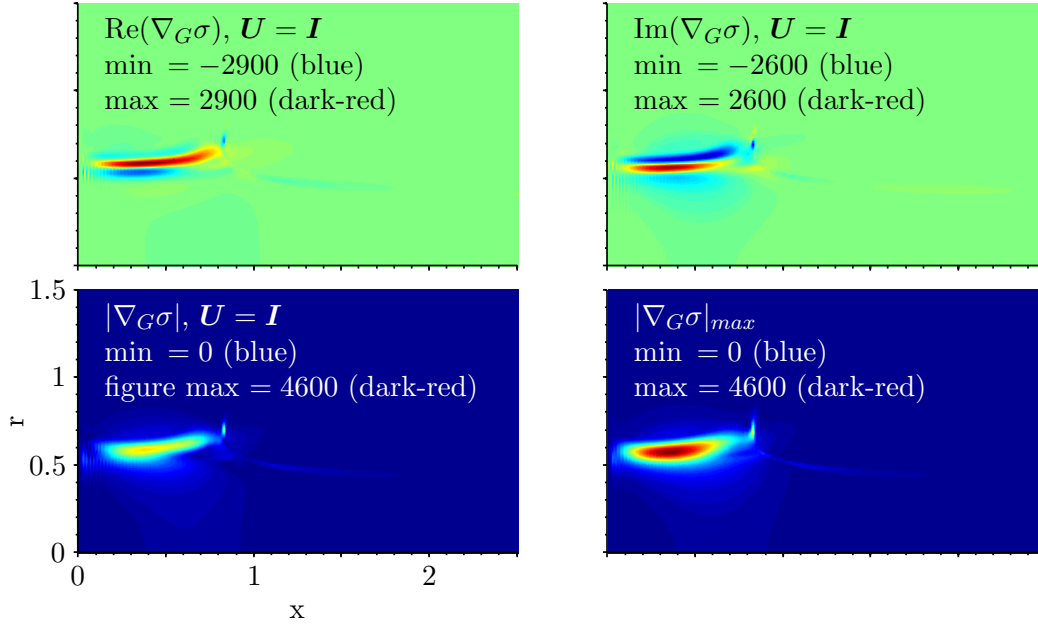
Figure 4.2: Sensitivity ($\nabla_G \sigma$) of the most-unstable eigenvalue (σ) to an increase the force feedback gain (G) for the flame with liftoff height of 0.858. For $\boldsymbol{U} = \boldsymbol{I}$ the feedback force is aligned with and in phase with the direct momentum vector. The real and imaginary parts of $\nabla_G \sigma$ correspond to the sensitivity of the growth rate and frequency of the global mode.

do not alternate. Moving a small sensor-actuator along the alternating regions would alternately enhance and suppress the growth rate of the global mode and alternately increase and decrease the frequency. The magnitude of the change in the eigenvalue σ, however, would vary slowly. The effect of a sensor-actuator on the stability properties of the flow depends significantly therefore on its precise location.

The similarity between $|\nabla_G \sigma|$ when $\boldsymbol{U} = \boldsymbol{I}$ and $|\nabla_G \sigma|_{max}$ in figure 4.1, suggests that the non-reacting direct and adjoint momentum vectors are almost linearly dependent at each point in space. The same maximum value has been used in both subfigures in order to make a direct comparison. The linear dependency is caused by the axial momentum amplitude being an order of magnitude larger than the radial momentum amplitude in the dominant region, which is shown in figure 2.7. The absolute value of $\nabla_G \sigma$ when $\boldsymbol{U} = \boldsymbol{I}$ for the flame with $h_l = 0.858$ is similar in shape to $|\nabla_G \sigma|_{max}$, but unlike the non-reacting case the amplitude is significantly less. For the flame with $h_l = 1.92$ the shape
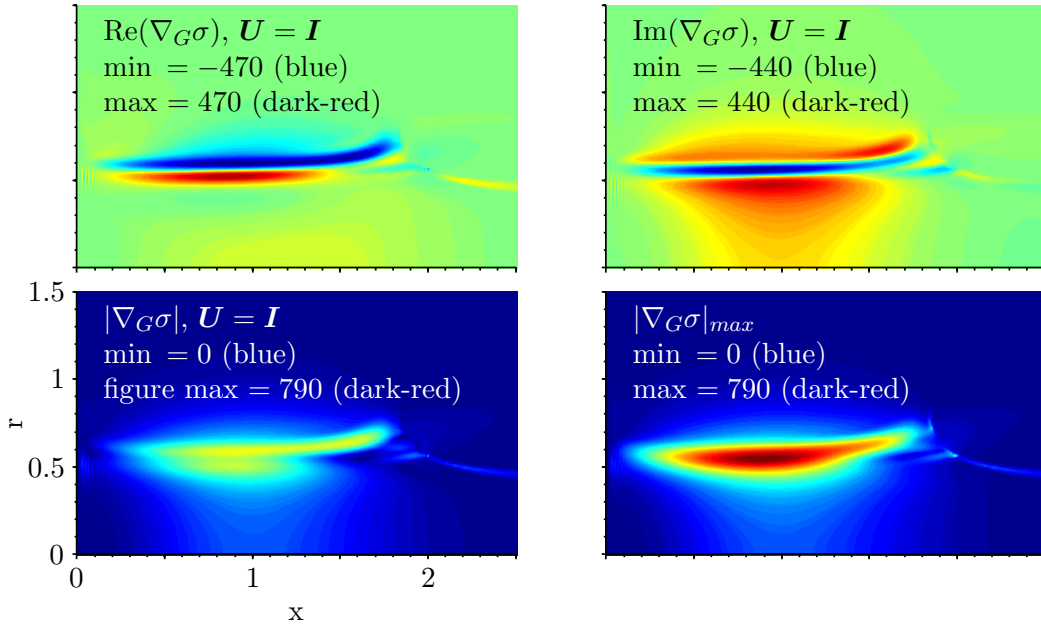
Figure 4.3: Sensitivity ($\nabla_G \sigma$) of the most-unstable eigenvalue (σ) to an increase the force feedback gain (G) for the flame with liftoff height 1.92. For $\boldsymbol{U} = \boldsymbol{I}$ the feedback force is aligned with and in phase with the direct momentum vector. The real and imaginary parts of $\nabla_G \sigma$ correspond to the sensitivity of the growth rate and frequency of the global mode.

as well as the amplitude differ. The direct and adjoint momentum vectors are more orthogonal for the reacting cases than for the non-reacting case, because the reacting axial momentum amplitude is smaller compared to the radial momentum amplitude in the dominant region ($|m_x|$ is approximately double $|m_r|$ for the $h_l = 0.858$ case, see figure 3.4). The force feedback from a small cylinder is aligned with the direct momentum vector. The hot jet is therefore likely to be more sensitive to this feedback force than the lifted flames because of the greater linear dependency of the direct and adjoint momentum vectors.

4.4 Sensitivity to heat and drag from a hot wire

In this section it is assumed that the rate of heat addition per unit volume φ and external force per unit volume $\boldsymbol{f}$ are due to a hot wire placed in the flow, that forms

an axisymmetric ring centred on the centre of the jet. The overall rate of heat addition $\widetilde{Q}$ in Watts (W) is given by the dimensional convection equation

$$\widetilde{Q} = \tilde{h}\widetilde{A}\left(\widetilde{T}_w - \widetilde{T}_l\right), \tag{4.36}$$

where $\widetilde{A}$ is the surface area of the wire in metres squared (m^2), $\widetilde{T}_w$ and $\widetilde{T}_l$ are the temperatures in Kelvin (K) of the wire and local fluid respectively and $\tilde{h}$ is the convective heat transfer coefficient (W m^{-2} K^{-1}). The dimensional rate of heat addition per unit volume of fluid, $\tilde{\varphi}$ (Wm^{-3}), is given by $\widetilde{Q}/\widetilde{L}_w\tilde{d}_j^2$, where $\widetilde{L}_w$ is the length of the wire (m) and $\tilde{d}_j$ is the diameter of the jet (m), which is the length scale used to non-dimensionalize the fluid equations. Noting that $\widetilde{A} = \pi \tilde{d}_w \widetilde{L}_w$, where $\tilde{d}_w$ is the diameter of the wire, and using the thermal conductivity of the fluid λ (W m^{-1} K^{-1}), jet temperature $\widetilde{T}_j$ (K), ambient temperature $\widetilde{T}_0$ (K) and jet diameter $\tilde{d}_j$ (m), (4.36) can be non-dimensionalised:

$$\frac{\tilde{d}_j^2 \tilde{\varphi}}{\lambda\left(\widetilde{T}_j - \widetilde{T}_0\right)} = \pi\left(\frac{\tilde{h}\tilde{d}_w}{\lambda}\right)\left(\frac{\left(\widetilde{T}_w - \widetilde{T}_0\right)}{\left(\widetilde{T}_j - \widetilde{T}_0\right)} - \frac{\left(\widetilde{T}_l - \widetilde{T}_0\right)}{\left(\widetilde{T}_j - \widetilde{T}_0\right)}\right), \tag{4.37}$$

$$\Rightarrow \varphi = \pi Nu\left(T_w - T_l\right), \tag{4.38}$$

where the non-dimensional rate of heat addition per unit volume of fluid φ is defined as $\tilde{d}_j^2\tilde{\varphi}/(\lambda(\widetilde{T}_j - \widetilde{T}_0))$, the Nusselt number Nu is defined as $\tilde{h}\tilde{d}_w/\lambda$, the non-dimensional wire temperature T_w is defined as $(\widetilde{T}_w - \widetilde{T}_0)/(\widetilde{T}_j - \widetilde{T}_0)$ and the non-dimensional local fluid temperature T_l is defined as $(\widetilde{T}_l - \widetilde{T}_0)/(\widetilde{T}_j - \widetilde{T}_0)$.

Assuming the Prandtl number of the fluid is constant, an empirical relationship between the Nusselt number Nu and local Reynolds number of the wire Re_w is given by

$$Nu = cRe_w^\eta, \tag{4.39}$$

$$\text{where } Re_w \equiv \frac{\tilde{\rho}_l\|\tilde{\boldsymbol{u}}_l\|\tilde{d}_w}{\mu}. \tag{4.40}$$

For a hot wire in cross flow, the empirical values c and η are typically in the ranges 0.9-1.0 and 0.30-0.36 respectively (White, 2008). The parameter μ is the dynamic viscosity of the fluid, $\tilde{\rho}_l$ is the density of the fluid at the location of the hot wire (kg m^{-3}) and $\|\tilde{\boldsymbol{u}}_l\|$ is the l^2-norm of the velocity vector at the location of the hot wire (m s^{-1}). Substituting (4.39) into (4.38) gives

$$\varphi = \pi c Re_w^\eta \left(T_w - T_l \right).$$
(4.41)

The Reynolds number of the wire is not a fixed quantity because it varies with the local density and velocity of the fluid. It is necessary to introduce the Reynolds number of the jet into (4.41):

$$\varphi = \pi c \left(\frac{\tilde{\rho}_l \|\tilde{\boldsymbol{u}}_l\| \tilde{d}_w}{\mu} \right)^\eta \left(\frac{\tilde{\rho}_j}{\tilde{\rho}_0} \frac{\mu}{\tilde{\rho}_j \tilde{u}_j \tilde{d}_j} \right)^\eta \left(S_1 Re \right)^\eta \left(T_w - T_l \right),$$
(4.42)

$$\varphi = \left(\pi c \left(S_1 Re \right)^\eta \right) \left(\frac{\tilde{d}_w}{\tilde{d}_j} \right)^\eta \left(\frac{\tilde{\rho}_l \|\tilde{\boldsymbol{u}}_l\|}{\tilde{\rho}_0 \tilde{u}_j} \right)^\eta \left(T_w - T_l \right),$$
(4.43)

$$\varphi = c_\varphi d_w^\eta \|\boldsymbol{m}_l\|^\eta \left(T_w - T_l \right),$$
(4.44)

where $\|\boldsymbol{m}_l\|$ is the l^2-norm of the non-dimensional momentum vector at the location of the hot wire, d_w is the diameter of the wire non-dimensionalized with the jet diameter and $c_\varphi = \pi c \left(S_1 Re \right)^\eta$. φ is currently a point source located at the position of the wire. Turning φ into a distributed source using the axisymmetric Dirac delta function at the position of the wire, $\delta^2(x_w, r_w)/(2\pi|r_w|)$, gives

$$\varphi(x,r) = c_\varphi d_w^\eta \|\boldsymbol{m}(x,r)\|^\eta \left(T_w - T(x,r) \right) \delta^2(x_w, r_w)/(2\pi|r_w|).$$
(4.45)

Noting that

$$\|\boldsymbol{m}\| \approx \|\bar{\boldsymbol{m}}\| + \frac{\boldsymbol{m}' \cdot \bar{\boldsymbol{m}}}{\|\bar{\boldsymbol{m}}\|},$$

for $\|\boldsymbol{m}'\| \ll \|\bar{\boldsymbol{m}}\|$, equation (4.45) can be linearized:

$$\bar{\varphi} = c_\varphi d_w^\eta \|\bar{\boldsymbol{m}}\|^\eta \left(T_w - \bar{T} \right) \delta^2(x_w, r_w)/(2\pi|r_w|),$$
(4.46)

$$\varphi' = c_\varphi d_w^\eta \|\bar{\boldsymbol{m}}\|^\eta \left(\left(T_w - \bar{T} \right) \eta \frac{\boldsymbol{m}' \cdot \bar{\boldsymbol{m}}}{\|\bar{\boldsymbol{m}}\|^2} - T' \right) \delta^2(x_w, r_w)/(2\pi|r_w|).$$
(4.47)

The drag force $\tilde{\boldsymbol{f}}$ (N) acting on the flow from the wire is given by

$$\tilde{\boldsymbol{f}} = -\frac{1}{2} \tilde{d}_w^2 C_D \tilde{\rho} \|\tilde{\boldsymbol{u}}_l\| \tilde{\boldsymbol{u}}_l,$$
(4.48)

where C_D is the Re_w dependent drag coefficient. For flow around a cylinder at low Reynolds numbers ($Re_w < 1$), C_D is proportional to Re_w^{-1} (for example see Munson *et al.*, 1998). Assuming the wire is thin compared to the jet implies that Re_w is

sufficiently small for C_D to be replaced with b/Re_w. Using this relation, (4.48) can be non-dimensionalized

$$\frac{\tilde{\boldsymbol{f}}}{\tilde{d}_j^2 \tilde{\rho}_0 \tilde{u}_j^2} = -\left(\frac{b}{2S_1 Re}\right)\left(\frac{\tilde{d}_w}{\tilde{d}_j}\right)\left(\frac{\tilde{\boldsymbol{u}}_l}{\tilde{u}_j}\right),$$

$$\Rightarrow \boldsymbol{f} = -c_f d_w \boldsymbol{u}_l, \tag{4.49}$$

where the non-dimensional drag force $\boldsymbol{f}$ is defined as $\tilde{\boldsymbol{f}}/(\tilde{d}_j^2 \tilde{\rho}_0 \tilde{u}_j^2)$, $c_f \equiv b/(2S_1 Re)$ is a positive constant, the non-dimensional wire diameter d_w is defined as $\tilde{d}_w/\tilde{d}_j$, and the non-dimensional local velocity $\boldsymbol{u}_l$ is defined as $\tilde{\boldsymbol{u}}_l/\tilde{u}_j$. Turning $\boldsymbol{f}$ from a point force to a distributed force gives

$$\boldsymbol{f}(x, r) = -c_f d_w \boldsymbol{u}(x, r)\, \delta^2(x_w, r_w)/(2\pi|r_w|). \tag{4.50}$$

Linearizing (4.50) gives

$$\bar{\boldsymbol{f}} = -c_f d_w \bar{\boldsymbol{u}}\, \delta^2(x_w, r_w)/(2\pi|r_w|), \tag{4.51}$$

$$\boldsymbol{f}' = -c_f d_w \boldsymbol{u}'\, \delta^2(x_w, r_w)/(2\pi|r_w|). \tag{4.52}$$

The present work derives and calculates the sensitivity to unsteady perturbative forcing. The theory for the sensitivity to steady forcing is given as an extension to this work in chapter 5.

Substituting (4.47) and (4.52) into (4.1) and defining a feedback operator F_w, which represents the action of (4.47) and (4.52) on the state vector $\boldsymbol{q}$, (4.1) can be written as

$$\frac{\partial \boldsymbol{q}}{\partial t} - (L + F_w)\boldsymbol{q} = 0. \tag{4.53}$$

Equation (4.53) is a homogeneous equation that has a different set of eigenvalues and eigenvectors to (4.1) corresponding to the new operator $(L+F_w)$. We are interested in non trivial solutions of (4.53) of the form

$$\boldsymbol{q}(x, r, t) = \hat{\boldsymbol{q}}(x, r)\exp(\sigma t). \tag{4.54}$$

Substituting (4.54) into (4.53), we can write the new system of equations in the form

$$\sigma \hat{\boldsymbol{q}} - (L + F_w)\hat{\boldsymbol{q}} = 0. \tag{4.55}$$

It is now possible to find the structural sensitivity of the eigenvalue, σ, to a change in the feedback operator, δF_w. Substituting F_w for L in (4.27) gives

$$\langle \nabla_{F_w} \sigma, \delta F_w \rangle = \frac{\langle \hat{\boldsymbol{q}}^+, \delta F_w \hat{\boldsymbol{q}} \rangle}{\langle \hat{\boldsymbol{q}}^+, \hat{\boldsymbol{q}} \rangle}. \tag{4.56}$$

For the present study, we are interested in the case where the feedback operator is perturbed from zero, which approximates the case where a hot wire is placed in an otherwise unperturbed flow. Two physical causes for the change in F_w are considered, one through a change in wire temperature, which implies $\langle \nabla_{F_w} \sigma, \delta F_w \rangle = \langle \nabla_{T_w} \sigma, \delta T_w \rangle$ and one through a change in wire diameter, which implies $\langle \nabla_{F_w} \sigma, \delta F_w \rangle = \langle \nabla_{d_w} \sigma, \delta d_w \rangle$. Considering first a change in wire temperature, the sensitivity of the eigenvalue is

$$\langle \nabla_{T_w} \sigma, \delta T_w \rangle = \frac{\left\langle \hat{T}^+, \bar{\rho}^{-1} c_\varphi d_w^\eta \|\bar{\boldsymbol{m}}\|^\eta \eta \frac{\hat{\boldsymbol{m}} \cdot \bar{\boldsymbol{m}}}{\|\bar{\boldsymbol{m}}\|^2} \delta^2(x_w, r_w)(2\pi|r_w|)^{-1} \delta T_w \right\rangle}{\langle \hat{\boldsymbol{q}}^+, \hat{\boldsymbol{q}} \rangle}, \tag{4.57}$$

$$\Rightarrow \nabla_{T_w} \sigma = \left(\frac{c_\varphi \eta d_w^\eta \|\bar{\boldsymbol{m}}\|^\eta}{\langle \hat{\boldsymbol{q}}^+, \hat{\boldsymbol{q}} \rangle} \right) \left(\frac{\hat{\boldsymbol{m}} \cdot \bar{\boldsymbol{m}}}{\bar{\rho} \|\bar{\boldsymbol{m}}\|^2} \frac{\delta^2(x_w, r_w)}{(2\pi|r_w|)} \right)^H \hat{T}^+, \tag{4.58}$$

$$\delta\sigma = \frac{1}{V} \int_V (\nabla_{T_w} \sigma)^* \delta T_w \, dV,$$

$$\Rightarrow \delta\sigma = \frac{1}{V} \left[\left(\frac{c_\varphi \eta d_w^\eta \|\bar{\boldsymbol{m}}_l\|^\eta}{\langle \hat{\boldsymbol{q}}^+, \hat{\boldsymbol{q}} \rangle} \right) \left(\frac{\hat{\boldsymbol{m}}_l \cdot \bar{\boldsymbol{m}}_l}{\bar{\rho}_l \|\bar{\boldsymbol{m}}_l\|^2} \right)^H \hat{T}_l^+ \right]^* \delta T_w, \tag{4.59}$$

where subscript l denotes the value of the field at the location of the hot wire. Real-valued scalar quantities, such as constants and norms, are not changed by the Hermitian operator and the operator has therefore been removed from this group. The extra $\bar{\rho}^{-1}$ has appeared in (4.57) due to the form of $\hat{s}$ in (4.2).

Using a similar method to consider a change in the wire diameter, the sensitivity of

the eigenvalue is

$$
\langle \nabla_{d_w}\sigma, \delta d_w \rangle = -\frac{\left\langle \hat{\boldsymbol{m}}^+, c_f \hat{\boldsymbol{u}}\, \delta^2(x_w, r_w)(2\pi|r_w|)^{-1}\delta d_w \right\rangle}{\langle \hat{\boldsymbol{q}}^+, \hat{\boldsymbol{q}} \rangle} \cdots
$$

$$
+ \frac{\left\langle \hat{T}^+, \bar{\rho}^{-1} c_\varphi \eta d_w^{\eta-1}\|\bar{\boldsymbol{m}}\|^\eta \left((T_w - \bar{T})\,\eta \frac{\hat{\boldsymbol{m}}\cdot\bar{\boldsymbol{m}}}{\|\bar{\boldsymbol{m}}\|^2} - \hat{T} \right)\delta^2(x_w, r_w)(2\pi|r_w|)^{-1}\delta d_w \right\rangle}{\langle \hat{\boldsymbol{q}}^+, \hat{\boldsymbol{q}} \rangle},
$$

$\Rightarrow$

$$
\nabla_{d_w}\sigma = \left[\left(\frac{c_\varphi \eta d_w^\eta \|\bar{\boldsymbol{m}}\|^\eta}{\langle \hat{\boldsymbol{q}}^+, \hat{\boldsymbol{q}} \rangle} \right) \frac{1}{d_w} \left(\left((T_w - \bar{T})\,\eta \frac{\hat{\boldsymbol{m}}\cdot\bar{\boldsymbol{m}}}{\|\bar{\boldsymbol{m}}\|^2} - \hat{T} \right) \frac{1}{\bar{\rho}} \frac{\delta^2(x_w, r_w)}{(2\pi|r_w|)} \right)^H \hat{T}^+ \cdots \right.
$$

$$
\left. - \left(\frac{c_f}{\langle \hat{\boldsymbol{q}}^+, \hat{\boldsymbol{q}} \rangle} \right) \left(\hat{\boldsymbol{u}}\, \frac{\delta^2(x_w, r_w)}{(2\pi|r_w|)} \right)^H \hat{\boldsymbol{m}}^+ \right],
$$

$$
(4.60)
$$

$$
\delta\sigma = \frac{1}{V}\int_V (\nabla_{d_w}\sigma)^* \delta d_w\, dV,
$$

$$
\Rightarrow \delta\sigma = \frac{1}{V}\left[\left(\frac{c_\varphi \eta d_w^\eta \|\bar{\boldsymbol{m}}_l\|^\eta}{\langle \hat{\boldsymbol{q}}^+, \hat{\boldsymbol{q}} \rangle} \right) \frac{1}{d_w} \left(\frac{(T_w - \bar{T}_l)\,\eta}{\bar{\rho}_l} \frac{\hat{\boldsymbol{m}}_l\cdot\bar{\boldsymbol{m}}_l}{\|\bar{\boldsymbol{m}}_l\|^2} - \frac{\hat{T}_l}{\bar{\rho}_l} \right)^H \hat{T}_l^+ \cdots \right.
$$

$$
\left. - \left(\frac{c_f}{\langle \hat{\boldsymbol{q}}^+, \hat{\boldsymbol{q}} \rangle} \right) \hat{\boldsymbol{u}}_l^H \hat{\boldsymbol{m}}_l^+ \right]^* \delta d_w.
$$

$$
(4.61)
$$

By comparing the pre-multipliers for the adjoint momentum and adjoint temperature in (4.61) it is possible to see which would have a greater effect on the eigenvalue when a small change in d_w occurs, the drag force or the heat addition. Equation (4.61) also shows that if the diameter of the wire is increased in a region where the real part of $\nabla_{d_w}\sigma$ is negative, the wire will suppress the instability.

4.4.1 Results

It is assumed that $\eta = 0.33$ and $c = 1.0$ (White, 2008), which gives $c_\varphi = 58.3$. To investigate the sensitivity of the eigenvalue to a change in wire temperature, the non-dimensional wire diameter, d_w, is set to 10^{-4}, implying the diameter of the wire is 10^4 times smaller than the diameter of the jet. For the flows concerned, the Reynolds number based on the jet is 1000, which implies that, if the wire is placed in the jet, $Re_w = 0.1$.

Using these values, the sensitivity of the most-unstable eigenvalue to an increase in hot wire temperature ($\nabla_{T_w}\sigma$) is calculated at each point in the domain (using the same

global modes that were used in section 4.3.1) and the resulting sensitivity maps for the non-reacting and reacting cases are shown in figures 4.4, 4.5 and 4.6. A convention used throughout this work is that if the minimum/maximum values of the figures are stated as 'min'/'max', they also refer to the minimum/maximum values of the data, whereas if they are stated as 'figure min'/'figure max', they refer to the figure values only and differ from the actual minimum/maximum values of the data. In the modal figures, the minimum/maximum values have been set using the value with larger magnitude so that the figure is centred on zero.
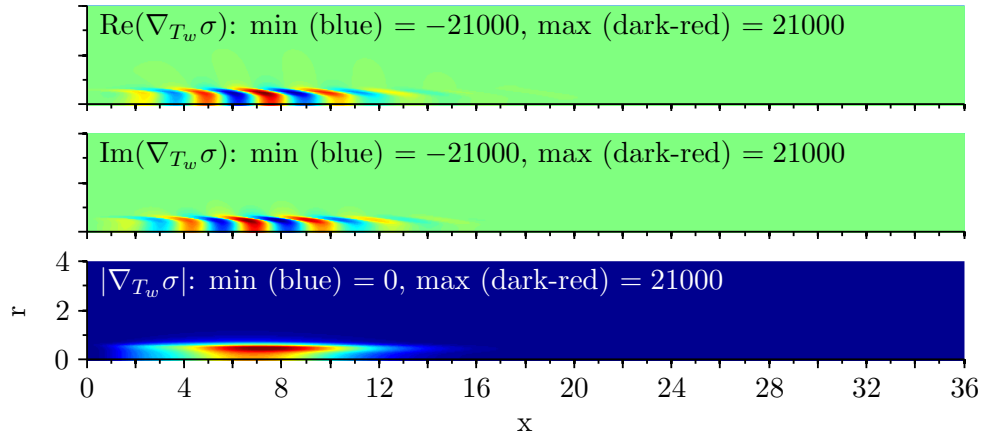
Figure 4.4: Sensitivity ($\nabla_{T_w}\sigma$) of the most-unstable eigenvalue (σ) to an increase in hot wire temperature (T_w) for the hot jet. The real and imaginary parts of $\nabla_{T_w}\sigma$ correspond to the sensitivity of the growth rate and frequency of the global mode.

From figure 9.21 in Munson *et al.* (1998), the parameter b in equation (4.4) for a cylinder in cross flow is estimated to be approximately 6, which implies $c_f = 4.3 \times 10^{-4}$. To investigate the sensitivity of the eigenvalue to a change in wire diameter, the non-dimensional wire temperature, T_w, is set to 0.5 and the resulting sensitivity maps are shown in figures 4.7, 4.8 and 4.9. c_f is approximately 5 orders of magnitude smaller than c_φ, which implies the sensitivity due to the drag of the wire is significantly lower than the sensitivity due to the heat release.

A cold wire placed in the flow can therefore be considered to have a negligible effect on the eigenvalue. $\nabla_{T_w}\sigma$ represents therefore the sensitivity to a change in temperature of an already-present cold wire. $\nabla_{d_w}\sigma$ on the other hand represents the sensitivity of placing an already-hot wire in an otherwise unperturbed flow. The real and imaginary
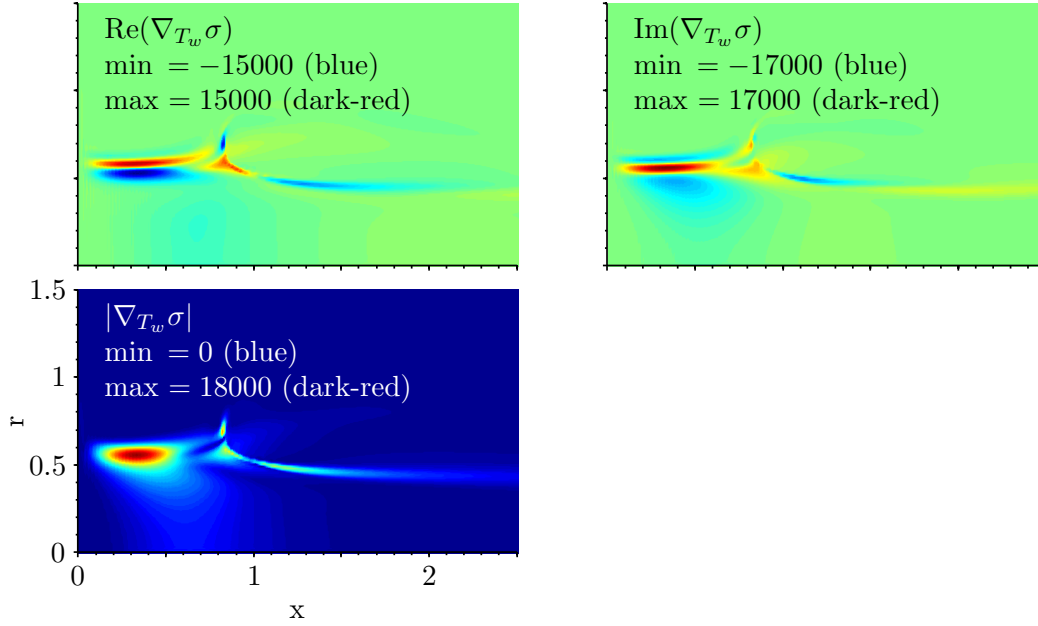
Figure 4.5: Sensitivity ($\nabla_{T_w}\sigma$) of the most-unstable eigenvalue (σ) to an increase in hot wire temperature (T_w) for the flame with liftoff height 0.858. The real and imaginary parts of $\nabla_{T_w}\sigma$ correspond to the sensitivity of the growth rate and frequency of the global mode.

parts of $\nabla_{T_w}\sigma$ and $\nabla_{d_w}\sigma$ correspond to the sensitivities of the real and imaginary parts of the eigenvalue σ. They correspond therefore to the sensitivities of the growth rate and frequency of the global mode. For instance, switching on a hot wire located in a positive (red) region of the real part of $\nabla_{T_w}\sigma$ in figures 4.4, 4.5 and 4.6 would increase the modal growth rate. Switching on a hot wire located in a positive (red) region of the imaginary part of $\nabla_{T_w}\sigma$, however, would decrease the modal frequency, because $\text{Im}(\sigma)$ is positive and $\delta\sigma$ depends on $(\nabla_{T_w}\sigma)^*$. For example, if a cold wire is located at $x = 0.3$, $r = 0.58$, in the flame with $h_l = 0.858$ (figure 4.5), (where $\text{Re}(\nabla_{T_w}\sigma) = 12700$ and $\text{Im}(\nabla_{T_w}\sigma) = 8820$) and is switched on to give a temperature rise of $\delta T_w = 0.01$, the growth rate ($\text{Re}(\sigma)$) will increase from -0.094 to $+0.067$ and the Strouhal number will decrease by $\sim 6\%$. The hot wire will therefore cause the stable flow to become globally unstable.

There is a large difference in the magnitudes of $\nabla_{T_w}\sigma$ and $\nabla_{d_w}\sigma$. This is because of the relative magnitudes of T_w and d_w. If percentage changes in T_w and d_w were to be
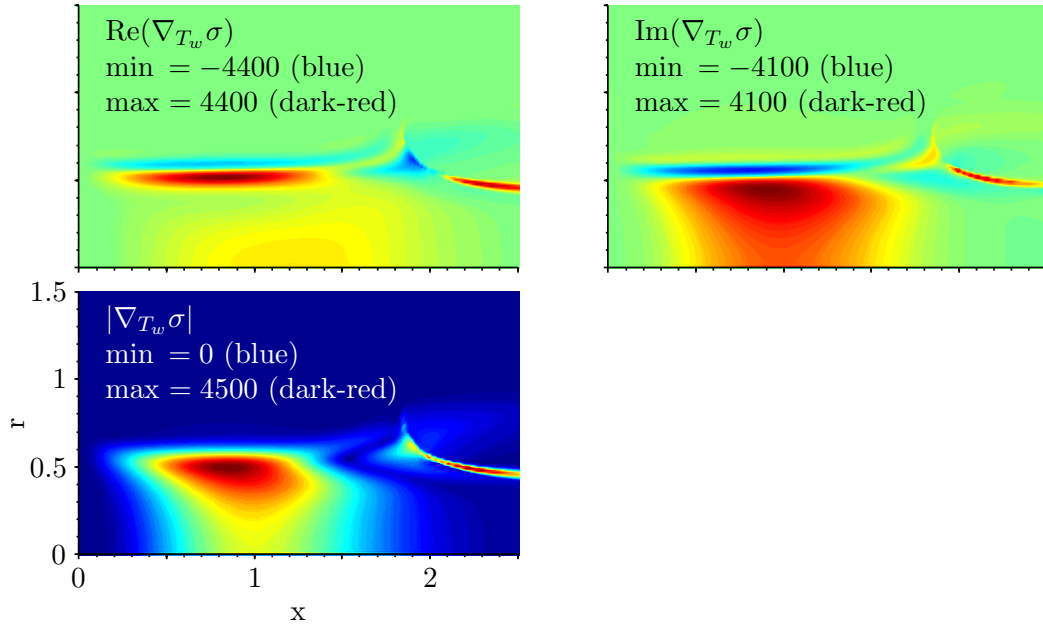
Figure 4.6: Sensitivity ($\nabla_{T_w}\sigma$) of the most-unstable eigenvalue (σ) to an increase in hot wire temperature (T_w) for the flame with liftoff height 1.92. The real and imaginary parts of $\nabla_{T_w}\sigma$ correspond to the sensitivity of the growth rate and frequency of the global mode.

considered instead of absolute changes, the magnitudes of the sensitivity maps would be of similar order.

For both reacting cases, the sensitivity to wire diameter is largest in the slim region near the inner surface of the flame (figures 4.8 and 4.9), whereas the sensitivity to the wire temperature is largest in the pre-mixing zone (figures 4.5 and 4.6). This is because $\nabla_{d_w}\sigma$ depends on the direct temperature field, whereas $\nabla_{T_w}\sigma$ does not depend on the direct temperature field, which explains the higher sensitivity to the wire diameter near the flame.

Re($\nabla_{d_w}\sigma$): min (blue) $= -1.6 \times 10^8$, max (dark-red) $= 1.6 \times 10^8$

Im($\nabla_{d_w}\sigma$): min (blue) $= -1.6 \times 10^8$, max (dark-red) $= 1.6 \times 10^8$

$|\nabla_{d_w}\sigma|$: min (blue) $= 0$, max (dark-red) $= 1.6 \times 10^8$
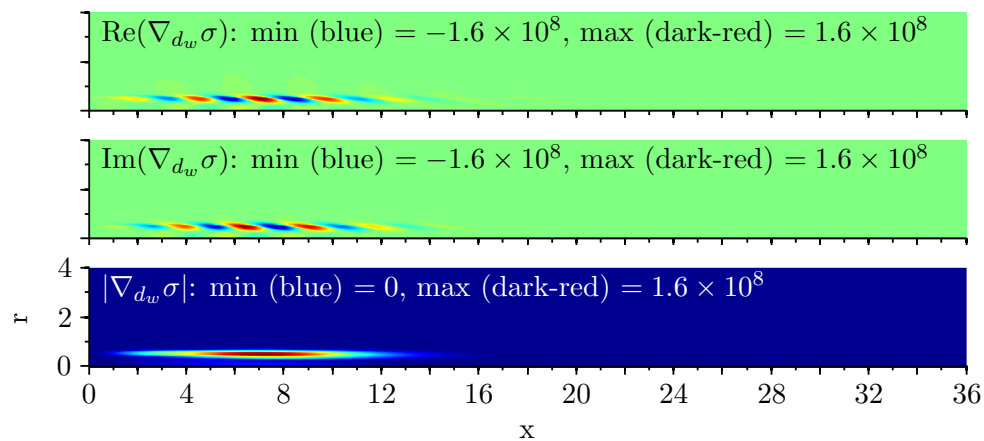
Figure 4.7: Sensitivity ($\nabla_{d_w}\sigma$) of the most-unstable eigenvalue (σ) to an increase in hot wire diameter (d_w) for the hot jet.

Re($\nabla_{d_w}\sigma$)
min $= -5.3 \times 10^7$ (blue)
max $= 5.3 \times 10^7$ (dark-red)

Im($\nabla_{d_w}\sigma$)
min $= -6 \times 10^7$ (blue)
max $= 6 \times 10^7$ (dark-red)

$|\nabla_{d_w}\sigma|$
min $= 0$ (blue)
max $= 6 \times 10^7$ (dark-red)
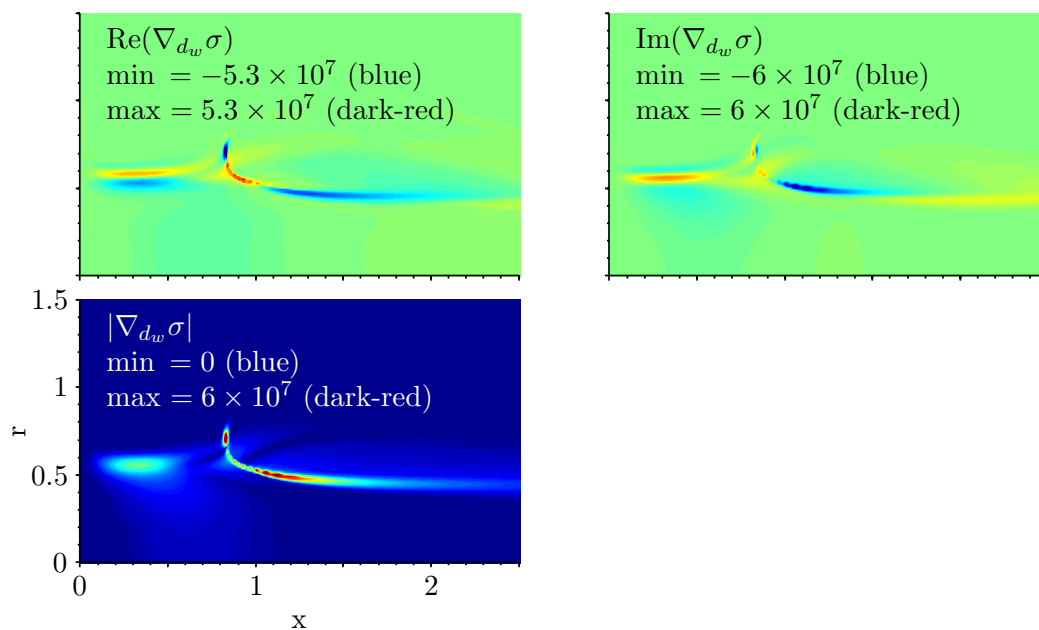
Figure 4.8: Sensitivity ($\nabla_{d_w}\sigma$) of the most-unstable eigenvalue (σ) to an increase in hot wire diameter (d_w) for the flame with liftoff height 0.858.
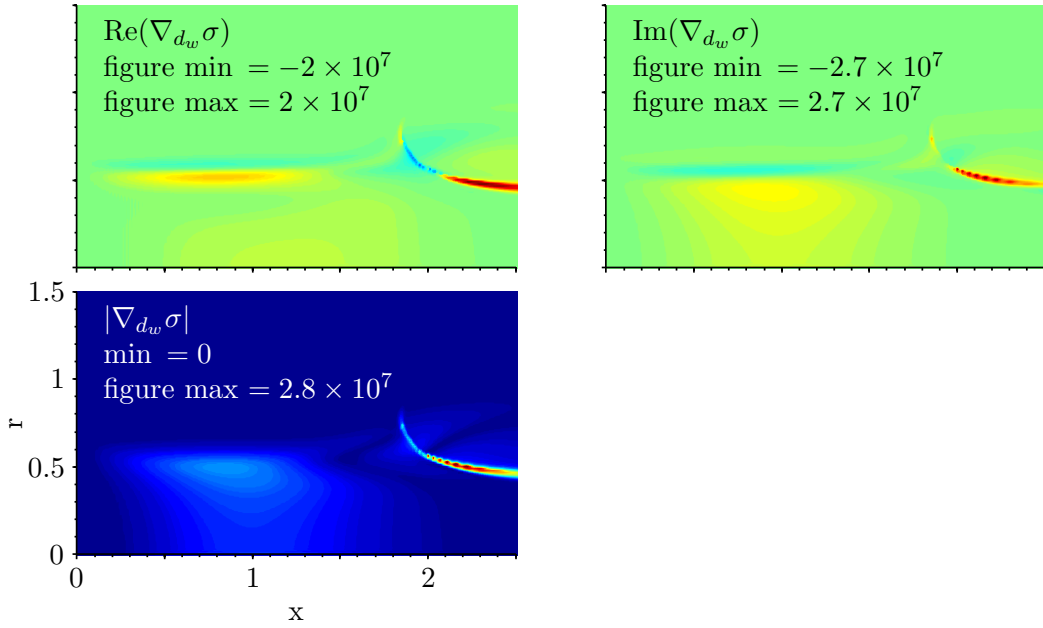
Figure 4.9: Sensitivity ($\nabla_{d_w}\sigma$) of the most-unstable eigenvalue (σ) to an increase in hot wire diameter (d_w) for the flame with liftoff height 1.92. Blue regions correspond to minimum values, dark-red regions correspond to maximum values.

4.5   Local analysis[1]

The base flows for the non-reacting and reacting (liftoff heights: $h_l = 0.858$, $h_l = 1.92$) cases are analysed with a local stability analysis (Huerre & Monkewitz, 1990). The radial profiles of the density and axial velocity at each discrete axial location are considered independently and are assumed to extend infinitely far up- and downstream. Axisymmetric perturbations are assumed and are made up from normal modes of the form $e^{\mathrm{i}(kx-\omega t)}$. These are substituted into the fully-compressible linearized Navier–Stokes equations with the Mach number set to 0.01, to solve for the perturbation in primitive variables (u_x, u_r, p, ρ, T) (Correia Da Costa, 2009).

At each axial location these equations are discretized on a grid with a Chebyshev distribution and a mapping is applied as in Khorrami *et al.* (1989). This leads to a generalized matrix eigenvalue problem, which represents the dispersion relation for this

---

[1]The results contained in this section have been kindly provided by my supervisor, Dr. Matthew Juniper.
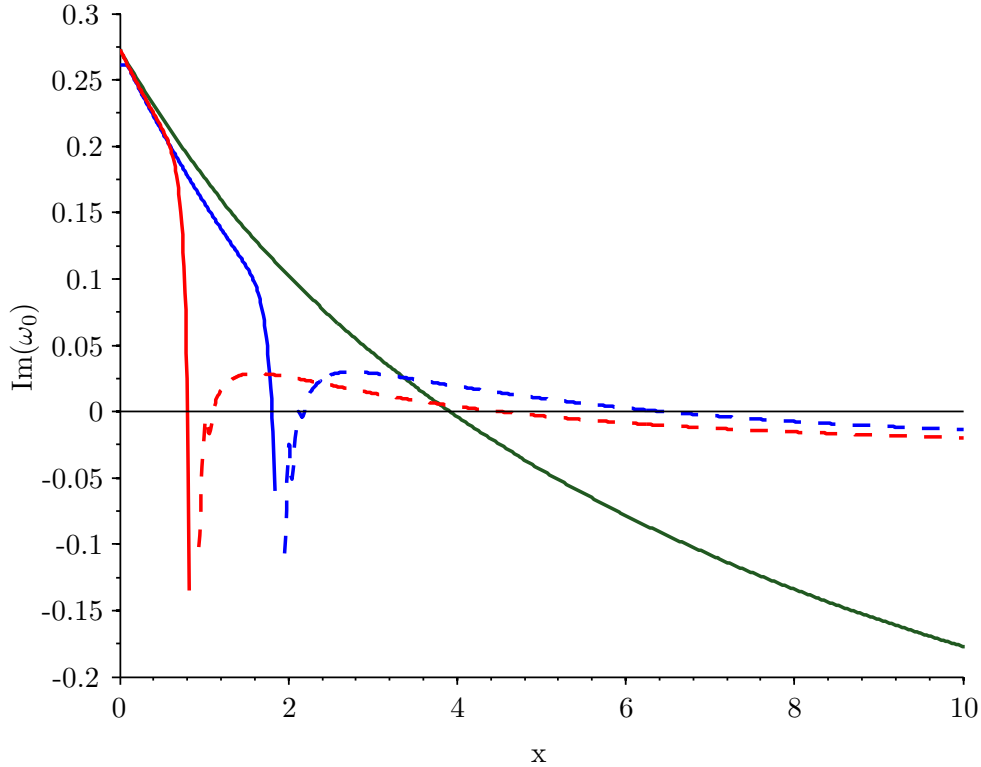
Figure 4.10: Absolute growth rates as a function of axial distance calculated by a local analysis for the non-reacting (green), $h_l = 0.858$ (red) and $h_l = 1.92$ (blue) cases. The solid lines correspond to the most dominant saddle and the dashed lines correspond a secondary saddle.

axial location. This is solved for complex k and ω with Matlab's function `eig` and the valid k^+/k^- saddle points are found with Instaflow (Correia Da Costa, 2009), which is a Matlab graphical user interface (GUI) that performs local stability analysis. This gives the absolute growth rate (the growth rate at the saddle point) as a function of downstream distance, which is shown in figure 4.10. Axial locations where $\text{Im}(\omega_0) > 0$ are absolutely unstable, whereas axial locations where $\text{Im}(\omega_0) < 0$ are convectively unstable. The real-valued x-axis can be considered to be the real axis in a complex x-plane. ω_0 is therefore the value of ω on the real axis of the complex x-plane. With the imaginary part of ω_0 corresponding to the absolute growth, the real part of ω_0 corresponds to the absolute frequency in radians per non-dimensional time unit and is shown in figure 4.11.
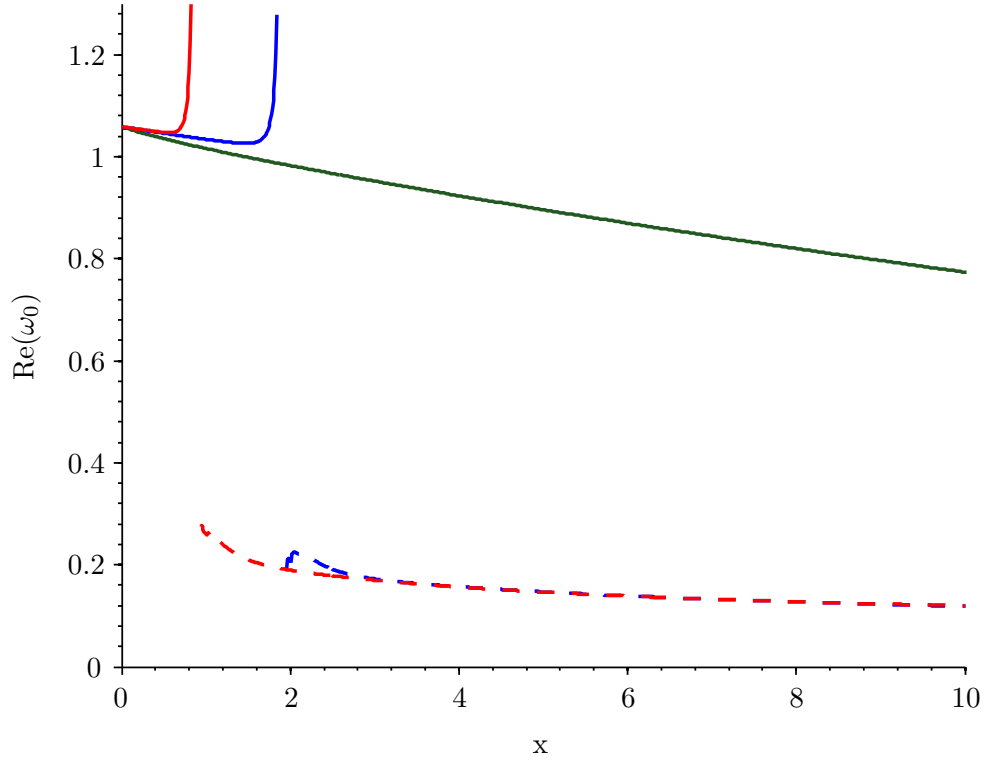
Figure 4.11: Absolute frequency as a function of axial distance calculated by a local analysis for the non-reacting (green), $h_l = 0.858$ (red) and $h_l = 1.92$ (blue) cases. The solid lines correspond to the most dominant saddle and the dashed lines correspond a secondary saddle.

For both reacting cases, an absolutely unstable region occurs in the pre-mixing zone and, near to the inlet, the corresponding growth rates and frequencies match closely those of the non-reacting case. The pocket of absolute instability in the non-reacting case extends to $x = 3.9$, which compares favourably to the value of 3.71 found by Nichols & Schmid (2008). For the reacting cases, this pocket of absolute instability extends only as far as the base of the flame. It was suggested by Nichols & Schmid that this pocket of absolute instability determines the global stability of the flow and as the pre-mixing zone, and associated absolutely unstable region, become shorter, the global instability is suppressed. This matches the findings of this work, where the $h_l = 1.92$ case is globally unstable and the $h_l = 0.858$ case is globally stable. The growth rate of the global mode for the $h_l = 1.92$ case, however, is approximately 4

times the growth rate of the global mode of the hot jet (see table 4.1). In this case, the flame has enhanced the global instability, despite suppressing the absolute instability downstream of the flame base.

To extend this analysis, secondary k^+/k^- saddle points were sought for in the flame region. In both reacting cases, a secondary saddle was found with a pocket of absolute instability in the flame region, shown by the dashed lines in figure 4.10. For both cases, this secondary absolutely unstable region is longer but weaker than the pocket of absolute instability in the pre-mixing zone. Despite this long secondary absolutely unstable region, the $h_l = 0.858$ case is globally stable. This situation, where a long region of slight absolute instability is globally stable, has been analysed by Pier (2010).

These observations indicate that, despite absolute instability existing in the flame region, Nichols & Schmid were correct in assuming the pocket of absolute instability in the pre-mixing zone determines the global stability of the flow. This implies that, for the $h_l = 1.92$ case in this work, the global mode arising from the absolutely unstable region in the pre-mixing zone dominates the absolutely unstable region in the flame.

4.5.1 Wavemaker

The local analysis can be extended to give global information by identifying the position of the wavemaker (Huerre & Monkewitz, 1990). The value of ω at the wavemaker position is then taken to be the global value ω_g, with the real and imaginary parts corresponding to the frequency $(2\pi St)$ and growth rate of the global instability. ω_g can be compared directly to $i\sigma$, where σ is the most-unstable direct linear eigenvalue. It is worth pointing out that the direct eigenvalues occur in complex-conjugate pairs and by selecting the eigenvalue with negative imaginary part, $\mathrm{Re}(i\sigma)$ is positive, which compares directly to $\mathrm{Re}(\omega_g)$.

The wavemaker location is found by extending ω_0 into the complex x-plane and finding the position of a global mode saddle point. The present analysis is complicated by all the cases having greatest absolute instability at the inlet. To overcome this, ω_0 was padded with zeros in the upstream region: $-1 < x < 0$. A representation of $\omega_0(x)$ was found with a 5th-order polynomial interpolation, which was then used to locate saddle points in the complex x-plane. As the number of polynomials used in the interpolation is increased only one saddle point remains approximately stationary, which is the one used as the position of the wavemaker. This method is in contrast to

Case	Nonlinear N&S: $2\pi\,St$	Direct linear eigenvalue: $\mathrm{i}\sigma$	Local analysis: ω_g	Local analysis N&S: $\mathrm{Re}(\omega_0(0))$
Non-reacting	1.332	$1.10 + \mathrm{i}\,0.042$	$1.06 + \mathrm{i}\,0.20$	1.06
$h_l = 0.858$	1.784	$1.98 - \mathrm{i}\,0.094$	$1.11 + \mathrm{i}\,0.25$	1.06
$h_l = 1.92$	/	$1.35 + \mathrm{i}\,0.18$	$1.09 + \mathrm{i}\,0.23$	/

Table 4.1: Comparison of ω_g from a local analysis, direct linear eigenvalues and non-linear global mode frequencies. The real parts of $\mathrm{i}\sigma$ and ω_g correspond to the non-dimensional frequency in radians per non-dimensional time unit and the imaginary parts correspond to the growth rate of the global mode. N&S refers to the results of Nichols & Schmid (2008).

that of Nichols & Schmid (2008), who compared the $\mathrm{Re}(\omega_0)$ at the inlet to the frequency of the nonlinear global mode. Table 4.1 compares the values found with the wavemaker approach to the results of Nichols & Schmid and to the eigenvalues of the most-unstable direct linear global modes.

The differences between the linear eigenvalues and nonlinear frequencies are discussed in section 4.1.1. The discrepancies seen in table 4.1 between the local and global results could be due to the inlet boundary. The local analysis is performed assuming the flow extends infinitely up- and downstream, whereas the global analyses have a homogeneous-Dirichlet inlet boundary for the perturbation fields.

Considering the second k^+/k^- saddle in the flame region, a second global mode saddle point can be found corresponding to the longer but lower amplitude absolutely unstable region in the flame. The global growth rates are $\mathrm{Im}(\omega_{g2}) = 0.0028$ and $\mathrm{Im}(\omega_{g2}) = 0.0020$ for the $h_l = 0.858$ and $h_l = 1.92$ cases respectively. These values are positive, which means that, according to the local analysis, the absolute instability in the flame region alone is sufficient for global instability. The negative imaginary part of $\mathrm{i}\sigma$ for the $h_l = 0.858$ case contradicts this finding. In both cases $\mathrm{Im}(\omega_{g2})$ is an order of magnitude smaller than the maximum value of $\mathrm{Im}(\omega_0)$ in the flame region and two orders of magnitude smaller than the value of $\mathrm{Im}(\omega_g)$ at the global mode saddle point associated with the absolute instability in the pre-mixing zone. With values close to zero, it is possible that a small discrepancy has shifted ω_{g2} from the stable half-plane to the unstable half-plane.

It is claimed by Giannetti & Luchini (2007) that the instability core (see section 4.3) 'takes account of the feedback which is at the origin of the self-excited oscillation

Case	Wavemaker axial location	Instability core axial location
Non-reacting	0.83	7.0
$h_l = 0.858$	0.30	0.35
$h_l = 1.92$	0.42	0.90

Table 4.2: Comparison of wavemaker and instability core location.

and is therefore useful to locate the region of the flow which acts as a wavemaker'. Table 4.2 compares the wavemaker locations to the instability core locations found in section 4.3. For both reacting cases the instability core and wavemaker are located in the absolutely unstable region in the pre-mixing zone. For $h_l = 0.858$ the locations match reasonably well. For the non-reacting case, however, the instability core lies outside of the absolutely unstable region and differs significantly from the position of the wavemaker.

The discrepancies seen in tables 4.1 and 4.2 highlight a current limitation in extending the local analysis to global instabilities. More investigation is needed into determining the position of the wavemaker via a local analysis and into the relationship between the wavemaker and the instability core defined by Giannetti & Luchini (2007).

4.6   Conclusions

The aim of this chapter is to provide sensitivity information for low-density jet flow and in particular low-density reacting jet flow. By providing a physical meaning for the adjoint global modes and calculating the sensitivity to an assumed feedback mechanism in the flow this aim has been met. In addition to this, the sensitivity to the placement of a hot wire provides a physically realisable problem with which to compare to experimental data and the local analysis provides greater insight into the underlying hydrodynamic instability and interpretation of the sensitivity information.

The adjoint global mode gives the sensitivity of the amplitude of the direct global mode to open-loop forcing and heating and, for the jet flows considered here, the adjoint global modes show that the most sensitive region is near the flow inlet. This is supported by findings from the local analysis that show the inlet to be the region of maximum absolute instability. For the lifted flames the spatial structure of the adjoint global

modes is of low amplitude in the flame and grows rapidly in the pre-mixing zone, which shows that the modal amplitude is relatively insensitive to forcing or heating applied locally in the flame.

The framework of Giannetti & Luchini (2007) has been successfully extended to reacting flows with density variation. On comparison to a local analysis, however, the instability core and wavemaker do not always coincide. This is in contrast to the suggestion by Giannetti & Luchini that the instability core is an alternative way to calculate the location of the wavemaker. The position of the instability core for the hot jet is, in fact, outside of the absolutely unstable region, which questions the suggested link between the two concepts. The instability core is, however, of fundamental interest and, rather than see it as an alternative to the wavemaker, perhaps it should be considered as additional information that improves our overall understanding of the hydrodynamic instability.

In addition to the calculation of the instability core, the formulation used in this work gives a more general framework for analyzing operator perturbations and feedback couplings, which was demonstrated by applying the same framework to look at the sensitivity to the placement of a hot wire. The present framework also allows the sensitivity of the growth rate and frequency of the global mode to be considered separately, which has given some unexpected results. It appears that, while the magnitude of the change in the eigenvalue varies on a long spatial length scale, the frequency and growth rate vary on much shorter spatial length scales. This produces the situation where a small change in location can result in changing from suppression to enhancement (or vice-versa) of the instability.

A prevailing theme in all four analyses in this chapter is the importance of the pre-mixing zone to the global instability of lifted flames. It is the region of greatest absolute instability; the region that contains the wavemaker; the region where the amplitude of the global mode is most sensitive to open-loop forcing; the region where the most-unstable eigenvalue is most sensitive to a perturbation in the proposed hydrodynamic force-momentum feedback coupling and the region where the most-unstable eigenvalue is most sensitive to the heat release from a hot wire. This shows that, despite the presence of reaction, the hydrodynamic instability due to the non-reacting shear layer is the most influential part of the flow.

CHAPTER 5

Future work

5.1 Three spatial dimensions

The obvious next step is to extend the present work to three spatial dimensions. This is especially important because of the non-normality of the governing operator. Although the largest exponential growth is typically found for perturbations without a spanwise dependence, transient amplification is often maximal for perturbations with a spanwise dependence (Butler & Farrell, 1992; Trefethen *et al.*, 1993; Schmid, 2007). This challenges the common use of Squire's theorem (Drazin & Reid, 1981) to justify simplifying three-dimensional problems to two dimensions.

It has been found by Delbende *et al.* (1998) (carrying out a DNS study of the linear impulse response of a parallel Batchelor vortex) and Olendraru *et al.* (1999) (using an absolute/convective instability approach) that swirl strongly promotes absolute instability. A similar conclusion was made by Heaton *et al.* (2009), who applied DNS to investigate the spatially evolving Batchelor vortex. Including swirl is therefore important. Initially, an axisymmetric base flow with swirl could be used with three-dimensional perturbations.

The cylindrical domain in this work lends itself to using Fourier modes in the azimuthal direction and as a consequence the values of the fields in the code must become complex. A useful property is that the Fourier modes are independent and can run relatively easily on separate nodes of a high performance cluster. Provided there are enough nodes available, the computational time to run three-dimensional calculations will not increase significantly.

5.2   Complex geometries

Complex geometry is required to model real fuel injectors. There are three possible paths to follow: include immersed boundaries in the existing finite difference code, as used by Giannetti & Luchini (2007); switch to an existing finite element code; or create a finite element code from scratch using software such as Freefem++, as used by Meliga (2008).

Freefem++ is a finite element partial differential equation (PDE) solver with built in meshing and solution procedures. The user can implement their own PDEs, solution algorithms and boundary conditions with relative ease compared to using a programming language such as Fortran. This lends itself particularly well to implementing adjoint equations and because the whole direct matrix is computed as part of the solution procedure, a discrete-adjoint code can be easily obtained.

Immersed boundaries have been implemented successfully in finite difference codes for a variety of different flow applications. A comprehensive review is given by Mittal & Iaccarino (2005). Immersed boundaries allow for the use of regular centred differencing across the whole domain, by either directly adjusting values near the boundaries (Fadlun *et al.*, 2000) or introducing an artificial force in the governing equations (Goldstein *et al.*, 1993), both of which can be set up to mimic a solid wall. This is especially useful for flows with moving boundaries such as in the cylinders of piston engines (Fadlun *et al.*, 2000).

The direct adjustment of values near the boundary is used by Giannetti & Luchini (2007) and is probably the more useful of the two types for this application. With this method the domain is essentially split up into the live region (where the fluid is flowing), a ghost region (a region around the boundary where flow values are adjusted to give the correct boundary condition), and a dead region (inside the boundary where the flow can be either left to its own devices or set to a constant value).

A 2nd-order finite difference scheme typically uses values at two grid points to calculate a derivative. The ghost region needs to include therefore only one grid point in order to be as accurate as the differencing scheme, i.e. in order to set the correct boundary condition (Neumann or Dirichlet for example) only one grid point near the boundary needs to be adjusted. As the order of the scheme increases more points are used in the differencing scheme and the ghost region must get thicker in order to maintain the correct boundary conditions. For the compact finite differencing currently

used in this work this might be a problem, because the scheme is considered to have spectral accuracy (see Goldstein *et al.*, 1993, for the implementation of an immersed boundary in a spectral code). Using toy models in Matlab, it was found that a ghost region of 6 or 7 grid points is required to stop unwanted oscillations in the derivatives near the boundary. This in turn restricts the maximum radius of curvature of the boundary shape. For boundary profiles curving away from the fluid, including at least 6 or 7 grid points and avoiding overlap of the grid points makes sharp corners impossible to achieve.

To implement a curved immersed boundary in the existing code would require a wide ghost region and a significant amount of interpolation. This would be quite complex and may be costly to implement at each time step. Alternatively the compact difference scheme could be exchanged for a lower-order scheme, which would help with the inclusion of an immersed boundary but would decrease the overall accuracy of the code.

5.3 Turbulence

The flow inside combustion chambers in aircraft is turbulent. Simulating turbulence with DNS is prohibitively expensive, so turbulence models would be a useful addition to the current code. A discrete-adjoint version of the code with turbulence models could be formed without too much extra difficulty and it should be possible to derive a set of adjoint equations that include the turbulence models too.

5.4 Acoustic forcing

Using a similar approach to that of Moeck *et al.* (2009), acoustic forcing can be modelled as a body force in the low-Mach-number equations. This is a specific type of open-loop forcing and so the sensitivity of the modal amplitude to the location, structure and frequency of the acoustic signal can be found. For reacting flow this is a thermoacoustic problem and has particular relevance to combustion instability. Investigating the effects of acoustic forcing in a three-dimensional reacting jet would be a useful step up from the one-dimensional Rijke tube, which is the canonical thermoacoustics problem.

5.5   Optimal spark position

The time-stepping codes could be used in optimization routines to find optimal initial perturbations and optimal forcing or heating. Localization of the initial perturbations or forcing can also be included. This is relatively easy to do, but a clear reason for doing it must be found. A possible useful area might be to try to find optimal conditions on the perturbation inlet boundary. This may be of use if transient effects from inlet disturbances can alter the dynamics in combustion chambers.

A problem suited to optimal perturbation techniques is the optimal position to place a spark to ignite the flow. To see how this could be tackled, a power iteration optimization routine was set up to find the optimal initial temperature perturbation distribution that leads to the maximum increases in thermal energy. No results are included because this was carried out with linear theory, which is a poor approximation for the heat release due to reaction when the temperature rises even by a small amount.

Nevertheless to show how optimal perturbations could be applied to the spark placement problem, an unignited cold steady base flow was found and used for the linear optimization routine. The reaction rate was artificially altered to encourage reaction. The perturbations were evolved forward in time with the direct code, rescaled and localized to the temperature field, and then evolved backwards in time with the adjoint code. They were then rescaled and localized to the temperature field again. The optimal perturbation is the eigenmode corresponding to the most-unstable eigenvalue of this loop and was found with both power iteration and with ARPACK. The optimal perturbation found favoured the region just outside the jet near the inlet, presumably because the heat there gets entrained into the jet slowly.

This preliminary linear optimization provides a starting point for a nonlinear optimization similar to those performed by Zuccher *et al.* (2006) and Juniper (2011). The starting condition would be a cold flow that would either be a steady solution of the unignited nonlinear problem or a snapshot from a time evolution of an unignited nonlinear global mode. The temperature starting condition would be the cold temperature plus positive white noise. The flow would be evolved forward in time with the fully-nonlinear operator and then backward in time with the adjoint of the nonlinear operator. Because the adjoint of the nonlinear operator is actually linear the result can be rescaled. The new temperature field would then replace the old temperature field in the original cold starting condition and the loop repeated until convergence.

5.6 Sensitivity of nonlinear global modes and secondary instabilities

One of the main limitations of the linear sensitivity analysis is the restriction that the flow must be near the first bifurcation point in order to extend the linear results into the the fully-nonlinear regime (Chomaz, 2005). Luchini *et al.* (2008) and Giannetti *et al.* (2010) extend the analysis of Giannetti & Luchini (2007) to include the sensitivity of the nonlinear global mode and secondary instability of the cylinder wake. Fuel injectors operate far from the first bifurcation point and well into the nonlinear regime, so the current work should be extended to take this into account.

5.7 Dynamic modes

Dynamic mode decomposition is a new area of interest (Rowley *et al.*, 2009; Schmid, 2010). It would be interesting to calculate dynamic modes for the fully-nonlinear flame. Given that the direct linear eigenmodes have a set of corresponding adjoint modes and the adjoint of a nonlinear operator is known to exist, it seems plausible that there could be a set of adjoint modes that correspond to the set of direct dynamic modes. Luchini *et al.* (2008) and Giannetti *et al.* (2010) calculate a set of adjoint Floquet modes that exist on top of a time evolving base flow formed by the nonlinear global mode, but these correspond to the linear direct Floquet modes of that base flow. Each dynamic mode could be used as a time-evolving base flow and a set of direct and adjoint Floquet modes could be found. It may be helpful to think of the nonlinear direct problem as a time evolving matrix acting on a vector, where the matrix contains the vector itself. The transpose of this matrix at each time instant gives a discrete-adjoint algorithm for the nonlinear problem and might provide a clue to obtaining a set of adjoint modes corresponding to the set of direct dynamic modes.

5.8 Sensitivity to steady source terms

As discussed in chapter 1, the sensitivity to steady source terms is likely to be more useful for design applications. A steady force or heat source does not appear in the linear perturbation equations. Instead they appear on the right hand side of the base flow equations and alter the base flow fields, which in turn alter the eigenvalues and

global modes. The sensitivity of the eigenvalue to changes in the steady source terms is therefore a structural sensitivity of the eigenvalue to changes in the linear operator in (4.1). The extra complexity involved in calculating this sensitivity favours using a Lagrange-multiplier approach similar to Marquet (2008) and Meliga (2008), who calculated the sensitivity to steady forcing for the incompressible and fully compressible cases respectively.

The sensitivity to arbitrary base flow modifications without connection to a steady source has not been included as part of this analysis. The arbitrary choices made when using the base flow equations to form the linear operator cause changes to the sensitivity of the eigenvalue to particular base flow quantities. For example, if the base flow state equation is used to replace $\bar{T}$ everywhere in the direct equations with a term containing $\bar{\rho}$, then the eigenvalue will no longer have any dependence to arbitrary changes in $\bar{T}$ and the sensitivity of the eigenvalue to arbitrary changes in $\bar{T}$ will change from a non-zero value to zero. Specifying a sensitivity to a base flow modification alone does not therefore yield a specific solution, which makes it difficult to extract a physical meaning. The base flow fields are constrained by the base flow equations and arbitrary changes can violate these constraints. Considering an arbitrary change in one quantity may cause others to vary in an unclear way. To alter the base flow quantities without violating constraints, it is necessary to change parameters in the base flow equations. This means that when combined in the full analysis - of sensitivity to changes in the steady source terms - the arbitrary choices made when using the base flow equations to form the linear operator have no net effect and a specific solution can be found.

The Lagrangian formulation is usually considered as a method of solving constrained optimization problems, but more generally it can be used to calculate total derivatives of constrained functions. Consider the Lagrangian $\mathcal{L}$ as a function of variables x and y and Lagrange multipliers α and β:

$$\mathcal{L}(x, y, \alpha, \beta) = f(x, y) - \alpha\, g(x, y) - \beta\, h(x, y),$$

where $g(x, y)$ and $h(x, y)$ are constraints and $f(x, y)$ is the function of interest. When all constraints are obeyed, the Lagrangian and its derivatives are equal to the function of interest and its derivatives. The total derivative of $\mathcal{L}$ with respect to x is given by

$$\frac{d\mathcal{L}}{dx} = \frac{\partial \mathcal{L}}{\partial x} + \frac{\partial \mathcal{L}}{\partial y}\frac{dy}{dx} + \frac{\partial \mathcal{L}}{\partial \alpha}\frac{d\alpha}{dx} + \frac{\partial \mathcal{L}}{\partial \beta}\frac{d\beta}{dx}.$$

Calculating the partial derivatives of $\mathcal{L}$ with respect to y, α and β and setting them to

zero yields a set of values that ensures the total derivative with respect to x equals the partial derivative with respect to x.

For the sensitivity of the eigenvalue to changes in the base flow, the function of interest is the eigenvalue σ and the constraints are the linear equations (2.13) and base flow equations (2.2) with Lagrange multipliers being the adjoint global mode fields and adjoint base flow fields respectively. The Lagrangian for the non-reacting system is therefore

$$
\begin{aligned}
\mathcal{L} = \sigma &- \left\langle \hat{p}^+, (S_1 - 1)\left(\bar{m}_i \frac{\partial \hat{T}}{\partial x_i} - \frac{1}{S_1 RePr} \frac{\partial^2 \hat{T}}{\partial x_i{}^2} \right) + \frac{\partial}{\partial x_i}\left(\frac{\hat{m}_i}{\bar{\rho}} \right) \right\rangle \ldots \\
&- \left\langle \hat{m}_i^+, \sigma \hat{m}_i + \frac{\partial}{\partial x_j}\left(\frac{\bar{m}_j \hat{m}_i}{\bar{\rho}} + \frac{\hat{m}_j \bar{m}_i}{\bar{\rho}} - \frac{\hat{\rho} \bar{m}_j \bar{m}_i}{\bar{\rho}^2} \right) + \frac{\partial \hat{p}}{\partial x_i} \right. \ldots \\
&\qquad \left. - \frac{1}{S_1 Re}\left(\frac{\partial^2}{\partial x_j{}^2}\left(\frac{\hat{m}_i}{\bar{\rho}} - \frac{\hat{\rho}\bar{m}_i}{\bar{\rho}^2} \right) + \frac{1}{3}\frac{\partial^2}{\partial x_j \partial x_i}\left(\frac{\hat{m}_j}{\bar{\rho}} - \frac{\hat{\rho}\bar{m}_j}{\bar{\rho}^2} \right) \right) - Ri\hat{\rho}\hat{g}_i \right\rangle \ldots \\
&- \left\langle \hat{T}^+, \sigma \hat{T} + \frac{\bar{m}_i}{\bar{\rho}}\frac{\partial \hat{T}}{\partial x_i} + \frac{\hat{m}_i}{\bar{\rho}}\frac{\partial \bar{T}}{\partial x_i} - \frac{1}{S_1 RePr}\frac{1}{\bar{\rho}}\frac{\partial^2 \hat{T}}{\partial x_i{}^2} \right\rangle \ldots \\
&- \left\langle \hat{\rho}^+, \frac{\hat{\rho}}{\bar{\rho}^2} + (S_1 - 1)\hat{T} \right\rangle \ldots \\
&- \left\langle \bar{p}^+, \frac{\partial \bar{m}_i}{\partial x_i} - \bar{\varrho} \right\rangle \ldots \\
&- \left\langle \bar{m}_i^+, \frac{\partial \bar{p}}{\partial x_i} + \frac{\partial}{\partial x_j}\left(\frac{\bar{m}_j \bar{m}_i}{\bar{\rho}} \right) \right. \ldots \\
&\qquad \left. - \frac{1}{S_1 Re}\left(\frac{\partial^2}{\partial x_j{}^2}\left(\frac{\bar{m}_i}{\bar{\rho}} \right) + \frac{1}{3}\frac{\partial^2}{\partial x_j \partial x_i}\left(\frac{\bar{m}_j}{\bar{\rho}} \right) \right) + Ri(1 - \bar{\rho})\hat{g}_i - \bar{f}_i \right\rangle \ldots \\
&- \left\langle \bar{T}^+, \bar{m}_i \frac{\partial \bar{T}}{\partial x_i} - \frac{1}{S_1 RePr}\frac{\partial^2 \bar{T}}{\partial x_i{}^2} - \bar{\varphi} \right\rangle \ldots \\
&- \left\langle \bar{\rho}^+, \bar{\rho}\left((S_1 - 1)\bar{T} + 1 \right) - 1 \right\rangle, \\
&- \int_S (\bar{m}_{wi}^+)^* \left(\bar{m}_i - \bar{m}_{wi} \right) + (\bar{T}_w^+)^* \left(\bar{T} - \bar{T}_w \right) \; dS
\end{aligned}
$$

(5.1)

where $\bar{\varrho}$ is the steady, non-dimensional rate of mass addition per unit volume, $\bar{f}_i$ is the steady, non-dimensional external force per unit volume and $\bar{\varphi}$ is the steady, non-dimensional rate of heat addition per unit volume. The last term in (5.1) is the constraint of the base flow boundary conditions, $\bar{m}_{wi}$ and $\bar{T}_w$, multiplied by the Lagrange multipliers $\bar{m}_{wi}^+$ and $\bar{T}_w^+$. Including the constraint imposed by the boundary conditions allows for the sensitivity to wall forcing and heating (Meliga, 2008).

The functional derivative of the Lagrangian with respect to the variable a is defined as

$$\langle \nabla_a \mathcal{L}, \delta a \rangle = \lim_{\varepsilon \to 0} \left(\frac{\mathcal{L}(a + \varepsilon \delta a) - \mathcal{L}(a)}{\varepsilon} \right). \tag{5.2}$$

We are interested in the functional derivative of $\mathcal{L}$ with respect to $\bar{\varrho}$, $\bar{f}_i$ and $\bar{\varphi}$, but in order for this derivative to be a total derivative, the functional derivatives with respect to all the other variables must be calculated and set to zero. Using (5.2) to take the functional derivatives with respect to the the adjoint global mode fields and adjoint base flow fields gives back the linear and base flow equations, which, by definition, are equal to zero. The functional derivatives with respect to the linear global mode fields yield the adjoint equations, which when set to zero are solved to give the adjoint global mode fields. The functional derivative with respect to σ gives

$$\nabla_\sigma \mathcal{L} = 1 - \langle \hat{m}_i^+, \hat{m}_i \rangle - \langle \hat{T}^+, \hat{T} \rangle = 0, \tag{5.3}$$

$$\Rightarrow \langle \hat{m}_i^+, \hat{m}_i \rangle + \langle \hat{T}^+, \hat{T} \rangle = 1, \tag{5.4}$$

which provides a normalization condition for the adjoint global mode fields.

The functional derivative with respect to the base flow fields, $\bar{p}$, $\bar{m}_i$, $\bar{T}$ and $\bar{\rho}$ requires much more algebra. The fields are first grouped together and the vector $\bar{q}$ and $\bar{q} + \varepsilon \delta \bar{q}$, (containing $\bar{p} + \varepsilon \delta \bar{p}$, $\bar{m}_i + \varepsilon \delta \bar{m}_i$, $\bar{T} + \varepsilon \delta \bar{T}$ and $\bar{\rho} + \varepsilon \delta \bar{\rho}$) is substituted into (5.1). Equation (5.1) is then linearized and multiple integrations by parts are performed to shift $\delta \bar{p}$, $\delta \bar{m}_i$, $\delta \bar{T}$ and $\delta \bar{\rho}$ to the right hand sides of the separate inner products. The inner products are then regrouped to give the functional derivatives with respect to $\bar{p}$, $\bar{m}_i$, $\bar{T}$ and $\bar{\rho}$, which are set to zero. This gives

$$\frac{\partial \bar{m}_i^+}{\partial x_i} = 0, \tag{5.5a}$$

$$-\frac{\bar{m}_j}{\bar{\rho}} \left(\frac{\partial \bar{m}_i^+}{\partial x_j} + \frac{\partial \bar{m}_j^+}{\partial x_i} \right) - \frac{1}{S_1 Re \bar{\rho}} \left(\frac{\partial^2 \bar{m}_i^+}{\partial x_j^2} + \frac{1}{3} \frac{\partial^2 \bar{m}_j^+}{\partial x_j \partial x_i} \right) - \frac{\partial \bar{p}^+}{\partial x_i} + \bar{T}^+ \frac{\partial \bar{T}}{\partial x_i} = \bar{f}_i^+, \tag{5.5b}$$

$$-\bar{m}_i \frac{\partial \bar{T}^+}{\partial x_i} - \frac{1}{S_1 Re Pr} \frac{\partial^2 \bar{T}^+}{\partial x_i^2} + (S_1 - 1) \bar{\rho}^+ = \bar{\varphi}^+, \tag{5.5c}$$

$$\frac{\bar{m}_i \bar{m}_j}{\bar{\rho}^2} \frac{\partial \bar{m}_i^+}{\partial x_j} + Ri \bar{m}_i^+ \hat{g}_i + \frac{\bar{m}_i}{S_1 Re \bar{\rho}^2} \left(\frac{\partial^2 \bar{m}_i^+}{\partial x_j^2} + \frac{1}{3} \frac{\partial^2 \bar{m}_j^+}{\partial x_j \partial x_i} \right) + \frac{\bar{\rho}^+}{\bar{\rho}^2} = \bar{\varrho}^+, \tag{5.5d}$$

with $\bar{f}_i^+$, $\bar{\varphi}^+$ and $\bar{\varrho}^+$ defined as

$$\bar{f}_i^+ \equiv -\left(S_1 - 1\right)\hat{p}^+ \frac{\partial \hat{T}^*}{\partial x_i} + \left(\frac{\hat{m}_j^*}{\bar{\rho}} - \frac{\hat{\rho}^* \bar{m}_j}{\bar{\rho}^2}\right)\left(\frac{\partial \hat{m}_i^+}{\partial x_j} + \frac{\partial \hat{m}_j^+}{\partial x_i}\right)\cdots$$
$$-\frac{\hat{\rho}^*}{S_1 Re \bar{\rho}^2}\left(\frac{\partial^2 \hat{m}_i^+}{\partial x_j^2} + \frac{1}{3}\frac{\partial^2 \hat{m}_j^+}{\partial x_j \partial x_i}\right) - \frac{\hat{T}^+}{\bar{\rho}}\frac{\partial \hat{T}^*}{\partial x_i}, \tag{5.6a}$$

$$\bar{\varphi}^+ \equiv \frac{\partial}{\partial x_j}\left(\frac{\hat{T}^+ \hat{m}_j^*}{\bar{\rho}}\right), \tag{5.6b}$$

$$\bar{\varrho}^+ \equiv 2\frac{\hat{\rho}^* \hat{\rho}^+}{\bar{\rho}^3} - \frac{\hat{m}_j^*}{\bar{\rho}}\frac{\partial \hat{p}^+}{\partial x_j} + \frac{\hat{T}^+}{\bar{\rho}^2}\left(\bar{m}_j\frac{\partial \hat{T}^*}{\partial x_j} + \hat{m}_j^*\frac{\partial \bar{T}}{\partial x_j}\right)\cdots$$
$$-\frac{\hat{T}^+}{S_1 Re Pr \bar{\rho}^2}\frac{\partial^2 \hat{T}^*}{\partial x_j^2} - \left(\frac{\bar{m}_i \hat{m}_j^*}{\bar{\rho}^2} + \frac{\hat{m}_i^* \bar{m}_j}{\bar{\rho}^2} - \frac{2\hat{\rho}^* \bar{m}_i \bar{m}_j}{\bar{\rho}^3}\right)\frac{\partial \hat{m}_i^+}{\partial x_j}\cdots$$
$$-\frac{1}{S_1 Re}\left(\frac{\hat{m}_i^*}{\bar{\rho}} - \frac{2\hat{\rho}^* \bar{m}_i}{\bar{\rho}^3}\right)\left(\frac{\partial^2 \hat{m}_i^+}{\partial x_j^2} + \frac{1}{3}\frac{\partial^2 \hat{m}_j^+}{\partial x_j \partial x_i}\right), \tag{5.6c}$$

where a^* is the complex conjugate of a.

The integration by parts to form (5.5) gives rise to a number of boundary terms similar to those in (2.50). Using the divergence theorem these can be transformed into a surface integral. Setting this to zero will give the boundary conditions for the solution of (5.5), but it is more useful to first combine it with the boundary constraint term in (5.1), so that values for $\bar{m}_{w\,i}^+$ and $\bar{T}_w^+$ can be determined.

The system of equations (5.5) closely resembles the adjoint perturbation equations with the time derivative terms removed and with source terms added on the right hand side. If we substitute

$$\bar{p}^+ = \frac{p^+}{\bar{\rho}}, \tag{5.7a}$$

$$\bar{m}_i^+ = m_i^+, \tag{5.7b}$$

$$\bar{T}^+ = \frac{T^+}{\bar{\rho}} + \left(S_1 - 1\right)p^+, \tag{5.7c}$$

$$\bar{\rho}^+ = \rho^+, \tag{5.7d}$$

into (5.5) and multiply (5.5d) by $\bar{\rho}^2$, the homogeneous part of the new equations recovers the exact from of the steady adjoint perturbation equations (2.15).

The source terms in (5.6) are functions only of the linear and adjoint global modes, and the base flow fields. These terms can therefore be calculated using the results from chapters 2 and 3, and then be used in the solution of (5.5). A possible solution procedure

is to introduce the source terms $\bar{f}_i^+$, $\bar{\varphi}^+$ and $\bar{\rho}^2 \bar{\varrho}^+$ into the continuous-adjoint code and use selective frequency damping (Åkervik *et al.*, 2006) to converge to a steady solution. The adjoint base flow fields can then be found using (5.7). The continuous-adjoint code has not been altered yet and so only the theory is presented in this thesis.

Now that we have set all these derivatives to zero, we can calculate the total derivative of $\mathcal{L}$ with respect to $\bar{\varrho}$, $\bar{\boldsymbol{f}}$, $\bar{\varphi}$, $\bar{\boldsymbol{m}}_w$ and $\bar{T}_w$ by using the functional derivative in (5.2). Applying (5.2) to each steady source term and the boundary conditions gives

$$\langle \nabla_{\bar{\varrho}} \mathcal{L}, \delta\bar{\varrho} \rangle = \langle \bar{p}^+, \delta\bar{\varrho} \rangle, \tag{5.8a}$$

$$\langle \nabla_{\bar{\boldsymbol{f}}} \mathcal{L}, \delta\bar{\boldsymbol{f}} \rangle = \langle \bar{\boldsymbol{m}}^+, \delta\bar{\boldsymbol{f}} \rangle, \tag{5.8b}$$

$$\langle \nabla_{\bar{\varphi}} \mathcal{L}, \delta\bar{\varphi} \rangle = \langle \bar{T}^+, \delta\bar{\varphi} \rangle, \tag{5.8c}$$

$$\int_S (\nabla_{\bar{\boldsymbol{m}}_w} \mathcal{L})^H \, \delta\bar{\boldsymbol{m}}_w \, dS = \int_S (\bar{\boldsymbol{m}}_w^+)^H \, \delta\bar{\boldsymbol{m}}_w \, dS, \tag{5.8d}$$

$$\int_S (\nabla_{\bar{T}_w} \mathcal{L})^* \, \delta\bar{T}_w \, dS = \int_S (\bar{T}_w^+)^* \, \delta\bar{T}_w \, dS. \tag{5.8e}$$

Remembering that $\mathcal{L}$ is equivalent to the constrained eigenvalue σ, the sensitivity of σ to changes in $\bar{\varrho}$, $\bar{\boldsymbol{f}}$, $\bar{\varphi}$, $\bar{\boldsymbol{m}}_w$ and $\bar{T}_w$ is

$$\nabla_{\bar{\varrho}} \sigma = \bar{p}^+, \tag{5.9a}$$

$$\nabla_{\bar{\boldsymbol{f}}} \sigma = \bar{\boldsymbol{m}}^+, \tag{5.9b}$$

$$\nabla_{\bar{\varphi}} \sigma = \bar{T}^+, \tag{5.9c}$$

$$\nabla_{\bar{\boldsymbol{m}}_w} \sigma = \bar{\boldsymbol{m}}_w^+, \tag{5.9d}$$

$$\nabla_{\bar{T}_w} \sigma = \bar{T}_w^+. \tag{5.9e}$$

The analysis presented here is for the non-reacting system, however a similar analysis could be performed for the reacting system with only minor changes.

CHAPTER 6

Concluding remarks

The work presented in this thesis is part of a wider project that aims to calculate sensitivity maps for real fuel injectors and it represents the initial steps in achieving this goal. The main contribution of this work has been to apply the sensitivity analysis techniques developed by Hill (1992) and Giannetti & Luchini (2007) for incompressible flow behind a cylinder to low-density jet diffusion flames. This has enabled the calculation of sensitivity maps for the lifted flame, which describe the most sensitive regions to open-loop forcing and heating, to perturbations in the hydrodynamic feedback coupling that drives the global instability and to the placement of a hot wire into the flow.

These sensitivity analyses confirm the observation made in chapter 3 (based on the spatial structure of the direct global mode) that the most sensitive area of the lifted flame is in the pre-mixing zone. The sensitivity maps provide a quantitative assessment of how perturbations in the pre-mixing zone of a lifted flame affect the hydrodynamic stability and show in detail the areas within the pre-mixing zone that can enhance or suppress the instability, or increase or decrease the global mode frequency.

Comparing the results of the lifted flame to the results of the hot jet highlights the effect that the heat release from reaction has on the underlying hydrodynamics. In the hot jet, the direct global mode is free to grow downstream until the slowly spreading shear layer in the base flow can no longer support the frequency of oscillation. By contrast the direct global mode in the flame can only grow a short distance downstream before it is altered significantly by the thermal expansion at the base of the flame. A different instability, driven by the instability arising in the pre-mixing zone, takes over in the flame. This observation is supported well by the sensitivity and local analyses in chapter 4.

The framework developed to analyze the sensitivity to force feedback can be of much more general use in the fluid dynamics community. Considering the feedback force as a gain multiplying a unitary matrix separates the strength of the feedback from the mechanism that causes it. The unitary matrix can be set up, for example, to mimic drag from a cylinder or lift from an aerofoil or a specific sensor-actuator arrangement for flow control.

The work presented here and the thoughts about future extensions in chapter 5 provide firm foundations on which to build a deeper understanding into the sensitivity of hydrodynamic instabilities in variable-density and reacting shear flows. While sensitivity of variable density shear flows has been covered by Meliga (2008) and Meliga & Chomaz (2010) using the fully-compressible Navier–Stokes equations, the distinct area of the low-Mach-number approximation and especially the inclusion of reaction has up until now not been covered. By including reaction into the Navier–Stokes equations a large forward step has been taken in applying these techniques to real fuel injectors.

Bibliography

Åkervik, E., Brandt, L., Henningson, D. S., Hœpffner, J., Marxen, O. & Schlatter, P. 2006 Steady solutions of the Navier–Stokes equations by selective frequency damping. *Phys. Fluids* **18** (6), 068102–1–068102–4.

Ananthkrishnan, N., Deo, S. & Culick, F. E. C. 2005 Reduced-order modeling and dynamics of nonlinear acoustic waves in a combustion chamber. *Combust. Sci. Technol.* **177**, 221–247.

Andersson, P., Berggren, M. & Henningson, D. S. 1999 Optimal disturbances and bypass transition in boundary layers. *Phys. Fluids* **11** (1), 134–150.

Ashpis, D. E. & Reshotko, E. 1990 The vibrating ribbon problem revisited. *J. Fluid Mech.* **213**, 531–547.

Barkley, D. & Henderson, R. D. 1996 Three-dimensional Floquet stability analysis of the wake of a circular cylinder. *J. Fluid Mech.* **322**, 215–241.

Barrère, M., Jaumotte, A., Fraeijs de Veubeke, B. & Vandenkerckhove, J. 1960 *Rocket Propulsion*. Elsevier.

Bender, C. M. & Orszag, S. A. 1978 *Advanced mathematical methods for scientists and engineers*. McGraw-Hill.

Berkooz, G., Holmes, P. & Lumley, J. L. 1993 The proper orthogonal decomposition in the analysis of turbulent flows. *Ann. Rev. Fluid Mech.* **25**, 539–75.

Bewley, T. R. 2001 Flow control: new challenges for a new renaissance. *Progress in Aerospace Sciences* **37** (1), 21–58.

Bottaro, A., Corbett, P. & Luchini, P. 2003 The effect of base flow variation on flow stability. *J. Fluid Mech.* **476**, 293–302.

BRIGGS, R. J. 1964 *Electron-stream interaction with plasmas*. MIT Press.

BROADWELL, J. E. 1988 Molecular mixing and chemical reactions in turbulent shear flows. In *Disorder and mixing* (ed. E. Guyon, J.-P. Nadal & Y. Pomeau). Kluwer Academic Publishers.

BROADWELL, J. E. & BREIDENTHAL, R. E. 1982 A simple model of mixing and chemical reaction in a turbulent shear layer. *J. Fluid Mech.* **125**, 397–410.

BROADWELL, J. E. & MUNGAL, M. G. 1991 Large-scale structures and molecular mixing. *Phys. Fluids A* **3** (5), 1193–1206.

BROWN, C. D., WATSON, K. A. & LYONS, K. M. 1999 Studies on lifted jet flames in coflow: the stabilization mechanism in the near- and far-fields. *Flow Turbul. Combust.* **62**, 249–273.

BUCKMASTER, J. 1986 The contribution of asymptotics to combustion. *Physica D: Nonlinear Phenomena* **20** (1), 91–108.

BUELL, J. C. & HUERRE, P. 1988 Inflow/outflow boundary conditions and global dynamics of spatial mixing layers. *CTR Proc. Summ. Prog.* pp. 19–27.

BUTLER, K. & FARRELL, B. 1992 Three-dimensional optimal perturbations in viscous shear flows. *Phys. Fluids A* **4** (8), 1637–1650.

CATRAKIS, H. J., AGUIRRE, R. C. & MASON, J. O. 2005 Physical modeling of turbulent fluid interfaces and flow regions at large Reynolds numbers. *IASME Transactions* **2** (1), 1–9.

CATRAKIS, H. J., AGUIRRE, R. C., RUIZ-PLANCARTE, J. & THAYNE, R. D. 2002 Shape complexity of whole-field three-dimensional space-time fluid interfaces in turbulence. *Phys. Fluids* **14** (11), 3891–3898.

CERVIÑO, L. I., BEWLEY, T. R., FREUND, J. B. & LELE, S. K. 2002 Perturbation and adjoint analyses of flow-acoustic interactions in an unsteady 2D jet. *CTR Proc. Summ. Prog.* pp. 27–39.

CHOMAZ, J.-M. 2005 Global instabilities in spatially developing flows: non-normality and nonlinearity. *Ann. Rev. Fluid Mech.* **37**, 357–92.

CHOMAZ, J.-M., HUERRE, P. & REDEKOPP, L. 1991 A frequency selection criterion in spatially developing flows. *Stud. Appl. Math.* **84**, 119–144.

CHORIN, A. J. 1968 Numerical solution of the Navier–Stokes equations. *Math. Comput.* **22** (104), 745–762.

CONSTANTINESCU, G. S. & LELE, S. K. 2002 A highly accurate technique for the treatment of flow equations at the polar axis in cylindrical coordinates using series expansions. *J. Comput. Phys.* **183**, 165–186.

COOK, A. W. & RILEY, J. J. 1996 Direct numerical simulation of a turbulent reactive plume on a parallel computer. *J. Comput. Phys.* **129**, 263–283.

COOLEY, J. W., LEWIS, P. A. W. & WELCH, P. D. 1970 The fast Fourier transform algorithm: programming considerations in the calculation of sine, cosine and Laplace transforms. *J. Sound Vib.* **12**, 315–337.

CORBETT, P. & BOTTARO, A. 2001 Optimal linear growth in swept boundary layers. *J. Fluid Mech.* **435**, 1–23.

CORREIA DA COSTA, B. 2009 Développement d'un logiciel d'analyse locale d'instabilités linéaires hydrodynamiques. *Tech. Rep.*. Department of Engineering, University of Cambridge.

COSSU, C. & CHOMAZ, J.-M. 1997 Global measures of local convective instabilities. *Phys. Rev. Lett.* **78** (23), 4387–4390.

CULICK, F. E. C., BURNLEY, V. & SWENSON, G. 1995 Pulsed instabilities in solid-propellant rockets. *J. Propul. Power* **11** (4), 657–665.

DELBENDE, I. & CHOMAZ, J.-M. 1998 Nonlinear convective/absolute instabilities in parallel two-dimensional wakes. *Phys. Fluids* **10** (11), 2724–2736.

DELBENDE, I., CHOMAZ, J.-M. & HUERRE, P. 1998 Absolute/convective instabilities in the Batchelor vortex: a numerical study of the linear impulse response. *J. Fluid Mech.* **355**, 229–254.

DRAZIN, P. & REID, W. 1981 *Hydrodynamic Stability*. Cambridge University Press.

DRAZIN, P. G. 1958 The stability of a shear layer in an unbounded heterogeneous inviscid fluid. *J. Fluid Mech.* **14** (2), 214–224.

EDWARDS, W. S., TUCKERMAN, L. S., FRIESNER, R. A. & SORENSEN, D. C. 1994 Krylov methods for the incompressible Navier–Stokes equations. *J. Comput. Phys.* **110**, 82–102.

EHRENSTEIN, U. & GALLAIRE, F. 2005 On two-dimensional temporal modes in spatially evolving open flows: the flat-plate boundary layer. *J. Fluid Mech.* **536**, 209–218.

FADLUN, E. A., VERZICCO, R., ORLANDI, P. & MOHD-YUSOF, J. 2000 Combined immersed-boundary finite-difference methods for three-dimensional complex flow simulations. *J. Comput. Phys.* **161**, 35–60.

FLETCHER, C. A. J. 1991 *Computational techniques for fluid dynamics*, 2nd edn., , vol. 1. Springer.

GARCIA-VILLALBA, M., FRÖHLICH, J. & RODI, W. 2006 Numerical simulations of isothermal flow in a swirl burner. *ASME Turbo Expo* pp. GT2006–90764.

GIANNETTI, F., CAMARRI, S. & LUCHINI, P. 2010 Structural sensitivity of the secondary instability in the wake of a circular cylinder. *J. Fluid Mech.* **651**, 319–337.

GIANNETTI, F. & LUCHINI, P. 2007 Structural sensitivity of the first instability of the cylinder wake. *J. Fluid Mech.* **581**, 167–197.

GILES, M. B. & DUTA, M. C. 2003 Algorithm developments for discrete adjoint methods. *AIAA Journal* **41** (2), 198–205.

GOLDSTEIN, D., HANDLER, R. & SIROVICH, L. 1993 Modeling a no-slip flow boundary with an external force field. *J. Comput. Phys.* **105**, 354–366.

GOLDSTEIN, S. 1931 On the stability of superposed streams of fluids of different densities. *Proc. R. Soc. Lond. A* **132**, 524–548.

GRESHO, P. M. 1991 Some interesting issues in incompressible fluid dynamics, both in the continuum and in numerical simulation. In *Advances in applied mechanics* (ed. J. W. Hutchinson & T. Y. Wu), , vol. 28, pp. 45–140. Academic Press.

GUEGAN, A., SCHMID, P. & HUERRE, P. 2006 Optimal energy growth and optimal control in swept Hiemenz flow. *J. Fluid Mech.* **566**, 11–45.

HEATON, C. J., NICHOLS, J. W. & SCHMID, P. 2009 Global linear stability of the non-parallel Batchelor vortex. *J. Fluid Mech.* **629**, 139–160.

HENNINGSON, D. S. & REDDY, S. C. 1994 On the role of linear mechanisms in transition to turbulence. *Phys. Fluids* **6** (3), 1396–1398.

HEPPENHEIMER, T. A. 1997 *Countdown: a history of space flight*. John Wiley & Sons.

HILL, D. C. 1992 A theoretical approach for analyzing the re-stabilization of wakes. *AIAA Paper* pp. 92–0067.

HILL, D. C. 1995 Adjoint systems and their role in the receptivity problem for boundary layers. *J. Fluid Mech.* **292**, 183–204.

HUERRE, P. 2000 Open shear flow instabilities. In *Perspectives in fluid dynamics : a collective introduction to current research* (ed. G. K. Batchelor, H. K. Moffat & M. G. Worster). Cambridge University Press.

HUERRE, P. & MONKEWITZ, P. 1985 Absolute and convective instabilities in free shear layers. *J. Fluid Mech.* **159**, 151–168.

HUERRE, P. & MONKEWITZ, P. 1990 Local and global instabilities of spatially developing flows. *Ann. Rev. Fluid Mech.* **22**, 473–537.

HUERRE, P. & ROSSI, M. 1998 Hydrodynamic instabilities in open flows. In *Hydrodynamics and nonlinear instabilities* (ed. C. Goldrèche & P. Manneville), pp. 81–294. Cambridge University Press.

JACKSON, C. P. 1987 A finite-element study of the onset of vortex shedding in flow past variously shaped bodies. *J. Fluid Mech.* **182**, 23–45.

JAMESON, A. 1988 Aerodynamic design via control theory. *J. Sci. Comput.* **3** (3), 233–260.

JAMESON, A. 1999 Re-engineering the design process through computation. *J. Aircraft* **36** (1), 36–50.

JENDOUBI, S. & STRYKOWSKI, P. J. 1994 Absolute and convective instability of axisymmetric jets with external flow. *Phys. Fluids* **6** (9), 3000–3009.

JUNIPER, M. & CANDEL, S. 2003 The stability of ducted compound flows and consequences for the geometry of coaxial injectors. *J. Fluid Mech.* **482**, 257–269.

JUNIPER, M. P. 2006 The effect of confinement on the stability of two-dimensional shear flows. *J. Fluid Mech.* **565**, 171–195.

JUNIPER, M. P. 2008 The effect of confinement on the stability of non-swirling round jet/wake flows. *J. Fluid Mech.* **605**, 227–252.

JUNIPER, M. P. 2011 Triggering in the horizontal Rijke tube: non-normality, transient growth and bypass transition. *J. Fluid Mech.* **667**, 272–308.

JUNIPER, M. P., LI, L. K. B. & NICHOLS, J. W. 2009 Forcing of self-excited round jet diffusion flames. *Proc. Combust. Inst.* (32), 1191–1198.

KHORRAMI, M. R., MALIK, M. R. & ASH, R. L. 1989 Application of spectral collocation techniques to the stability of swirling flows. *J. Comput. Phys.* **81** (1), 206–229.

KIMURA, I. 1965 Stability of laminar-jet flames. *Proc. Combust. Inst.* (10), 1296–1300.

KYLE, D. M. & SREENIVASAN, K. R. 1993 The instability and breakdown of a round variable-density jet. *J. Fluid Mech.* **249**, 619–664.

LEHOUCQ, R. B., SORENSEN, D. C. & YANG, C. 1998 *ARPACK Users' Guide*. SIAM.

LELE, S. K. 1992 Compact finite difference schemes with spectral-like resolution. *J. Comput. Phys.* **103**, 16–42.

LESSHAFFT, L. & HUERRE, P. 2007 Linear impulse response in hot round jets. *Phys. Fluids* **19** (2), 024102–1–024102–11.

LESSHAFFT, L., HUERRE, P., SAGAUT, P. & TERRACOL, M. 2006 Nonlinear global modes in hot jets. *J. Fluid Mech.* **554**, 393–409.

LINGENS, A., NEEMANN, K., MEYER, J. & SCHREIBER, M. 1996 Instability of diffusion flames. *Proc. Combust. Inst.* **26**, 1053–1061.

LUCHINI, P. 2000 Reynolds-number-independent instability of the boundary layer over a flat surface: optimal perturbations. *J. Fluid Mech.* **404**, 289–309.

LUCHINI, P., GIANNETTI, F. & PRALITS, J. O. 2008 Structural sensitivity of linear and nonlinear global modes. In *5th AIAA Theor. Fluid Mech. Conf., Seattle*. AIAA paper no. AIAA-2008-4227.

MARQUET, O. 2008 Sensitivity analysis and passive control of cylinder flow. *J. Fluid Mech.* **615**, 221–252.

MAXWORTHY, T. 1999 The flickering candle: transition to a global oscillation in a thermal plume. *J. Fluid Mech.* **390**, 297–323.

MCMURTRY, P. A. 1987 Direct numerical simulations of a reacting mixing layer with chemical heat release. PhD thesis, University of Washington.

MCMURTRY, P. A., JOU, W.-H., RILEY, J. J. & METCALFE, R. W. 1986 Direct numerical simulations of mixing layers with heat release. *AIAA Journal* **24**, 962.

MELIGA, P. 2008 A theoretical approach for the onset and control of unsteadiness in compressible afterbody flows. PhD thesis, École Polytechnique.

MELIGA, P. & CHOMAZ, J.-M. 2010 Global modes in a confined impinging jet: application to heat transfer and control. *Theor. Comput. Fluid Dyn.* **25**.

MICHALKE, A. 1984 Survey on jet instability theory. *Prog. Aerospace Sci.* **21**, 159–199.

MITTAL, R. & IACCARINO, G. 2005 Immersed boundary methods. *Ann. Rev. Fluid Mech.* **37**, 239–261.

MOECK, J. P., OEVERMANN, M., KLEIN, R., PASCHEREIT, C. O. & SCHMIDT, H. 2009 A two-way coupling for modeling thermoacoustic instabilities in a flat flame Rijke tube. *Proc. Combust. Inst.* (32), 1199–1207.

MONKEWITZ, P. A., BECHERT, D. W., BARSIKOW, B. & LEHMANN, B. 1990 Self-excited oscillations and mixing in a heated round jet. *J. Fluid Mech.* **213**, 611–639.

MONKEWITZ, P. A., HUERRE, P. & CHOMAZ, J.-M. 1993 Global linear stability analysis of weakly non-parallel shear flows. *J. Fluid Mech.* **251**, 1–20.

MONKEWITZ, P. A., LEHMANN, B., BARSIKOW, B. & BECHERT, D. W. 1989 The spreading of self-excited hot jets by side jets. *Phys. Fluids A* **1** (3), 446–448.

MONKEWITZ, P. A. & SOHN, K. D. 1988 Absolute instability in hot jets. *AIAA Journal* **26** (8), 911–916.

MUNSON, B. R., YOUNG, D. F. & OKIISHI, T. H. 1998 *Fundamentals of fluid mechanics*, 3rd edn. John Wiley & Sons.

NAJM, H. N., WYCKOFF, P. S. & KNIO, O. M. 1998 A semi-implicit numerical scheme for reacting flow. *J. Comput. Phys.* **143**, 381–402.

NEWMAN, J. C., TAYLOR, A. C., BARNWELL, R. W., NEWMAN, P. A. & HOU, G. J.-W. 1999 Overview of sensitivity analysis and shape optimization for complex aerodynamic configurations. *J. Aircraft* **36** (1), 87–96.

NICHOLS, J. W. 2005 Simulation and stability analysis of jet diffusion flames. PhD thesis, University of Washington.

NICHOLS, J. W., CHOMAZ, J.-M. & SCHMID, P. J. 2009 Twisted absolute instability in lifted flames. *Phys. Fluids* **21** (2), 015110–015110–8.

NICHOLS, J. W. & SCHMID, P. J. 2008 The effect of a lifted flame on the stability of round fuel jets. *J. Fluid Mech.* **609**, 275–284.

NICHOLS, J. W., SCHMID, P. J. & RILEY, J. J. 2007 Self-sustained oscillations in variable-density round jets. *J. Fluid Mech.* **582**, 341–376.

OLENDRARU, C., SELLIER, A., ROSSI, M. & HUERRE, P. 1999 Inviscid instability of the Batchelor vortex: absolute-convective transition and spatial branches. *Phys. Fluids* **11** (7), 1805–1820.

PIER, B. 2002 On the frequency selection of finite-amplitude vortex shedding in the cylinder wake. *J. Fluid Mech.* **458**, 407–417.

PIER, B. 2010 Signalling problem in absolutely unstable systems. *Theor. Comput. Fluid Dyn.* **25**.

PIRONNEAU, O. 1974 On optimum design in fluid mechanics. *J. Fluid Mech.* **64**, 97–110.

POINSOT, T. & VEYNANTE, D. 2005 *Theoretical and Numerical Combustion*, 2nd edn. Edwards.

PROTAS, B., BEWLEY, T. R. & HAGEN, G. 2004 A computational framework for the regularization of adjoint analysis in multiscale PDE systems. *J. Comput. Phys.* **195**, 49–89.

PROTAS, B. & LIAO, W. 2008 Adjoint-based optimization of PDEs in moving domains. *J. Comput. Phys.* **227**, 2707–2723.

RAYLEIGH, L. 1880 On the stability and instability of certain fluid motions. *Proc. Lond. Maths. Soc.* **11**, 57–70.

REDDY, S. C., SCHMID, P. J. & HENNINGSON, D. S. 1993 Pseudospectra of the Orr–Sommerfeld operator. *SIAM J. Appl. Math.* **53** (1), 15–47.

ROWLEY, C. W., MEZIC, I., BAGHERI, S., SCHLATTER, P. & HENNINGSON, D. S. 2009 Spectral analysis of nonlinear flows. *J. Fluid Mech.* **641**, 115–127.

RUHE, A. 1983 The two-sided Arnoldi algorithm for non-symmetric eigenvalue problems. In *Matrix pencils* (ed. B. Kågström & A. Ruhe), *Lecture Notes in Mathematics*, vol. 973/1983, pp. 104–120. Springer Berlin / Heidelberg.

SALWEN, H. & GROSCH, C. E. 1981 The continuous spectrum of the Orr–Sommerfeld equation. Part 2. Eigenfunction expansions. *J. Fluid Mech.* **104**, 445–465.

SANI, R. L., SHEN, J., PIRONNEAU, O. & GRESHO, P. M. 2006 Pressure boundary condition for the time-dependent incompressible Navier–Stokes equations. *Int. J. Numer. Meth. Fluids* **50**, 673–682.

SATO, H., KUSHIDA, G., AMAGAI, K. & ARAI, M. 2002 Numerical analysis of the gravitational effect on the buoyancy-driven fluctuations in diffusion flames. *Proc. Combust. Inst.* (29), 1671–1678.

SCHMID, P. J. 2007 Nonmodal stability theory. *Ann. Rev. Fluid Mech.* **39**, 129–162.

SCHMID, P. J. 2010 Dynamic mode decomposition of numerical and experimental data. *J. Fluid Mech.* **656**, 5–28.

SCHMID, P. J. & HENNINGSON, D. S. 2001 *Stability and transition of shear flows.* Springer, New York.

SCHMID, P. J., LI, L., JUNIPER, M. P. & PUST, O. 2010 Applications of the dynamic mode decomposition. *Theor. Comput. Fluid Dyn.* DOI:10.1007/s00162-010-0203-9.

SCHUMANN, U. & SWEET, R. A. 1988 Fast Fourier transforms for direct solution of Poisson's equation with staggered boundary conditions. *J. Comput. Phys.* **75**, 123–137.

SIRKES, Z. & TZIPERMAN, T. 1997 Finite difference of adjoint or adjoint of finite difference? *Mon. Weath. Rev.* **125** (7), 3373–3378.

SREENIVASAN, K. R., RAGHU, S. & KYLE, D. 1989 Absolute instability in variable density round jets. *Exp. Fluids* **7**, 309–317.

SRIPAKAGORN, P., MITARAI, S., KOSÁLY, G. & PITSCH, H. 2004 Extinction and re-ignition in a diffusion flame: a direct numerical simulation study. *J. Fluid Mech.* **518**, 231–259.

STRYKOWSKI, P. J. & SREENIVASAN, K. R. 1990 On the formation and suppression of vortex 'shedding' at low reynolds numbers. *J. Fluid Mech.* **218**, 71–107.

SWARZTRAUBER, P. N. 1977 The methods of cyclic reduction, Fourier analysis and the FACR algorithm for the discrete solution of Poisson's equation on a rectangle. *SIAM Rev.* **19** (3), 490–501.

TAYLOR, G. I. 1931 Effect of variation in density on the stability of superposed streams of fluid. *Proc. R. Soc. Lond. A* **132**, 499–523.

TOONG, T.-Y., SALANT, R. F., STOPFORD, J. M. & ANDERSON, G. Y. 1965 Mechanisms of combustion instability. *Proc. Combust. Inst.* (10), 1301–1313.

TREFETHEN, L. N., TREFETHEN, A. E., REDDY, S. C. & DRISCOLL, T. A. 1993 Hydrodynamic stability without eigenvalues. *Science* **261**, 578–584.

VOGEL, C. R. & WADE, J. G. 1995 Analysis of costate discretizations in parameter estimation for linear evolution equations. *SIAM J. Control and Optimization* **33** (1), 227–254.

WHITE, A. J. 2008 *Engineering Tripos part IB, experiment T4: Heat transfer from a heated circular wire*. Cambridge University Eng. Dept.

YILDIRIM, B. S. & AGRAWAL, A. K. 2005 Full-field measurements of self-excited oscillations in momentum-dominated helium jets. *Exp. Fluids* **38**, 161–173.

ZEBIB, A. 1987 Stability of viscous flow past a circular cylinder. *J. Eng. Math.* **21**, 155–165.

ZUCCHER, S., BOTTARO, A. & LUCHINI, P. 2006 Algebraic growth in a Blasius boundary layer: nonlinear optimal disturbances. *Eur. J. Mech. B-Fluids* **25** (1), 1–17.